THRESHOLDS TO XE-135 INDUCED FLUX OSCILLATIONS IN THE PICKERING AND BRUCE NUCLEAR POWER REACTORS

by

J.V.B. Simmons

PART A: INDUSTRIAL PROJECT*

A project report submitted in partial fulfillment of the
requirements for the degree of
Master of Engineering

The work reported upon herein was undertaken at
Atomic Energy of Canada Limited, Sheridan Park, Ontario,

Dept. of Engineering Physics
McMaster University
Hamilton, Ontario
1970

---

* One of two project reports. The other part is designated PART B: McMASTER (ON-CAMPUS) PROJECT.

TITLE (PART A): Thresholds to XE-135 Induced Flux Oscillations in the Pickering and Bruce Nuclear Power Reactors

AUTHOR: J.V.B. Simmons, B.Ap.Sc. (Univ. of Toronto)

SUPERVISOR: Professor O. A. Trojan

NUMBER OF PAGES: vi, 75

MASTER OF ENGINEERING
(Engineering Physics)

McMASTER UNIVERSITY
Hamilton, Ontario

ABSTRACT

Xenon induced flux oscillations are possible in large thermal reactors operating at high powers because of the inter-play between the xenon concentration, reactivity, and thermal flux, and the fact that xenon is produced mainly by radioactive decay of I-135, which has a half-life of 6.7 hours. Due to these nuclear characteristics along with size and operating conditions of the Pickering and Bruce cores, these oscillations in flux are inherently unstable with respect to xenon. That is, a local perturbation in reactivity will result in a divergent and cyclic time and space variation in the thermal flux distribution in the core.

One group diffusion theory and a simple perturbation analysis yield for a bare thermal reactor, a threshold in the average flux level ϕ which satisfies (1)

$$\frac{M^2 \lambda ij^2}{\alpha_{xe}} - \frac{\alpha_T}{\alpha_{xe}} \phi = f(\phi)$$

$$= \frac{\dfrac{1}{1 + \lambda_{xe}/\sigma_{xe}\phi} - \mu_{xe}}{1 + (\lambda_{xe} + \lambda_I)/\sigma_{xe}\phi}$$

for oscillations in ij^{th} mode of the flux distribution (see Figure 1) M^2 is the migration area in cm^2, α_{xe} is the reactivity load of Xe-135 at high flux levels; α_T is the fuel temperature coefficient expressed in terms of reactivity change per unit flux. The function $f(\phi)$ depends only upon the decay constants λ_{xe} of Xe-135 and λ_I of I-135; μ_{xe} is the fraction of Xe-135 produced directly from the fission of the fuel rather than through iodine decay (which fraction is denoted by μ_I). The dimensionless parameter λij^2 depends only upon the shape of the flux distribution and is equal to the difference between the bulking of the ij^{th} mode and the fundamental model.

The Bruce and Pickering reactors are used as models in this study to determine the threshold power level at which xenon instability is possible and in which mode this instability occurs.

Bruce is found to be unstable in the fundamental and first azimuthal mode for fresh and equilibrium fuel conditions, and stable for the radial, axial and higher azimuthal modes.

Pickering, on the other hand, is unstable for the equilibrium fuel condition in the fundamental and first azimuthal modes only and is stable in every mode except the fundamental in the fresh fuel condition.

TABLE OF CONTENTS

LIST OF TABLES

LIST OF TABLES (continued)

LIST OF FIGURES

ACKNOWLEDGEMENTS

The author is indebted to Atomic Energy of Canada Limited for providing a position on their staff to carry out the Industrial Experience Requirement of the M.Eng. program at McMaster. In particular, O.A. Trojan, A.R. Dastur and D.B. Miller provided help and insight into seeing the project to its conclusion.

1. INTRODUCTION

The presence of xenon poison in large thermal reactors operating at high flux levels may lead to a potentially unstable operation (1, 2, 3).

A reactor which has been operating at constant power with a steady flux distribution will develop an equilibrium xenon distribution throughout the core. If for some reason there occurs a slight radial, axial or azimuthal tilting of the thermal flux due to small changes in the local multiplication constant of the core, the rate of destruction of Xe-135 by neutron capture will increase in that part of the core where the flux increased, call this region A, while its rate of formation from decay of I-135 will initially remain constant.

Conversely, in the other region, B, where the flux decreased the rate of destruction will be reduced while the rate of formation remains constant, assuming the control scheme keeps the total reactor power at a constant value. The Xe-135 concentration will therefore increase, raising the absorption cross-section of non-fissile material in this region. The resultant decrease in the local multiplication constant, K_∞, will lessen the flux even more.

In region A, the local multiplication constant will increase due to the decrease of non-fissile materials absorption cross-section.

The intial flux tilt thus augments itself until the rate of decay of the increasing I-135 concentration matches and becomes greater than the destruction of Xe-135 atoms by neutron absorption in region A.

In region B, the flux level ceases to decrease and increases in magnitude since the rate of formation of Xe-135 from I-135 decay has lessened.

The thermal flux distribution will oscillate in a see-saw fashion between these two parts of the core, as will the power distribution since it is directly proportional to flux in the fuelled portion of the core. The total power on the other hand remains constant.

The above interplay does not, however, automatically make a system unstable with respect to xenon; the following physical features of the core are important:

(a) A high thermal flux level is prerequisite to xenon instability. The reason being that a high flux level implies a high iodine concentration, hence a potentially high xenon concentration.

(b) The physical size of the core, or rather the physical size in units of the neutron migration length, is important because it affects the probability that a neutron born in one subregion of the core will migrate to another subregion and initiate fission there. The lower this probability is the more will the two subregions act as independent reactors. The physical size is also important in determining the leakage of neutrons from the system, the greater the leakage the more stable the reactor will be.

(c) The more flattened the flux distribution is the smaller is the margin against xenon instability due to the low leakage in the flattened subregion.

(d) A positive power coefficient (increase in reactivity with power) enhances xenon instability because it augments the effect of variation in the xenon concentration.

With reference to the above points, the pertinent Pickering data and characteristics are (also meaningful for Bruce due to these basic similarities):

(a) xenon destruction due to neutron absorption is up to 14 times that due to radioactive decay;

(b) the length of the core is about 30 times the neutron migration length while the diameter is even greater;

(c) the radial and axial form factors of the actual core are respectively 0.791 and 0.702; the corresponding numbers for the unflattened core are respectively 0.591 and 0.635; and

(d) in equilibrium fuel conditions, the fuel temperature coefficient is only slightly negative while the fresh fuel condition has a fuel temperature coefficient which is more negative, thereby increasing the stability of the reactor.

These xenon-induced flux oscillations are usually divided into four types: fundamental, azimuthal, radial and axial instabilities.

Oscillations in the fundamental mode results in a uniform fractional change in the thermal neutron flux level throughout the core; consequently, the total reactor power will oscillate correspondingly. Any positive control action will counteract this type of oscillation and for this reason nothing more will be said about fundamental mode instabilities in the Bruce and Pickering reactors.

Axial, azimuthal, and radial oscillations in the thermal flux may take place at constant total reactor power; therefore, these types of oscillations pose more stringent requirements on the control action than does oscillation in the fundamental mode.

Oscillations in the first axial and first azimuthal modes manifest themselves by cyclic redistribution of xenon between two halves of the core: in the former case, the core being divided into two axial halves; in the latter case, the core being divided into two halves by any radial plane. (See Figure 1 for the form of the variations in the different modes.)

2. MATHEMATICAL FORMALISM

Since the Bruce and Pickering reactors are large thermal reactors, a one-group diffusion theory analysis is thought to be sufficient for this stability study. The thermal flux satisfies

$$\nabla^2\phi + B^2\phi = 0 \qquad (2.1)$$

where the delayed neutrons have been neglected because of their disproportionately small time constant compared to the time constant for a xenon oscillation. It can be seen from the above relation that at any time the shape of the thermal neutron distribution is determined by the spatial distribution of B^2.

The concentration of I-135 and Xe-135 is governed by the following equations:

$$\frac{dI}{dt} = \gamma_I \Sigma_f \phi - \lambda_I I \qquad (2.2)$$

$$\frac{dXe}{dt} = \lambda_I I + \gamma_{xe}\Sigma_f\phi - \lambda_{xe}Xe - \sigma_{xe}\phi Xe \qquad (2.3)$$

where Xe and I are the concentrations of xenon and iodine, respectively. γ_{xe} and γ_I are their absolute yields in atoms per fission of the fuel. λ_{xe} and λ_I are their associated decay constants. σ_{xe} is the microscopic absorption cross-section for xenon and Σ_f is the macroscopic fission cross-section for the fuel. The saturated iodine concentration is from (2.2) setting $\frac{dI}{dt} = 0$

$$I_{sat} = \frac{\gamma_I \Sigma_f \phi}{\lambda_I} \qquad (2.4)$$

Likewise, when (2.4) is substituted in (2.3) and $\frac{dX}{dt} = 0$, it is found that the saturated xenon concentration

$$X_{sat} = \frac{(\gamma_I + \gamma_{xe})\,\Sigma_f\,\phi}{\lambda_{xe} + \sigma_{xe}\,\phi} \qquad (2.5)$$

For very high flux levels, this last expression has the value

$$X_{\infty} = \frac{(\gamma_I + \gamma_{xe})\,\Sigma_f}{\sigma_{xe}} \qquad (2.6)$$

Now, if (2.2) and (2.3) are divided through by (2.6), the following relations occur:

$$\frac{di}{dt} = \sigma_{xe}\,\phi\,\mu_I = \lambda_I\,i \qquad (2.7)$$

$$\frac{dx}{dt} = \lambda_I i + \sigma_{xe}\phi\,\mu_{xe} - \lambda_{xe}X - \sigma_{xe}\phi X \qquad (2.8)$$

where i and X are the concentrations of iodine and xenon relative to that of the saturation xenon concentration at very high flux. μ_I and μ_{xe} are the fractions

$$\frac{\gamma_I}{\gamma_I + \gamma_{xe}} \quad \text{and} \quad \frac{\gamma_{xe}}{\gamma_I + \gamma_{xe}} \quad \text{respectively.}$$

It is assumed that all perturbations are small and the following quantities undergo oscillations about their equilibrium value

$$\phi = \phi^* + \phi^1 \qquad (2.9)$$

$$B^2 = B^{2*} + a_T\phi^1 + a_{xe}\,X^1 \qquad (2.10)$$

$$X = X^* + X^1 \qquad (2.11)$$

$$i = i^* + i^1 \qquad (2.12)$$

where the asterisk (*) quantities are solutions of the unperturbed equations, and those which are primed are the small perturbations. a_T and a_{xe} express the dependence of B^2 resulting from changes in flux and Xe-135 concentrations, respectively.

If expressions (2.9) through (2.12) are substituted into equations (2.1), (2.7) and (2.8), the following set of equations result:

$$\nabla^2\phi^* + \nabla^2\phi^1 + B^{*2}\phi^* + B^{*2}\phi^1 + \phi^* a_T \phi^1 + \phi^* a_{xe} X^1 = 0 \qquad (2.13)$$

where $\phi^1 a_T \phi^1$ and $\phi^1 a_{xe} X^1$ have been neglected inthis linear analysis as negligible second order effects.

$$\frac{di^*}{dt} + \frac{di^1}{dt} = \phi^*\sigma_{xe}\mu_I + \phi^1\sigma_{xe}\mu_I - \lambda_I i^* - \lambda_I i^1 \qquad (2.14)$$

$$\frac{dX^*}{dt} + \frac{dX^1}{dt} = \lambda_I i^* + \lambda_I i^1 + \sigma_{xe}\phi^*\mu_{xe} + \sigma_{xe}\phi^1\mu_{xe} - \lambda_{xe}X^* - \lambda_{xe}X^1$$

$$- \sigma_{xe}\phi^* X^* - \sigma_{xe}\phi^* X^1 - \sigma_{xe}\phi^1 X^* \qquad (2.15)$$

where again the second order term $\sigma_{xe}\phi^1 X^1$ has been neglected. This approximation is good since near the oscillation threshold the perturbation is indeed small and the product of two small disturbances will be completely negligible.

Subtracting the unperturbed equations (2.1), (2.7) and (2.8) from these last three equations respectively yields

$$\nabla^2\phi^1 + B^{*2}\phi^1 + \phi^* a_{xe} X^1 + \phi^* a_T \phi^1 = 0 \qquad (2.16)$$

$$\frac{di^1}{dt} = \phi^1\sigma_{xe}\mu_I - \lambda_I i^1 \qquad (2.17)$$

$$\frac{dX^{1}}{dt} = \lambda_{I} i^{1} + \sigma_{xe} \phi^{1} \mu_{xe} - \lambda_{xe} X^{1} - \sigma_{xe} X^{1} \phi^{*} - \sigma_{xe} X^{*} \phi^{1} \tag{2.18}$$

Since these equations are linear, solutions with time dependence ($e^{\omega t}$) are sought. That is,

$$\phi^{1} = \phi^{11} e^{\omega t} \tag{2.19}$$

$$i^{1} = i^{11} e^{\omega t} \tag{2.20}$$

$$X^{1} = X^{11} e^{\omega t} \tag{2.21}$$

If these last three expressions are substituted in equations (2.16) through (2.18), the following relations are obtained after dividing through by $e^{\omega t}$.

$$\nabla^{2} \phi^{11} + B^{*2} \phi^{11} + \phi^{*} a_{xe} X^{11} + \phi^{*} a_{T} \phi^{11} = 0 \tag{2.22}$$

$$\omega i^{11} = \phi^{11} \sigma_{xe} \mu_{I} - \lambda_{I} i^{11} \tag{2.23}$$

$$\omega X^{11} = \lambda_{I} i^{11} + \sigma_{xe} \phi^{11} \mu_{xe} - \lambda_{xe} X^{11} - \sigma_{xe} \phi^{*} X^{11} - \sigma_{xe} \phi^{11} X^{*} \tag{2.24}$$

ϕ^{11}, X^{11} and i^{11}, the perturbation amplitudes are now expanded in terms of orthonormal eigen-functions g_i

$$\phi^{11} = \sum_{i} A_i \, g_i \tag{2.25}$$

$$X^{11} = \sum_{i} X_i \, g_i \tag{2.26}$$

These eigen-functions satisfy the boundary condition $g_i = 0$ at the extrapolated surface of the bare reactor and are solutions of

$$(\nabla^2 + B^{*2})g_i + \xi^2_i \; g_i = 0 \tag{2.27}$$

The fundamental solution is the unperturbed flux shape since ξ_o is zero and g_o is proportional to the unperturbed flux. ξ^2_i is the eigenvalue of the equation.

From (2.23)

$$i^{11} = \frac{\phi^{11} \; \sigma_{xe} \; \mu_I}{\omega + \lambda_I} \tag{2.28}$$

Substituting this last expression (2.28) along with (2.25) and (2.26) into (2.22) and (2.24) results in

$$\sum_i A_i \left\{ \nabla^2 g_i + B^{*2} g_i \right\} + \phi^* a_{xe} \sum_i X_i g_i + \phi^* a_T \sum_i A_i g_i = 0 \tag{2.29}$$

$$\omega \sum_i X_i g_i = \frac{\lambda_I \sum_i A_i g_i \; \sigma_{xe} \; \mu_I}{\omega + \lambda_I} + \sigma_{xe} \sum_i A_i g_i \; \mu_{xe}$$

$$- \lambda_{xe} \sum_i X_i g_i - \sigma_{xe} \phi^* \sum_i X_i g_i - \sigma_{xe} \sum_i A_i g_i X^* \tag{2.30}$$

If equations (2.29) and (2.30) are multiplied through by g_j and integrated over the reactor volume and (2.27) is employed, they become

$$- \xi^2_i A_j + a_{xe} \sum_i X_i \int_V \phi^* g_i g_j \; dV + a_T \sum_i A_i \int_V \phi^* g_i g_j \; dV = 0 \tag{2.31}$$

$$\omega X_j = \frac{\lambda_I}{\omega + \lambda_I} A_j \; \sigma_{xe} \mu_I + \sigma_{xe} A_j \mu_{xe} - \lambda_{xe} X_j$$

$$- \sigma_{xe} \sum_i X_i \int_V \phi^* g_i g_j \; dV - \sigma_{xe} \sum_i A_i \int_V X^* g_i g_j \; dV \tag{2.32}$$

Making the following symbolic changes

$$\bar{\emptyset}_j = \int \emptyset^* g_j^2 \, dV \tag{2.33}$$

$$\bar{\emptyset}_{ij} = \int \emptyset^* g_i g_j \, dV \tag{2.34}$$

$$\bar{X}_j = \int X^* g_j^2 \, dV \tag{2.35}$$

$$\bar{X}_{ij} = \int X^* g_i g_j \, dV \tag{2.36}$$

allows (2.31) and (2.32) to be rewritten.

$$(-\xi_j^2 + a_T\bar{\emptyset}_j)A_j + a_{xe} X_j \bar{\emptyset}_j + \sum_{i\neq j} (a_{xe}\bar{\emptyset}_{ij}X_i + a_T\bar{\emptyset}_{ij} A_i) = 0 \tag{2.37}$$

$$(\omega + \lambda_{xe} + \sigma_{xe}\bar{\emptyset}_j)X_j + \sigma_{xe}\left\{\bar{X}_j - \mu_{xe} - \frac{\lambda_I\mu_I}{\omega+\lambda_I}\right\}A_j$$

$$+ \sum_{i\neq j} (\sigma_{xe}X_i\bar{\emptyset}_{ij} + \sigma_{xe}A_i\bar{X}_{ij}) = 0 \tag{2.38}$$

Equations (2.37) and (2.38) form a homogeneous, linear set of equations for A_j and X_j. The cross-product terms $\bar{\emptyset}_{ij}$ and $\bar{X}_{ij}$ are very small because of the orthogonality condition and are identically zero for a perfectly flat flux distribution. The power distributions for Bruce and Pickering in our simplified analysis are approximately 60 percent flat and the cross-product terms are assumed negligible. Setting the determinant of the coefficients in (2.37) and (2.38) to zero defines a quadratic equation for the unknown inverse period of oscillation ω. The possible values of ω are defined by the equation

$$\omega^2 + b\omega + c = 0 \tag{2.39}$$

where

$$b = \lambda_I + \lambda_{xe} + \sigma_{xe}\bar{\emptyset}_j - \frac{a_{xe}\sigma_{xe}\bar{\emptyset}_j(\bar{X}_j - \mu_{xe})}{(-\xi_j^2 + a_T\bar{\emptyset}_j)} \tag{2.40}$$

$$\text{and} \quad c = \lambda_I \left\{ \lambda_{xe} + \sigma_{xe}\bar{\phi}_j + \frac{a_{xe}\,\sigma_{xe}\,\bar{\phi}_j\,(1 - \bar{X}_j)}{(-\xi_j^2 + a_T\,\bar{\phi}_j)} \right\} \tag{2.41}$$

A positive value of b is a stable situation since the oscillations will die away. A negative value on the other hand leads to an oscillatory behaviour growing exponentially with time and is therefore an unstable condition.

The threshold of instability can thus be found by setting b = 0

$$-\xi_j^2 + a_T\bar{\phi}_j = \frac{a_{xe}\,\sigma_{xe}\,\bar{\phi}_j\,(\bar{X}_j - \mu_{xe})}{\lambda_I + \lambda_{xe} + \sigma_{xe}\,\bar{\phi}_j} \tag{2.42}$$

$$\xi_j^2 = \frac{-a_{xe}(\bar{X}_j - \mu_{xe})}{1 + \dfrac{\lambda_I + \lambda_{xe}}{\sigma_{xe}\,\bar{\phi}_j}} + a_T\,\bar{\phi}_j \tag{2.43}$$

$$= -\,a_{xe}\,f(\bar{\phi}_j) + a_T\bar{\phi}_j \tag{2.44}$$

The eigenvalues ξ_j^2 from (2.27) are identical to the difference in buckling of the ij^{th} mode of the flux distribution and the fundamental mode. These differences in buckling, call them λ_{ij}^2, depend on the flux shape and the reactor size. However, the righthand side of (2.43) shows λ_{ij}^2 depends primarily on flux level and secondarily on flux shape.

Since $\bar{\phi}_j$ is the steady-state value of the effective flux in the reactor, the approximation that $\bar{X}_j$ is equal to the steady-state value of xenon relative to the xenon concentration at a high flux level $\bar{\phi}_j$ is made.

$$\bar{X}_j = \frac{(\gamma_I + \gamma_{xe})\,\Sigma_f\,\bar{\phi}_j}{\lambda_{xe} + \sigma_{xe}\,\bar{\phi}_j} \Bigg/ \frac{(\gamma_I + \gamma_{xe})\,\Sigma_f}{\sigma_{xe}} \tag{2.45}$$

$$= \frac{1}{1 + \lambda_{xe}/\sigma_{xe}\bar{\phi}_j} \tag{2.46}$$

This approximation is good, since $\bar{\phi}_j$ and $\bar{X}_j$ are averages taken over the same weighting function. Replacing the symbol $\bar{\phi}_j$ by the steady-state flux level ϕ

$$f(\phi) = \frac{\dfrac{1}{1 + \lambda_{xe}/\sigma_{xe}\,\phi} - \mu_{xe}}{1 + \dfrac{\lambda_I + \lambda_{xe}}{\sigma_{xe}\,\phi}} \qquad (2.47)$$

Also, the substitutions $\alpha_{xe} = -a_{xe}M^2$, $\alpha_T = a_T M^2$, $\xi_j^2 = \lambda_{ij}^2$ are made where α_{xe} is the reactivity load held by saturated xenon at very high flux level. The negative sign appears since the change in system reactivity with Xe-135 concentration is negative where, as defined α_{xe} is the xenon load, a positive quantity. a_T is the power coefficient in terms of reactivity change per unit flux, and M^2 is the migration area. The resulting stability criterion is the trancendental equation

$$f(\phi) = \frac{M^2\,\lambda_{ij}^2}{\alpha_{xe}} - \frac{\alpha_T}{\alpha_{xe}}\,\phi \qquad (2.48)$$

where ϕ is the flux level at which undampened xenon oscillations occur. At the oscillation threshold, the period is given by $2\pi/C^{1/2}$, where C is defined as in (2.41).

The function $f(\phi)$ is negative when the flux level is such that the xenon burnoff is equal to or less than its direct formation from fission. If the reactor is to be operated below this flux level, it will be stable with respect to xenon oscillations for all core sizes. The value of $f(\phi)$ then increases monotonically with flux level and saturates at very high flux levels to a value of $(1 - \mu_{xe})$, which has a value of approximately 0.95 which varies with fuel composition. From equation (2.48) it can be seen qualitatively how the power coefficient α_T affects the threshold flux level. A positive value of α_T lowers the value of $f(\phi)$ and therefore the instability flux threshold, and if large enough can cause instability without the xenon. A negative α_T raises the threshold level, and if large enough can eliminate the possibility of xenon oscillations altogether. As previously stated, whenever a flux perturbation is introduced into a reactor, the fundamental as well as the higher mode flux distributions are altered. These altered distributions determine the magnitude of λ_{ij}^2 (see Figure 1 for the form of these altered distributions of the different modes). What determines whether these flux oscillations lead to an unstable xenon distribution is the magnitude and sign of the parameters a_T and a_{xe}.

The fuelled reactor core consists of 480 channels, each 600 cm in length with a lattice pitch of 28.575 cm. Each channel has the geometrical configuration given in Table 1. In reality, these 480 channels are divided into 3 zones, two of which differ only in the coolant temperature by 6°C. This small difference will be neglected, and these two zones combined into what is called zone 2. Zone 1, also known as the flattened zone, is comprised of the innermost 216 channels within a radius, R_F, of 237 cm. Zone 2 extends from R_F to the radius of the fuelled core, R_C = 353 cm; and contains the remaining 264 channels. See Table 2 for the core data. The zonal powers shown in this table are the rates of energy transferred to the coolant which are 95% of the actual fission powers. The fuel in each channel is pushed through the reactor core only once, thus the irradiation (product of flux level and exposure time) for a reactor operating in the steady-state critical condition increases along the channel to a value termed discharge exposure. To counteract this skewing effect on the flux, the fuel is pushed through in opposite directions in adjacent channels so the axial exposure distribution is approximately constant if two adjacent channels are considered together. This fuelling procedure along with relatively small variations in fissile atom concentrations over the residency of the fuel in the reactor enables a single fuel composition to be employed over any region where the terminal irradiation and corresponding burnup is constant. In order for the reactor to operate at the rated power of 2375 MW (thermal) and not to exceed the fuel pencil rating of 48 W/cm, the neutron flux and power distributions are flattened radially. This is achieved by adjusting the fuelling rate of the inner 216 channels to give a discharge exposure of 2.96 neutrons/kilo-barn, at which the reactivity is just sufficient to provide excess neutrons to compensate for axial leakage. The fuelling rates within the outer 264 channels are adjusted according to the average neutron flux over the channel so as to obtain a uniform terminal exposure of 2.06 neutrons/kilo-barn, at which the reactivity associated with this burnup is sufficient to give a critical system. The radial flux and power distributions shown in Figure 2 were calculated from a modified one-group diffusion theory code POOOFBURN for the reflected Bruce reactor. The jump in the power distribution is due to the different fuel compositions of the two zones. Since the lattice properties are uniform along the axial direction, the axial flux and power distributions correspond to a cosine function. See Figure 3.

Since the stability criterion was derived using one-group diffusion theory for a bare thermal reactor, the actual radial flux distribution is not applicable. A new flux distribution was developed by solving the one-group neutron diffusion equation for the bare homogeneous reactor taking account of the reflector by an extrapolated radius, R_E. Thus although the two flux distributions are radically different outside the fuelled core, they are to a good approximation physically similar within the fuelled region. This analytically derived flux distribution is also shown in Figure 2. Note that in this latter distribution the flux is assumed flat over all of zone 1, while the POOOFBURN flux distribution begins to decrease at a value less than the flattened radius R_F of zone 1.

The lattice parameters are taken from the computer code POWDERPUFS-V while the microscopic cross sections employed follow the Westcott convention for averaging over the neutron energy spectrum.

$$\hat{\sigma}_{ij}(r,T_n) = \hat{\sigma}_{ij}(2200)\{g_{ij}(T_n) + r\,S_{ij}(T_n)\} \qquad \text{......(3.1)}$$

where j denotes the process, absorption or fission, and i denotes the isotope specification. T_n and r are the neutron spectrum characteristics of the fuel. The $g_{ij}(T_n)$ factors are given in terms of a polynomial expansion as are the $S_{ij}(T_n)$

$$g_{ij}(T_n) = \sum_{k=1}^{9} a_{ij} T_n^{k-1} \qquad \text{......(3.2)}$$

$$S_{ij}(T_n) = \sum_{k=1}^{9} b_{ij} T_n^{k-1} \qquad \text{......(3.3)}$$

The expression in brackets of (3.1) essentially represents the variation in cross section with respect to neutron temperature. The effective flux, $\hat{\emptyset}_{eff}$, used in POWDERPUFS$^{(4)}$ is the 2200 m/sec flux statistically weighted over the core. The reaction rates used to calculate the lattice parameters are obtained by averaging the macroscopic cross-sections over the channel exposure distribution for discharge exposures, $\overline{W}_T$, of 2.96 and 2.06 neutrons/kilo-barn for the inner and outer zones respectively. The cross sections entering into the burnup equations are those pertaining to the exposure interval.

$$\hat{\sigma}_{ij}(\overline{\Delta w}) = \hat{\sigma}_{ij}(2200)\left\{g_{ij}(T(\overline{\Delta w})) + r(\overline{\Delta w})\; s_{ij}(T(\overline{\Delta w}))\right\} \qquad \ldots\ldots(3.4)$$

The lattice parameters at any exposure, W_T, are calculated on the basis of the average of the accumulated exposure interval macroscopic fuel cross section up to the exposure $\bar{W}_T = n\Delta\bar{W}$. Thus

$$\bar{\Sigma}_j(\bar{W}_T) = \frac{1}{n}\sum_{r=1}^{n}\left\{\sum_i\left\{N_i(\Delta\bar{w}_r)\;\hat{\sigma}_{ij}(\Delta\bar{W}_r)\right\}\right\} \qquad \ldots\ldots(3.5)$$

where i is the type of isotope, j is the type of cross section, and $\Delta\bar{W}_r$ is the average exposure interval where there are n exposure intervals in the life of the fuel. The absorption cross sections, $\bar{\Sigma}_a(\bar{W}_T)$, for each component of the lattice cell are then volume averaged to give a representative cell cross-section. The macroscopic fission cross-section $\bar{\Sigma}_f(\bar{W}_T)$ is also volume averaged to give a uniform fission cross section across the cell.

The radial power form factor is found from POOOFBURN(10) to be 0.85 while the axial power form factor is 0.649.

The one-group diffusion equation to be solved for the bare cylindrical reactor is

$$D\nabla^2\phi - \Sigma_a\phi + k\Sigma_a\phi = 0 \qquad (4.1)$$

where D is the diffusion coefficient, Σ_a is the macroscopic thermal absorption cross-section and k is the effective multiplication constant. Equation (4.1) can be rearranged as

$$\nabla^2\phi + B^2\phi = 0 \qquad (4.2)$$

where B^2 is the geometric buckling of the core and identical to the materials buckling for a critical reactor. The axial flux is found to be a simple cosine distribution when the flux is separated into radial and axial eigenfunctions and the latter is evaluated from (4.2)(see Figure 3). The radial flux is determined from

$$\nabla^2\phi(r) + \beta^2\phi(r) = 0 \qquad (4.3)$$

where β^2 is the radial Laplacian. The general solution of this zero order, ordinary Bessel equation in cylindrical geometry is

$$\phi(r) = AJ_o(\beta r) + BY_o(\beta r) \qquad (4.4)$$

where A and B are constants to be determined from the boundary conditions. The radial flux will now be divided into two distinct regions,(see Figure 2). The first extends from $r = 0$ to $r = R_F$ with the boundary conditions $\phi(0) = 1$ and $\phi(R_F) = 1$, that is a perfectly flat flux distribution normalized to 1.0. $\phi_1(r) = 1$, where the subscript 1 denotes region one, obviously satisfies these requirements. In region two, $R_F < r < R_c$, the boundary conditions are

$$\phi(R_F) = 1 \qquad (4.5)$$

$$\phi(R_E) = 0 \qquad (4.6)$$

$$\frac{d\phi(R_F)}{dr} = 0 \qquad (4.7)$$

Expression (4.6) assumes the monotonically decreasing flux takes the value zero at a radius, R_E, greater than the radius, R_c, of the fuelled core but as yet unknown. Expression (4.7) is the zero leakage from region one condition. The radial buckling of region two is β_2^2. Substituting (4.4) into (4.5), (4.6) and (4.7) yields

$$AJ_o(\beta_2 R_F) + BY_o(\beta_2 R_F) = 1 \tag{4.8}$$

$$AJ_o(\beta_2 R_E) + BY_o(\beta_2 R_E) = 0 \tag{4.9}$$

$$-AJ_1(\beta_2 R_F) - BY_1(\beta_2 R_F) = 0 \tag{4.10}$$

Eliminating A from (4.8) and (4.9), results in

$$B = \frac{J_o(\beta_2 R_E)}{Y_o(\beta_2 R_F)\,J_o(\beta_2 R_E) - Y_o(\beta_2 R_E)\,J_o(\beta_2 R_F)}$$

Substituting this into (4.9) results in

$$A = \frac{Y_o(\beta_2 R_E)}{J_o(\beta_2 R_F)\,Y_o(\beta_2 R_E) - Y_o(\beta_2 R_F)\,J_o(\beta_2 R_E)}$$

Expression (4.4) now becomes, for region two

$$\phi_2(r) = \frac{Y_o(\beta_2 R_E)\,J_o(\beta_2 r) - J_o(\beta_2 R_E)\,Y_o(\beta_2 r)}{Y_o(\beta_2 R_E)\,J_o(\beta_2 R_F) - Y_o(\beta_2 R_F)\,J_o(\beta_2 R_E)} \tag{4.11}$$

Also, from (4,9) and (4.10), the relation

$$\frac{J_o(\beta_2 R_E)}{Y_o(\beta_2 R_E)} = \frac{J_1(\beta_2 R_F)}{Y_1(\beta_2 R_F)} \tag{4.12}$$

is obtained. Note β_2 and R_E are as yet unknown quantities.

The average to maximum radial power form factor is from the actual flux distribution of the reflected reactor shown in Figure 2, $\phi_p = 0.85$, where ϕ_p is the symbol for the form factor. This will be equated with the power form factor derived using expression (4.11) for the thermal flux. The power is directly proportional to the flux in the fuelled portion of the reactor, and so

$$\frac{\int_0^{R_c} 2\pi r\, \phi(r)\, dr}{\int_0^{R_c} 2\pi r\, dr} = 0.85 \qquad (4.13)$$

after the flux has been normalized to a maximum value of 1.0 and, as before, R_c is the radius of the fuelled core. After substituting (4.11) into (4.13) and employing (4.12) as well, the two unknowns β_2 and R_E can be solved for using an iterative technique. These are evaluated in Appendix 1 and are found to be $\beta_2 = 1.119 \times 10^{-2}$ and $R_E = 393$ cm.

The one-group diffusion equation for the higher flux modes can be written for the radial flux distribution as

$$\nabla^2 \phi_{ij}(r) + (K_o^2 + \lambda_{ij}^2)\, \phi_{ij}(r) = 0 \qquad (4.14)$$

where K_o^2 is the radial Laplacian of the fundamental mode, and is identical to β^2. λ_{ij}^2 is the difference between the buckling of the ijth mode and the fundamental. If $\lambda_{ij}'^2$ is the buckling of this higher mode flux distribution, the relation

$$\lambda_{ij}'^2 = K_o^2 + \lambda_{ij}^2 \qquad (4.15)$$

is evident, and the solution of (4.14) will be identical in form with the solution of (4.3), replacing $\lambda_{ij}^{'2}$ with β^2.

In region one, the buckling of the fundamental mode is zero, so

$$\lambda_{ij}^{'2} = \lambda_{ij}^{2}$$

In region two, (4.15) holds with β_2^2, the radial buckling of zone two replacing K_o^2. For various values of R_F/R_E, the radial buckling differences, λ_{ij}^2, for region two, have been evaluated and tabulated (3)(see Table 4).

In the present case

$$\frac{R_F}{R_E} = \frac{237}{393} = 0.603,$$

$(\lambda_{01}\ R_E)^2$ from Table 4 is 5.24, and so $\lambda_{01}^2 = 3.39 \times 10^{-5}$ for the first azimuthal mode. Similarly, $(\lambda_{02}\ R_E)^2 = 14.25$ yielding $\lambda_{02}^2 = 9.22 \times 10^{-5}$ for the second azimuthal mode. The first radial mode has an even higher value of $(\lambda_{10}\ R_E)^2$ and will be investigated only if the second azimuthal mode proves to be unstable. As mentioned before, the axial flux distribution is $\cos(\alpha z)$ normalized to a maximum flux of 1.0, and where α^2 is the axial buckling, $(\frac{\pi}{H})^2$, of the fundamental mode where H is the length of the reactor core, 600 cm. The first axial mode buckling is $(\frac{2\pi}{H})^2$, and so the buckling difference between the first axial mode and the fundamental is $(4-1)(\frac{\pi}{H})^2 = \lambda_{A1}^2$. Note the higher axial modes have greater λ_A^2 values. With H = 600 cm, λ_{A1}^2 is 8.24×10^{-5}. It can be seen that if this mode proves to be stable so will all the azimuthal modes other than the first and all the radial modes by virtue of their higher λ_{ij}^2 values.

The equilibrium fuel parameters will be evaluated first. An average burnup of the discharged fuel over the entire fuelled core is 9834 MWd/TeU, and the terminal exposure associated with this value of burnup is 2.4 neutrons/Kilo-barn. The irradiation dependent parameters will be extracted from POWDERPUFS-V (4) at this discharge irradiation.

As derived, the stability criterion is

$$\frac{M^2\lambda_{ij}^2}{\alpha_{xe}} - \frac{\alpha_T}{\alpha_{xe}}\phi = f(\phi) \qquad (4.16)$$

where ϕ is the Westcott (2200 m/sec) flux statistically weighted over the core.

$$\hat{\phi}_{eff} = \int_V \phi^3\, dV \Big/ \int_V \phi^2\, dV$$

M^2 is the migration area of the core and, in modified one-group theory, equals the slowing down area L_s^2 plus the diffusion area L_T^2. These values are tabulated in Table 2, and M^2 is found to be 375.29 cm^2.

α_T is the power or temperature coefficient of reactivity usually in units of reactivity per °C, where the temperature is that of the particular component affecting the reactivity. These components are usually considered as comprising the overall temperature coefficient, these are due to temperature changes in fuel, coolant and moderator. Expression (4.16) was derived using simple perturbation theory and is therefore valid only for small deviations in the flux. Since the temperature of the component will be sensitive to these small flux oscillations, it will deviate only slightly from its nominal operating value and α_T must be calculated with this in mind. The coolant and moderator changes are second order effects and for small deviations in flux are completely negligible compared to the fuel temperature coefficient. Since α_T, for the present study must be in units of reactivity per unit flux, the following technique will be used to evaluate it. In Figure 4, the reactivity change versus a change in fuel temperature from its nominal operating value of 870°C is plotted. In order that α_T be representative of small deviations in flux, a tangent is drawn to the curve at the origin and the slope of this line will give a first approximation to α_T. The flux is assumed to be Westcott, statistically weighted value of $\hat{\phi}_{eff} = 10.11 \times 10^{13}$ neutrons/cm^2-sec at the operating fuel temperature of 870°C. The flux is assumed to decrease to zero when the fuel temperature reaches the coolant temperature fo 274°C, a change of 596°C. The system reactivity change from Figure 4 for this change in fuel temperature is -1.6 milli-k. The slope of the tangent after converting to the correct units of α_T is

$$\frac{-1.6 \times 10^{-3}}{596°\text{C}} \times \frac{596°\text{C}}{10.11 \times 10^{13} \text{n/cm}^2\text{-sec}}$$

which is -1.583×10^{-17} in reactivity per unit flux.

α_{xe} is defined as the amount of reactivity held by xenon at high flux; in other words, the xenon reactivity load. The related quantity $\Delta k_{eff}/k_{eff}$ is calculated where Δk_{eff} is the change in the effective multiplication constant due to the presence of Xe-135. α_{xe} is related to this value as

$$\alpha_{xe} = -\frac{\Delta k_{eff}}{k_{eff}}$$

This is calculated in Appendix 2, the result being

$$\alpha_{xe} = \frac{f\Delta\Sigma_{aF}}{\Sigma_{aF}} - \frac{B_g^2 L_T^2}{1+B_g^2 L_T^2} \cdot \frac{V_F}{V_C} \cdot \frac{\phi_F}{\phi_C} \cdot \frac{\Delta\Sigma_{aF}}{\Sigma_a^2} \quad (4.17)$$

$\Delta\Sigma_{aF}$ is replaced by the Xe-135 macroscopic absorption cross-section extracted from POWDERPUFS-V(4), at a terminal exposure of 2.4 neutrons/Kilo-barn. Table 5 lists the values of the parameters in this equation. The first item is 28.3 mk, while the second is 0.5 mk, resulting in α_{xe}, the reactivity load at high flux = 0.0278.

γ_{xef} is the yield of Xe-135 from fission of the fuel with terminal exposure 2.4 neutrons/Kilo-barn. Since the fuel is composed of three fissile isotopes

$$\gamma_{xef} = (\nu\,\Sigma_f\,\gamma_{xe})_{U-235} + (\nu\,\Sigma_f\,\gamma_{xe})_{Pu-239} + (\nu\,\Sigma_f\,\gamma_{xe})_{Pu-241} \quad (4.18)$$

The $\nu\Sigma_f$ term is calculated in POWDERPUFS-V(4), normalized to the fresh fuel isotopic abundance of U-238 and is termed "yield". Therefore,

$$\gamma_{xef}(W_T) = \frac{\left(N(\overline{W}_T)\ \hat{\sigma}_f(\overline{W}_T)\ \nu\ \gamma_{xe}\right)_{U\text{-}235}}{\left[N(0)\right]_{U\text{-}238}} + \frac{\left(N(\overline{W}_T)\ \hat{\sigma}_f(\overline{W}_T)\ \nu\ \gamma_{xe}\right)_{Pu\text{-}239}}{\left[N(0)\right]_{U\text{-}238}} + \frac{\left(N(\overline{W}_T)\ \hat{\sigma}_f(\overline{W}_T)\ \nu\ \gamma_{xe}\right)_{Pu\text{-}241}}{\left[N(0)\right]_{U\text{-}238}} \qquad (4.19)$$

See Table 5 for the numerical values of the three terms on the left-hand side of (4.19).

The quantity μ_{xef}, the fractional Xe-135 yield from the fission of the fuel mixture is

$$\mu_{xef} = \frac{\gamma_{xef}}{\gamma_{xef} + \gamma_{If}} \qquad (4.20)$$

and for equilibrium fuel conditions has the value 0.096.

The quantity

$$f(\emptyset) = \frac{\dfrac{1}{1 + \lambda_{xe} / \sigma_{xe}\emptyset} - \mu_{xe}}{1 + (\lambda_{xe} + \lambda_I) / \sigma_{xe}\ \emptyset}$$

is rearranged for the purpose of calculation as

$$f(\emptyset) = \frac{(\sigma_{xe}\ \emptyset)^2}{\left\{\sigma_{xe}\emptyset + \lambda_{xe}\right\}\left\{\sigma_{xe}\emptyset + \lambda_{xe} + \lambda_I\right\}} - \frac{\mu_{xef}\ \sigma_{xe}\ \emptyset}{\left\{\sigma_{xe}\emptyset + \lambda_{xe} + \lambda_I\right\}} \qquad (4.21)$$

The former is designated as $f(\overset{1}{\phi})$ and $f(\overset{2}{\phi})$ in the calculations. The following iterative procedure was followed. A value for the flux was guessed at and $f(\phi)$ evaluated. Using the stability criterion

$$\phi^* = \frac{M^2 \lambda_{ij}^2}{\alpha_T} - \frac{\alpha_{xe}}{\alpha_T} f(\phi) \qquad (4.22)$$

a new flux ϕ^* was calculated. The two fluxes were then compared and the process continued until the two values of flux were identical. Table 6 lists these iterations for equilibrium and fresh fuel. For the fresh fuel case, α_T and α_{xe} are different in value but are calculated in the same manner. See Figure 4 for the variation in system reactivity with fresh fuel temperature changes.

For the equilibrium fuel case, a flux of 2.689×10^{13} neutrons/cm^2-sec was found to satisfy the stability criterion. Instability due to undampened X-135 oscillations is therefore possible at

$$\frac{2.689 \times 10^{13} \times 10^{2}}{10.11 \times 10^{13}} = 26.6 \text{ percent}$$

of full power in the first azimuthal mode. The second azimuthal mode was investigated employing the stability criterion

$$\phi = \frac{M^2 \lambda^2_{02}}{\alpha_T} - \frac{\alpha_{xe}}{\alpha_T} f(\phi) \qquad (5.1)$$

The first term is negative while the second term is positive. Stability for all flux levels occurs if the flux calculated from (5.1) is negative when the highest possible value of $f(\phi)$ is employed. This value of $f(\phi)$ occurs for infinite flux and is found to be

$$1 - \mu_{xe} = 0.904$$

after taking the limit of (4.21) as flux approaches infinity. $\lambda^2_{02} = 9.22 \times 10^{-5}$ and the flux calculated from 4.22 is -6×10^{14}, indicating a stable system. Since larger values of λ^2_{ij} succeeds only in pushing the flux to greater negative values, all other azimuthal and radial modes are stable. In the first axial mode $\lambda^2_{11} = 8.24 \times 10^{-5}$, the flux calculated from (5.1) employing $f(\phi) = 0.904$, is -3.7×10^{14} neutrons/cm^2-sec indicating the first axial mode is stable as well as all other axial modes.

For fresh fuel, a flux of 2.52×10^{13} neutrons/cm^2-sec satisfied the stability criterion indicating that xenon instability would occur at

$$\frac{2.52 \times 10^{13} \times 10^{2}}{10.11 \times 10^{13}} = 24.9 \text{ percent}$$

of full power. The second azimuthal mode when investigated using (5.1) with $f(\phi)$ equal to

$$1 - \mu_{xe} = 1 - 0.0341 = 0.9659$$

and α_T and α_{xe} corresponding to the fresh fuel values proved to be stable since ϕ was -6.1×10^{13} neutrons/cm^2-sec. The first axial mode also proved stable since $\phi = -3.8 \times 10^{14}$ neutrons/cm^2-sec. All higher azimuthal, axial, and radial modes are thus stable in the fresh fuel condition.

All the quantities in the stability criterion (5.1) are known design quantities except λ_{ij}^2. This was calculated for a reactor flux distribution of a bare rather than a reflected reactor. This parameter depends on flux shape and, as mentioned previously, this was thought to be of secondary importance. The predominant factor was flux level. To find out just how sensitive flux shape was on stability, another case was carried out with R_E fixed at the radius at which the actual reflected reactor flux distribution went to zero. An R_F and β_2 are then found by solving (4.12) and each pair of parameters inserted in (4.13) until an R_F and β_2 consistent with both equations are found. The steps in this iterative procedure are listed in Table 7. Values of $R_F = 208.5$ cm and $\beta_2 = 8.3 \times 10^{-3}$ were found.

$$\frac{R_F}{R_E} = \frac{208.5}{426} = 0.491; \quad (\lambda_{01} R_E)^2 = 6.00; \quad \text{and}$$

$$\lambda_{01}^2 = 3.31 \times 10^{-5}$$

When this value of λ_{01}^2 was used in the equilibrium fuel case, keeping all other parameters constant, (see Table 8 for the steps in the iterative process) a flux level of 2.574×10^{13} neutrons/cm^2-sec was found to satisfy the stability criterion, or

$$\frac{2.574 \times 10^{13} \times 10^2}{10.11 \times 10^{13}} = 25.5 \text{ percent}$$

of full power. This is very close to the value 26.6 percent for a different flux shape supporting the claim that the shape of the flux is relatively unimportant in computing a flux level at which instability occurs. It also provides a reliable lower limit on this instability level without having to define a flattened radius initially. An R_E can be used equal to that extrapolated radius of the actual reflected distribution and then an R_F and β_2 consistent with (4.12) and (4.13) can be solved for (see Tables 6 and 8)

6. REACTOR DESCRIPTION - PICKERING

The physical dimensions of the Pickering reactor are smaller than in Bruce, the total number of channels being 390 compared to 480 for the latter. The core radius corresponding to 390 channels is 318.4 cm, and the length of each channel is 594.4 cm. The channel lattice pitch of 28.575 cm remains the same for the two reactor configurations although the actual composition of a channel differs from one reactor to the other (see Table 1). Table 9 contains other pertinent core data.

With Bruce, the actual radial flux distribution, although possessing the characteristic rise in thermal flux at the boundary between the reflector and the core, was actually quite flat over a radius not greatly different from the radius of zone one, and this shape did not vary axially. Therefore, a flattened radius was easily defined and a radius R_E was then solved for by equating flux form factors for the actual and the analytically derived distribution.

The Pickering flux distribution is flattened by the introduction of adjuster rods, not by a variation in fuel burnup. As a result, the flux distribution experiences depressions both radially and axially near these rods and peaking between two adjacent ones. Further away from the rods, the flux is smoothened considerably. See Figures 5 and 6 for the radial and axial flux shapes, respectively. The effect of this flux distribution on a neutron is similar to the flattened distribution since in both cases a neutron does not tend to diffuse out of the central core region. However, it is very difficult to define a flattened radius which would have the same overall physical effect as these distributions shown in Figures 5 and 6. In Bruce, it was found that the threshold power level did not vary markedly with flux shape; if an extrapolated radius R_E was chosen to be equal to the radius at which the actual reflected distribution went to zero and then an R_F was solved for by equating power form factors, the threshold power level was only one percent lower than the other technique. Therefore, it is assumed that a lower limit on the power threshold for Pickering can be found by setting R_E = 389 cm, which is the reflected reactor flux distribution zero-flux radius, and by equating power form factors, an R_F representative of the actual flux distribution could be found.

A second method of evaluation R_F was also employed. This involved trying to find a representative value of R_F initially, keeping in mind that the shape of the flux in the radial direction varied at each axial position. Clearly what was needed were the power levels in each channel integrated along the axis of the reactor (see Figure 7). It is seen that the integrated channel powers increase in the horizontal direction to a maximum before falling off in the direction of the core boundary. In the vertical direction, a steady decrease in channel powers is evident from the horizontal centerline to the bottom of the core boundary, at first gradually and then more rapidly. An effective flattened radius, R_F, was determined by equating the total area in which a neutron does not tend to diffuse outward from the central core region to πR_f^2. The crossed line in Figure 7 describes what is thought to be a good approximation of the flattened area. R_F calculated from this area was found to be 168.3 cm.

In the axial direction, also, the flux experiences flattening due to the presence of the adjuster rods. What was done in this case was to assume that this flux could be replaced by a flattened cosine distribution. An analytical expression for the flux was developed and assuming an extrapolated length, z_E, equal to one half the actual extrapolated height of 604 cm, and equating the axial flux form factors in the core of the actual and the analytically derived distributions, a representative flattened length, z_F, of 45.1 cm was calculated. It was assumed that this method would provide a lower limit on the instability threshold for the first axial mode.

As in Bruce, the fuelling scheme is a once-through bi-directional loading and the terminal irradiation and corresponding fuel burnup are constant over the entire core (see Table 9 for values). Thus, a single fuel composition is employed over the entire core and the power distribution is direction proportional to the thermal flux. The flattening is achieved, therefore, in a different manner to Bruce. Eighteen vertical adjuster rods having a high absorption cross-section for thermal neutrons are employed to trim the flux. Figure 5 shows the exact position of these rods. The three pronounced dips in the thermal flux distribution in a plane through the adjuster rods are the result of the presence of these rods. The overall effect, near the rods, as shown in Figure 5, is a flattened flux distribution. These flux maps were extracted from the two-group neutron diffusion code WHIRLAWAY-IV (9) for the reflected Pickering reactor. The lattice parameters used in the calculations are the time averaged ones calculated by POWDERPUFS (4) and, as in Bruce, the microscopic cross-sections follow the Westcott convention. The reaction rates used in calculating the lattice parameters are obtained as before by averaging the macroscopic cross-sections over the channel exposure distribution for a discharge exposure of 1.8 neutrons/Kilo-barn. The same averaging convention is employed. The radial power form factor is 0.791 while the axial direction is 0.702, giving an overall power form factor of 0.556.

An identical analysis to that developed in the section on calculations for the Bruce reactor leads to expressions (7.1) and (7.2).

$$\emptyset_2(r) = \frac{Y_o(\beta_2 R_E)\, J_o(\beta_2 r) - J_o(\beta_2 R_E)\, Y_o(\beta_2 r)}{Y_o(\beta_2 R_E)\, J_o(\beta_2 R_F) - Y_o(\beta_2 R_F)\, J_o(\beta_2 R_E)} \qquad (7.1)$$

$$\frac{J_o(\beta_2 R_E)}{Y_o(\beta_2 R_E)} = \frac{J_1(\beta_2 R_F)}{Y_1(\beta_2 R_F)} \qquad (7.2)$$

The radial power form factor, as calculated for the actual reflected reactor flux distribution, is 0.791. Therefore, it is possible to write

$$\frac{\int_o^{R_c} 2\pi r\, \emptyset(r)\, dr}{\int_o^{R_c} 2\pi r\, dr} = 0.791 \qquad (7.3)$$

where flux has been normalized to a maximum value of 1.0.

In the section on Reactor Description, it was mentioned that two methods were to be employed. The first assumes an R_E, and (7.2) and (7.3) are solved iteratively to find values of the other unknown parameters β_2 and R_F. The second assumes an R_F can be defined as in the case of Bruce, and β_2 and R_E are found by solving (7.2) and (7.3) simultaneously. See Appendix 3 for the calculation of these parameters for the two methods. Method one produces a value of $R_F = 147$ cm, and $\beta_2 = 7.8 \times 10^{-3}$ for an $R_E = 389$ cm; while the second method yields for an $R_F = 168.3$ cm, values of $\beta_2 = 9.3 \times 10^{-3}$ and $R_E = 365$ cm. The parameters λ_{ij}^2 as defined in the section on calculations for the Bruce reactor were evaluated from Hitchcock(3) (see Table 4). For the first method

$$\frac{R_F}{R_E} = \frac{147}{389} = 0.378; \qquad (\lambda_{01} R_E)^2 = 6.846 \text{ and } \lambda_{01}^2 = 4.52 \times 10^{-5}$$

for the first azimuthal mode. In the case of the second azimuthal mode,

$$(\lambda_{02} R_E)^2 = 17.61 \quad \text{and} \quad \lambda_{02}^2 = 1.166 \times 10^{-4}$$

In the first radial mode

$$(\lambda_{01} R_E)^2 = 25.69 \quad \text{and} \quad \lambda_{10}^2 = 1.7 \times 10^{-4}$$

The first radial mode will be investigated only if the second azimuthal mode proves to be unstable. For the second method

$$\frac{R_F}{R_E} = \frac{168.3}{365} = 0.461; \qquad (\lambda_{01} R_E)^2 = 6.21 \quad \text{and} \quad \lambda_{01}^2 = 4.66 \times 10^{-5}$$

The higher modes will be investigated only if method one proves them to be unstable, since method one provides a lower limit on the threshold power value.

In the axial direction the flux is determined from

$$\nabla^2 \phi(z) + B_n^2 \phi(z) = 0 \tag{7.4}$$

The general solution of this equation in the axial direction is

$$\phi(z) = A\,\mathrm{SIN}(B_n z) + B\cos(B_n z) \tag{7.5}$$

where A and B are constants to be determined from the boundary conditions.

Since the flux is symmetrical in the axial direction, $z = 0$ is taken to be the reactor centre, while the physical boundary of the core is at $z_E = 297.2$ cm. $\phi(z)$ is obviously equal to 1.0 in zone one extending from $z = 0$ to $z = z_F$, which is the flattened flux length. The boundary conditions in zone two are

$$\emptyset(z_F) = 1.0 \qquad (7.6)$$

$$\emptyset(z_E) = 0 \qquad (7.7)$$

$$\frac{d\emptyset}{dz}(z_F) = 0 \qquad (7.8)$$

The last three expressions become, after substituting for $\emptyset(z)$ from (7.5)

$$A\ \mathrm{SIN}(B_n\ z_F) + B\ \mathrm{COS}(B_n\ z_F) = 1 \qquad (7.9)$$

$$A\ \mathrm{SIN}(B_n\ z_E) + B\ \mathrm{COS}(B_n\ z_E) = 0 \qquad (7.10)$$

$$AB_n\ \mathrm{COS}(B_n\ z_F) - BB_n\ \mathrm{SIN}(B_n\ z_F) = 0 \qquad (7.11)$$

On dividing (7.10) and (7.11), the expression analogous to (7.2) is obtained,

$$\frac{\mathrm{SIN}(B_n\ z_E)}{\mathrm{COS}(B_n z_F)} = -\frac{\mathrm{COS}(B_n z_E)}{\mathrm{SIN}(B_n z_F)}$$

which can be rearranged to yield

$$\frac{\mathrm{SIN}(B_n\ z_E)}{\mathrm{COS}(B_n\ z_E)} = -\frac{\mathrm{COS}(B_n\ z_F)}{\mathrm{SIN}(B_n\ z_F)} \qquad (7.12)$$

From (7.10)

$$A = \frac{-B\ \mathrm{COS}(B_n\ z_E)}{\mathrm{SIN}(B_n\ z_E)}$$

and, substituting into (7.5)

$$\frac{-B\ \mathrm{COS}(B_n\ z_E)\ .\ \mathrm{SIN}(B_n\ z_F)}{\mathrm{SIN}(B_n\ z_E)} + B\ \mathrm{COS}(B_n\ z_F) = 1$$

and $$B = \frac{\mathrm{SIN}(B_n z_E)}{\mathrm{SIN}(B_n z_E)\ \mathrm{COS}(B_n z_F) - \mathrm{COS}(B_n z_E)\ \mathrm{SIN}(B_n z_F)}$$

and therefore

$$A = \frac{-\ \mathrm{COS}(B_n z_E)}{\mathrm{SIN}(B_n z_E)\ \mathrm{COS}(B_n z_F) - \mathrm{COS}(B_n z_E)\ \mathrm{SIN}(B_n z_F)}$$

Therefore, finally

$$\emptyset_2(z) = \frac{\mathrm{COS}(B_n z)\ \mathrm{SIN}(B_n z_E) - \mathrm{SIN}(B_n z)\ \mathrm{COS}(B_n z_E)}{\mathrm{SIN}(B_n z_E)\ \mathrm{COS}(B_n z_F) - \mathrm{COS}(B_n z_E)\ \mathrm{SIN}(B_n z_F)} \qquad (7.13)$$

The axial power form factor is 0.702 and the expression analogous to (7.3) is

$$\frac{2.\int_0^{z_c} \emptyset(z).dz}{2.\int_0^{z_c} dz} = 0.702 \qquad (7.14)$$

where (7.13) is used for $\emptyset(z)$. In this case z_E is set equal to the value of z at which the actual flux distribution goes to zero. This value is 302 cm. A z_F and B_n are found that satisfy (7.12). Each pair is then tested to see if it satisfies expression (7.14). See Appendix 4 for the evaluation of (7.14) and the iterative scheme employed. z_F and B_n were found to be 45.1 cm and 0.00611, respectively. The parameter λ_{11}^2 for the first axial mode is found in the following way. Reference (1) lists for a one-dimensional pile the parameter $\Lambda_j = \lambda_{11}^2 / B_g^2$ plotted versus the percent flatness for a flattened sinusoidal flux distribution.

$$\frac{z_F}{z_E} = \frac{45.1}{302} = 0.149 = 14.9 \text{ percent flat.}$$

Λ_1 = 2.625 from the graph in Reference (1). $\lambda_{11}^2 = 2.625 \times B_g^2$, where

$$B_g^2 = \left(\frac{\pi}{H_c}\right)^2 = \left(\frac{\pi}{594.4}\right)^2 = 2.79 \times 10^{-5}$$

for a one-dimensional pile. Therefore, $\lambda_{11}^2 = 7.32 \times 10^{-5}$.

The other parameters appearing in equation (4.16) are evaluated next.

M^2, the migration area, is equal to the sum of the thermal diffusion area L_T^2 and the slowing down area L_s^2.

$$M^2 = L_T^2 + L_s^2 = 221.31 + 154.96 = 376.27 \text{ cm}^2$$

α_{xe}, the xenon load at high flux is from Figure 8 for the equilibrium fuel case 0.028. This is also the value for the fresh fuel condition.

α_T, for the fresh fuel condition is calculated by a method analogous to that used in Bruce. Figure 9 shows a graph of system reactivity versus change in fuel temperature from its nominal operating value of 730°C. The coolant temperature at zero flux is 249°C, and so for a fuel temperature change from this temperature, 249°C to its nominal operating value 730°, a change of 481°C, the flux increases from zero to its operating statistically weighted Westcott value of 8.236×10^{13} neutrons/cm^2-sec. From Figure 9, drawing a tangent to the curve at the origin since we are considering small deviations in fuel temperature as in Bruce. The slope of this line, converting to the units of reactivity per unit flux yields α_T.

$$\alpha_T = \frac{-7.4 \times 10^{-3}}{481°\text{C}} \times \frac{481°\text{C}}{8.236 \times 10^{13}} \text{ neutrons/cm}^2\text{-sec}$$

$$= -8.985 \times 10^{-17}$$

Similarly, for the equilibrium fuel condition α_T was calculated to be

$$\alpha_T = \frac{-2.6 \times 10^{-3}}{481°\text{C}} \times \frac{481°\text{C}}{8.236 \times 10^{13}} \text{ neutrons/cm}^2\text{-sec}$$

$$= -3.157 \times 10^{-17}$$

To facilitate a check of the numerical results with the power threshold computed from SORGHUM(11), a computer code which simulates reactor startup and is sensitive to Xe-135 oscillations, α_T was set equal to zero and the calculations for an instability threshold repeated.

μ_{xe}, the fractional xenon yield was found by a method analogous to the one used in Bruce to be 0.0866 for the equilibrium fuel case, and 0.0341 for the fresh fuel case. See Table 11 for a resume of the pertinent parameters.

For the equilibrium fuel case concerning oscillations in the first azimuthal mode, $R_F = 147$ cm, $R_E = 389$ cm and $\lambda_{01}^2 = 4.52 \times 10^{-5}$. From Table 12, a flux of 6.5×10^{13} neutrons/cm^2-sec satisfied the stability criterion, and the corresponding power level is

$$\frac{6.5 \times 10^{13} \times 10^2}{8.236 \times 10^{13}} = 78.9 \text{ percent}$$

of full power. The second method employed with $R_F = 168.3$ cm, $R_E = 365$ cm and $\lambda_{01}^2 = 4.66 \times 10^{-5}$ resulted in a threshold flux level of 7.94×10^{13} neutrons/cm^2-sec, or

$$\frac{7.94 \times 10^{13} \times 10^2}{8.236 \times 10^{13}} = 96.4 \text{ percent}$$

of full power. These results confirm the assumption based on the results from Bruce. Setting an R_E equal to the extrapolated radius of the actual flux distribution for the reflected reactor results in a lower limit on the threshold power level for instability. The first axial mode using $R_F = 45.1$ cm, $R_E = 302$ cm and $\lambda_{11}^2 = 7.32 \times 10^{-5}$ proved to be stable. The result should be valid, since z_E was set equal to the value 302 cm, which is the zero flux half-height for the actual flux distribution of the reflected reactor, and it has already been shown that adopting this method gives a lower limit on the instability threshold. Since λ_{02}^2 and λ_{10}^2 for the second azimuthal and first radial modes are greater than λ_{11}^2 for the first axial mode which is stable, and since $f(\emptyset)$ is a monotonically increasing function, these higher modes will also be stable.

In the fresh fuel condition, α_T is more negative than the equilibrium fuel case and, as previously mentioned, this is a stabilizing effect, and it is expected that the threshold power level for instability will be higher than the corresponding values for equilibrium fuel. When a computer program was run (no listing is given since it is essentially the same as that listed in Appendix 6 with α_T non-zero), it was found that no flux level satisfied the stability criterion, indicating the fresh fuel condition to be stable in all modes.

With $\alpha_T = 0$ and the equilibrium fuel case condition, a short computer program listed in Appendix 5 is used to solve

$$f(\emptyset) = \frac{M^2 \lambda_{ij}^2}{\alpha_{xe}} \tag{8.1}$$

A flux of 4.538×10^{13} neutrons/cm^2-sec was found to be the instability flux threshold employing $R_F = 147$ cm, $R_E = 389$ cm and $\lambda_{01}^2 = 4.52 \times 10^{-5}$, that is method one, and the power level is 55 percent of full power. The second method with $R_F = 168.3$ cm, $R_E = 365$ cm and $\lambda_{01}^2 = 4.66 \times 10^{-5}$ resulted in a threshold flux level of 4.946×10^{13} neutrons/cm^2-sec, or 60 percent of full power.

9. CONCLUSIONS AND RECOMMENDATIONS

The qualitative arguments in the introductory section of this report as to why Xe-135 oscillations might lead to an unstable situation in the Bruce and Pickering reactors have been, as a first approximation, substantiated.

In the equilibrium fuel condition, the Bruce reactor was found to be unstable in the fundamental and first azimuthal modes, while stable operation was assured in the higher azimuthal, radial and axial modes.

The fresh fuel condition was also found to be unstable only in the modes cited for the equilibrium fuel condition, but the margin against instability was larger as it was found that these modes were unstable at a slightly higher power level.

For Pickering, the modes were stable against Xe-135 oscillations in all but the fundamental and first azimuthal modes in the equilibrium fuel condition. For fresh fuel, only the fundamental mode was unstable.

The results also substantiated the premise that the power level at which instability occurred depended mainly on the flux size and only secondarily on flux shape. In the Bruce reactor, as the flattened radius was varied from 208.5 to 237 cm, a 13 percent change, the power threshold for Xe-135 instability varied about 5 percent. For Pickering, as the flattened radius was varied from 147 cm to 168.3 cm, a 12 percent change, the power threshold level varied about 15 percent.

It was stated that the more negative the fuel temperature power coefficient, the more stable the system would be against Xe-135 oscillations. In Bruce, the fresh fuel condition was unstable at a higher power level than the equilibrium fuel condition, since here the α_T value was more negative than the equilibrium α_T value. In Pickering, where α_T is also more negative in the fresh fuel condition, the reactor was found to be unstable for equilibrium fuel yet stable for fresh fuel.

In Section 7 it was stated that the threshold power level was to be calculated for the case $\alpha_T = 0$ for equilibrium fuel, to facilitate a check of numerical results with SORGHUM (11). In section 8 the calculations led to a predicted instability power threshold of 60 percent. The computer results (12) show the power threshold for instability to be in fact only slightly higher than this predicted value. With this close agreement in this particular case, it is assumed the other predicted instability thresholds are good approximations of those for the actual physical system.

It is recommended that to improve the accuracy of these calculations, the cross terms $\bar{\emptyset}_{ij}$ and $\bar{X}_{ij}$, which were neglected because of the orthogonality of the eigen-functions g_i, be evaluated by some numerical-integration technique. These are in fact identically zero only for a perfectly flat flux distribution. For flux distributions which differ substantially from the fundamental geometrical distribution, $\lambda_{ij}^2 = \Lambda_j B_g^2$ is found from

$$\nabla^2 g_j + B^2 g_j + \Lambda_j B_g^2 g_j = 0 \qquad \text{(C1)}$$

where B^2 is the space-dependent materials buckling. The fundamental flux distribution $g_o (\Lambda_o = 0)$ can be determined by iteration techniques for which high speed computer codes exist. Modification is required to adapt these codes to determine Λ_1 and g_1 (13).

a_T the dependence of the buckling on the flux could take into account the secondary effects due to variation in reactivity with moderator temperature and also changes in reactivity with coolant temperature, both of which were neglected in this analysis as negligible compared to the variation in reactivity with fuel temperature.

C1 is only a one-energy group diffusion equation describing the problem. A two-energy group approach could be adapted to a computer solution of the problem and a stability criterion dependent on both fast flux and thermal flux would result.

As a final check on the results, the actual startup of these reactors will determine the actual power level at which they would become unstable with respect to Xe-135, since control action will be initiated at a power level such that these modal oscillations are suppressed.

10. REFERENCES

(1) Randall and St. John: "Xenon Spatial Oscillations", Nucleonics, March 1958.

(2) Ward, A.G.: "The Problem of Flux Instability in Large Power Reactors", CRRP-657.

(3) Hitchcock, A: "Nuclear Reactor Stability", Temple Press, 1960.

(4) Loken, P.C.: "The Physics of POWDERPUFS-IV-V Lattice Parameter Program", AECL Report TDAI-31, April 1969.

(5) Bruce Safety Report, AECL, August 1970.

(6) Bowen and Masters: "Nuclear Reactor Control and Instrumentation".

(7) Galanin: "Thermal Reactor Theory".

(8) "Bessel Functions Part I" British Association Math. Tables.

(9) Fowler, T.B. and Tobias, M.K.: "WHIRLAWAY - A Three-dimensional, Two-group Neutron Diffusion Code for the IBM 7090 Computer", Report No. ORNL-3150.

(10) Duret, M.F. and Marriott, R.: "POOOFBURN - A Computer Program for Reactor Studies", AECL Report No. 911, October 1959.

(11) SORGHUM - Code for Evaluating Methods of Control of Spatial Flux Distribution in a Large Reactor, With Xe-135, After a Perturbation.

(12) Trojan, O.A.: Private communication.

(13) Pearce, R.M. and Roth, R.E.: "XENOSC - A G-20 Programme for Studying Xenon Spatial Oscillations and Applications to CANDU", AECL 1803, July 1963.

APPENDIX 1

Evaluation of β_2 and R_E

In Figure 2, the power distribution is directly proportional to the flux in region two and then suffers a jump discontinuity, as it passes the boundary of region one and region two, to a lower proportionality constant. This is due in the actual reactor to a difference in fuel composition between the two regions, the macroscopic fission cross-section times the energy per fission of the fuel mixture having a lesser value in region one. If power varies directly as flux in zone 2, it will vary in zone 1 as the flux times the ratio of the fission cross-sections and energy per fission of the two fuel mixtures. The ratio is 0.98, and therefore we have power directly proportional to 0.98 times the flux in region one.

Expression (4.13) takes the form

$$\frac{\int_{0}^{R_F} 2\pi r(0.98\, \emptyset_1(r))dr + \int_{R_F}^{R_c} 2\pi r\, \emptyset_2(r)\, dr}{\pi R_c^2} = 0.85$$

when $\emptyset(r)$ is broken up into its respective parts.

$$0.98\,\frac{R_F^2}{R_c^2} + \frac{2}{R_c^2}\int_{R_F}^{R_c} \emptyset_2(r).rdr = 0.85 \qquad \text{(A1.1)}$$

$$\int_{R_F}^{R_c} \emptyset_2(r).rdr = \left\{ 0.85 - 0.98\,\frac{R_F^2}{R_c^2} \right\} \frac{R_c^2}{2} \qquad \text{(A1.2)}$$

When the right-hand side of (A1.2) is evaluated from the core data in Table 2, it is found to have a value of 2.54×10^4. With $\phi_2(r)$ equal to the expression (4.11), the left-hand side of (A1.1) becomes

$$\int_{R_F}^{R_c} \left\{ \frac{J_o(\beta_2 r)\ Y_o(\beta_2 R_E) - Y_o(\beta_2 r)\ J_o(\beta_2 R_E)}{J_o(\beta_2 R_F)\ Y_o(\beta_2 R_E) - Y_o(\beta_2 R_F)\ J_o(\beta_2 R_E)} \right\} r dr \qquad \text{(A1.3)}$$

Denoting the denominator by the constant Q, (A1.3) can be rewritten

$$\left\{ \frac{Y_o(\beta_2 R_E)}{Q} \times \frac{1}{\beta_2^2} \int_{\beta_2 R_F}^{\beta_2 R_c} X\ J_o(X)\,dX \right\} - \left\{ \frac{J_o(\beta_2 R_E)}{Q} \times \frac{1}{\beta_2^2} \int_{\beta_2 R_F}^{\beta_2 R_c} X\ Y_o(X)\,dX \right\}$$

This is further simplified:

$$\frac{Y_o(\beta_2 R_E)}{Q\ \beta_2^2} \left\{ X\ J_1(X) \Bigg|_{\beta_2 R_F}^{\beta_2 R_c} \right\} - \frac{J_o(\beta_2 R_E)}{Q\ \beta_2^2} \left\{ X\ Y_1(X) \Bigg|_{\beta_2 R_F}^{\beta_2 R_c} \right\}$$

$$\frac{R_c}{\beta_2} \left\{ \frac{Y_o(\beta_2 R_E)\ J_1(\beta_2 R_c) - J_o(\beta_2 R_E)\ Y_1(\beta_2 R_c)}{Q} - \frac{Y_o(\beta_2 R_E)\ J_1(\beta_2 R_F) - J_o(\beta_2 R_E)\ Y_1(\beta_2 R_F)}{Q} \right\}$$

The second expression within the brackets is found to be zero from the boundary condition,

$$\frac{\partial \phi(R_F)}{\partial r} = 0,$$

the zero leakage from region 1 condition. Thus $J_1(\beta_2 R_F)\ Y_o(\beta_2 R_E) - Y_1(\beta_2 R_F)\ J_o(\beta_2 R_E) = 0$ after multiplying through by $\frac{Q}{\beta_2}$.

The left-hand side of (A1.2) is now

$$\frac{R_c}{\beta_2}\left\{\frac{Y_o(\beta_2R_E)\ J_1(\beta_2R_c)\ -\ J_o(\beta_2R_E)\ Y_1(\beta_2R_c)}{J_o(\beta_2R_F)\ Y_o(\beta_2R_E)\ -\ Y_o(\beta_2R_F)\ J_o(\beta_2R_E)}\right\} \qquad \text{(A1.4)}$$

The unknown parameters β_2 and R_E are found by solving (4.12) and (A1.4) by an iterative procedure as follows. A value of R_E was chosen and (4.12) was solved for a β_2. With these two values (A1.4) was evaluated and compared with 2.54×10^4. See Table 3 for the steps in the iterative process. Values of β_2 and R_E equal to 1.119×10^{-2} and 393 cm, respectively were quickly found to satisfy both conditions.

APPENDIX 2

Evaluation of $\alpha_{xe} = \left|\frac{\Delta k_{eff}}{k_{eff}}\right|$

k_{eff} for a finite thermal reactor is $\eta f P_T$, and so evaluating $\frac{\Delta k_{eff}}{k_{eff}}$ by logarithmic differences results in

$$\frac{\Delta k_{eff}}{k_{eff}} = \frac{\Delta \eta f}{\eta f} + \frac{\Delta P_T}{P_T} \qquad \text{(A2.1)}$$

Consider the first term on the right-hand side of (A2.1)

$$\eta = \frac{\nu \Sigma_f}{\Sigma_{aF}}$$

$$f = \frac{\phi_F V_F \Sigma_{aF}}{\phi_F V_F \Sigma_{aF} + \phi_R V_R \Sigma_{aR}}$$

where the subscripts F stand for fuel, and R stands for the rest of the cell, other than fuel.

$$\eta f = \frac{\nu \Sigma_{fF} \phi_F V_F}{\phi_F V_F \Sigma_{aF} + \phi_R V_R \Sigma_{aR}}$$

$$\frac{\Delta \eta f}{\eta f} = \frac{-(\nu \Sigma_{fF} \phi_F V_F) \phi_F V_F \Delta\Sigma_{aF}}{(\phi_F V_F \Sigma_{aF} + \phi_R V_R \Sigma_{aR})^2} \times \left\{\frac{\phi_F V_F \Sigma_{aF} + \phi_R V_R \Sigma_{aR}}{\nu \Sigma_{fF} \phi_F V_F}\right\}$$

$$= \frac{-\phi_F V_F \Delta\Sigma_{aF}}{(\phi_F V_F \Sigma_{aF} + \phi_R V_R \Sigma_{aR}}$$

$$= \frac{-f \Delta\Sigma_{aF}}{\Sigma_{aF}} \qquad \text{(A2.2)}$$

where we are considering changes in ηf due to changes in the macroscopic absorption cross-section of the fuel to the presence of xenon poison. Now consider the second term on the right-hand side of (A2.1)

$$P_T = (1 + L_T^2 B_g^2)^{-1}$$

$$\frac{\Delta P_T}{P_T} = \frac{-B_g^2 \, \Delta L_T^2 \, (1 + L_T^2 B_g^2)}{(1 + L_T^2 B_g^2)^2}$$

$$= \frac{-\Delta L_T^2}{L_T^2} \left\{ \frac{B_g^2 L_T^2}{1 + L_T^2 B_g^2} \right\} \qquad (A2.3)$$

Now $L_T^2 = \frac{D}{\Sigma_a^2}$, so in (A2.3), where the superscript 2 denotes thermal

$$\frac{\Delta L_T^2}{L_T^2} = \frac{-\Delta \Sigma_a^2 \, D}{(\Sigma_a^2)^2} \times \frac{\Sigma_a^2}{D}$$

$$= \frac{-\Delta \Sigma_a^2}{\Sigma_a^2} \qquad (A2.4)$$

in (A2.4)

$$\Sigma_a^2 = \frac{\phi_F V_F \Sigma_{aF} + \phi_R V_R \Sigma_{aR}}{V_c \phi_c}$$

where c stands for the cell = F + R.

$$\frac{\Delta \Sigma_a^2}{\Sigma_a^2} = \frac{\phi_F V_F \Delta \Sigma_{aF}}{\phi_c V_c \Sigma_a^2}$$

and finally

$$\frac{\Delta P_T}{P_T} = \left\{ \frac{-B_g^2 L_T^2}{1 + B_g^2 L_T^2} \right\} \cdot \left\{ \frac{-V_F}{V_c} \frac{\phi_F}{\phi_c} \frac{\Delta\Sigma_{aF}}{\Sigma_a^2} \right\}$$

$$\alpha_{xe} = \frac{\Delta\eta f}{\eta f} + \frac{\Delta P_T}{P_T}$$

$$\frac{f\Delta\Sigma_{aF}}{\Sigma_{aF}} - \left(\frac{B_g^2 L_T^2}{1 + B_g^2 L_T^2}\right)\left(\frac{V_F \phi_F \Delta\Sigma_{aF}}{V_c \phi_c \Sigma_a^2}\right)$$

where f is the thermal utilization of the fuel; Σ_{aF} is the macroscopic cross-section of the fuel; $\Delta\Sigma_{aF}$ is the macroscopic cross-section for absorption by Xe-135; B_g^2 is the geometric buckling of the core; L_T^2 is the diffusion length of the thermal neutrons; V_F is the volume of the fuel; ϕ_F is the flux in the fuel, while V_c and ϕ_c are the corresponding quantities for the core; Σ_a^2 is the macroscopic thermal absorption cross-section for the cell. See Table 5 for the values of these parameters.

APPENDIX 3

Evaluation of β_2 and R_E

Since in Pickering there is only one fuel composition across the core, the power is directly proportinal to the flux both in the flattened zone and zone two. Expression (7.3) becomes

$$\frac{\int_{o}^{R_F} 2\pi r\, \phi_1(r)\, dr + \int_{R_F}^{R_c} 2\pi r\, \phi_2(r)\, dr}{\pi R_c^2} = 0.791$$

$$\int_{R_F}^{R_c} \phi_2(r)\, dr = \left\{ 0.791 - \frac{R_F^2}{R_c^2} \right\} \frac{R_c^2}{2} \qquad \text{(A3.1)}$$

As in Appendix 1, the left-hand side of this expression is

$$\frac{R_c}{\beta_2} \left\{ \frac{Y_o(\beta_2 R_E)\, J_1(\beta_2 R_c) - J_o(\beta_2 R_E)\, Y_1(\beta_2 R_c)}{J_o(\beta_2 R_F)\, Y_o(\beta_2 R_E) - Y_o(\beta_2 R_F)\, J_o(\beta_2 R_E)} \right\}$$

Method One:

Here R_E = 389 cm is assumed. A value of R_F and β_2, consistent with equation 7.2 is found and then, employing these three parameters, the left- and right-hand sides of (A3.1) are compared. This is repeated until a value of R_F and β_2, consistent with (7.2) and (A3.1), are found. Table 10 lists the steps in the iterative process. A value of R_F = 147 cm and β_2 = 0.0078 satisfied these criteria.

Method Two:

This method involves equating the area thought to be a representative flattened area to the area of a circle πR_F^2. The total flattened area from Figure 7 for one quarter of the reactor geometry is 27.25 lattice cells each of area $(28.575)^2$ cm^2. R_F was calculated to be 168.3 cm. R_E and β_2, consistent with (7.2) were now found and inserted in (A3.1) to see if they satisfied the power criterion. The steps in this procedure are listed in Table 10. Values of R_E = 365 cm and β_2 = 0.0093 were quickly found to satisfy these criteria.

APPENDIX 4

Evaluation of Z_F and B_A

Expression (7.14) can be written with $\emptyset_1(z)$ normalized to 1.0 and $\emptyset_2(z)$ given by (7.13)

$$\frac{\int_o^{z_F} \emptyset_1(z)\,dz + \int_{z_F}^{z_c} \emptyset_2(z)\,dz}{\int_o^{z_c} dz} = 0.702$$

$$\int_{z_F}^{z_c} \emptyset_2(z)\,dz = \left\{ 0.702 - \frac{z_F}{z_c} \right\} z_c \qquad \text{(A4.1)}$$

The left-hand side of this last expression is evaluated next

$$\frac{1}{K} \left\{ \int_{z_F}^{z_c} \cos(B_n z)\,\sin(B_n z_E)\,dz - \int_{z_F}^{z_c} \sin(B_n z)\,\cos(B_n z_E)\,dz \right\}$$

where $K = \sin(B_n z_E)\,\cos(B_n z_F) - \cos(B_n z_E)\,\sin(B_n z_F)$.

This expression is further reduced to

$$\frac{1}{K} \left\{ \frac{1}{B_n} \left[\sin(B_n z_c)\,\sin(B_n z_E) - \sin(B_n z_F)\,\sin(B_n z_E) \right] \right.$$

$$\left. + \frac{1}{B_n} \left[\cos(B_n z_c)\,\cos(B_n z_E) - \cos(B_n z_F)\,\cos(B_n z_E) \right] \right\}$$

Grouping terms, this becomes

$$\frac{1}{B_n K}\left\{ \mathrm{SIN}(B_n z_E)\ \mathrm{SIN}(B_n z_c) + \mathrm{COS}(B_n z_c)\ \mathrm{COS}(B_n z_E) \right\}$$

$$-\ \frac{1}{B_n K}\left\{ \mathrm{SIN}(B_n z_F)\ \mathrm{SIN}(B_n z_E) + \mathrm{COS}(B_n z_E)\ \mathrm{COS}(B_n z_F) \right\}$$

The second expression in brackets is zero from the zero leakage condition at $z = z_F$. Therefore, finally (A4.1) is rearranged

$$\frac{\mathrm{SIN}(B_n z_E)\ \mathrm{SIN}(B_n z_c) + \mathrm{COS}(B_n z_c)\ \mathrm{COS}(B_n z_E)}{\mathrm{SIN}(B_n z_E)\ \mathrm{COS}(B_n z_F) - \mathrm{COS}(B_n z_E)\ \mathrm{SIN}(B_n z_F)} \equiv \left(0.702 - \frac{z_F}{z_c}\right) \cdot B_n z_c \qquad (A4.2)$$

Expressions (7.12) and (A4.2) are solved using a short computer program. The listing is as follows: (z_F = 45.1 cm and β_A = 0.00611 were found)

```
            PHI  =  0.702
            EPS  =  0.009
            ZC  =  297.2
            ZE  =  302.0
            ZF  =  20.0
            BN  =  0.0050
   20       CONTINUE
            DO 10 I  =  1,500
            X  =  BN * ZE
            Y  =  BN * ZF
            A  =  SIN(X) / COS(X)
            B  =  COS(Y) / SIN(Y)
            WRITE (6,100)  A, B, BN, ZF
```

```
100      FORMAT  (4 (3X, F10.5))
         IF  (ABS  (A + B). LE. EPS)  GO TO 1000
         BN  =  BN + 0.000001
10       CONTINUE
         WRITE  (6,200)
200      FORMAT  (6H    ERROR)
         IF  (ZF. GE. 200)  GO TO 30
         ZF  =  ZF + 0.5
         BN  =  BN - 0.0002
         GO TO 20
1000     Z  =  BN * ZC
         C  =  (PHI - ZF/ZC) * Z
         D  =  (SIN(X) * SIN(Z) + COS(Z) * COS(X))/ (SIN(X) * COS(Y)
              - COS(X) * SIN(Y))
         WRITE (6,300) C,D.
300      FORMAT (2 (10X, F10.5)
         ZF  =  ZF + 0.5
         IF  (ZF. GE. 200) GO TO 30
         GO TO 20
30       CONTINUE
         STOP .
         END.
```

APPENDIX 5

Solution of (A5.1)

The following is the listing of the short computer program to solve

$$f(\emptyset) = \frac{M^2 \lambda_{ij}^2}{\alpha_{xe}} \qquad (A5.1)$$

```
         M  =  0
         PHI  =  1.00
         XM2  =  376.27
         XLAM2  =  0.0000452
         ALFAX  =  0.028
         RIGHT  =  XM2 * XLAM2 / ALFAX
         DO 10  I  =  1,724
50       XF1  =  ((3.5 * PHI) ** 2.) / ((3.5 * PHI + 2.09)
                 * (3.5 * PHI + 4.96))
         XF2  =  (3.5 * PHI * 0.0866) / (3.5 * PHI + 4.96 )
         XF  =  XF1 - XF2
         WRITE (6,100)  XF1, XF2, XF, RIGHT, PHI
100      FORMAT (5 (3X, F10.5))
         IF (M. EQ. 0)  PHI  =  PHI + 0.01
         IF (M. EQ. 1)  PHI  =  PHI + 0.001
         IF (ABS (XF - RIGHT)  .LE. 0.0001)   GO TO 20
         IF (M. EQ. 1)  GO TO 10
         IF (ABS (XF - RIGHT). LE. 0.005)  TO TO 30
10       CONTINUE
```

```
30      CONTINUE
        PHI =  PHI - 0.01
        M  =  1
        GO TO 50
20      CONTINUE
        STOP
        END.
```

TABLE 1

Comparison of Bruce and Pickering Lattices

Lattice Component	Material		Dimensions	
	Bruce	Pickering	Bruce	Pickering
Fuel	Nat. UO_2 (0.7257 atom %) U-235	Nat. UO_2 (0.7257 atom %) U-235	Volume = 42.932 cm^3/cm Pellet Radius = 0.7165 cm	Volume = 42.932 cm^3/cm Pellet Radius = 0.7165 cm
Sheath	Zr-2	Zr-2	IR = 0.719 cm OR = 0.760 cm Volume = 6.362 cm^3/cm	IR = 0.719 cm OR = 0.760 cm Volume = 6.362 cm^3/cm
Coolant	D_2O (99.75 atom %) Purity	D_2O (99.722 atom %) Purity	Volume = 33.706 cm^3/cm	Volume = 33.252 cm^3/cm
Pressure Tube	Zr-Nb	Zr-2 (Units 1 & 2) Zr-Nb (Units 3 & 4)	IR = 5.183 cm OR = 5.564 cm Volume = 12.863 cm^3/cm	IR = 5.169 cm OR = 5.667 cm Volume = 16.947 cm^3/cm
Gas Annulus	Air	Air	IR = 5.564 cm OR = 6.447 cm Volume = 33.33 cm^3/cm	IR = 5.667 cm OR = 6.550 cm Volume = 33.90 cm^3/cm
Calandria Tube	Zr-2	Zr-2	IR = 6.447 cm OR = 6.547 cm Volume = 4.148 cm^3/cm	IR = 6.550 cm OR = 6.705 cm Volume = 6.454 cm^3/cm
Moderator	D_2O (99.75 atom %) Purity	D_2O (99.722 atom %) Purity	Volume = 681.829 cm^3/cm Lattice Pitch = 28.575 cm	Volume = 675.324 cm^3/cm Lattice Pitch = 28.575 cm

TABLE 2

Core Data - Bruce

R_F	237 cm
R_E	393 cm
R_c	353 cm
Number of Channels in Zone 1	216
Number of Channels in Zone 2	264
Length of Channel	600 cm
Lattice Pitch	28.575 cm
Discharge Irradiation of Zone 1	2.96 neutrons/Kilo-barn
Discharge Irradiation of Zone 2	2.06 neutrons/Kilo-barn
L_s^2	153.65 cm^2
L_T^2	221.64 cm^2
$M^2 = L_s^2 + L_T^2$	375.29 cm^2
Power to Coolant (Zone 1)	1185.9 MW
Power to Coolant (Zone 2)	1189.1 MW
Power to Coolant (total)	2375.0 MW
Total Thermal Fission Power	2515.0 MW
$\phi_{eff} = \int_V \phi^3 \, dV / \int_V \phi^2 \, dV$	10.11×10^{13} neutrons/cm^2-sec
Power Form Factor (Radial)	0.85
Power Form Factor (Axial)	0.649
Coolant Temperature (Zone 1)	274 °C

TABLE 2 (continued)

Coolant Temperature (Zone 2)	280 °C
Fuel Operating Temperature	870 °C

TABLE 3

Steps In Iterative Solution of (4.12) and (A1.4) For R_E and β_2

R_E	β_2	$Y_o(\beta_2 R_E)$	$J_1(\beta_2 R_c)$	$J_o(\beta_2 R_E)$	$Y_1(\beta_2 R_c)$	$J_o(\beta_2 R_F)$	$Y_o(\beta_2 R_F)$	(A1.4)
432	0.908×10^{-2}	0.011	0.257	-0.401	0.373	0.133	0.520	2.82×10^{4}
390	1.138×10^{-2}	-0.176	-0.074	-0.334	0.396	-0.142	0.461	2.52×10^{4}
392	1.125×10^{-2}	-0.167	-0.055	-0.340	0.401	-0.129	0.467	2.53×10^{4}
394	1.112×10^{-2}	-0.157	-0.039	-0.346	0.405	-0.115	0.473	2.55×10^{4}
393	1.119×10^{-2}	-0.163	-0.047	-0.342	0.403	-0.120	0.471	2.54×10^{4}

TABLE 4

Values of λR_0 for Values of R_1/R_0

R_1 / R_0	$(\lambda'_{00} R_0)^2$	$(\lambda_{01} R_0)^2$	$(\lambda_{02} R_0)^2$	$(\lambda_{10} R_0)^2$
0.00	5.78	8.90	20.59	24.69
0.02	5.79	8.89	20.58	24.71
0.04	5.82	8.86	20.56	24.74
0.06	5.86	8.82	20.51	24.80
0.08	5.92	8.76	20.46	24.86
0.10	5.99	8.69	20.38	24.95
0.12	6.08	8.61	20.29	25.05
0.14	6.19	8.51	20.18	25.16
0.16	6.31	8.40	20.06	25.28
0.18	6.46	8.28	19.92	25.40
0.20	6.62	8.16	19.77	25.51
0.22	6.80	8.02	19.59	25.61
0.24	7.00	7.88	19.40	25.71
0.26	7.23	7.74	19.20	25.79
0.28	7.48	7.59	18.97	25.85
0.30	7.76	7.44	18.74	25.89
0.32	8.06	7.29	18.49	25.89
0.34	8.39	7.14	18.23	25.86
0.36	8.77	6.99	17.96	25.80
0.38	9.18	6.83	17.67	25.71
0.40	9.65	6.67	17.38	25.58
0.42	10.14	6.52	17.08	25.39
0.44	10.71	6.37	16.78	25.16

TABLE 4 (continued)

R_1 / R_0	$(\lambda'_{00} R_0)^2$	$(\lambda_{01} R_0)^2$	$(\lambda_{02} R_0)^2$	$(\lambda_{10} R_0)^2$
0.46	11.14	6.22	16.47	24.90
0.48	12.06	6.07	16.15	24.61
0.50	12.87	5.93	15.84	24.29
0.52	13.72	5.79	15.52	23.93
0.54	14.70	5.65	15.21	23.56
0.56	15.86	5.52	14.89	23.17
0.58	17.22	5.39	14.58	22.76
0.60	18.83	5.26	14.27	22.34
0.62	20.31	5.14	13.97	21.91
0.64	22.19	5.02	13.68	21.48
0.66	24.61	4.91	13.39	21.04
0.68	27.69	4.80	13.10	20.61
0.70	31.57	4.69	12.82	20.17
0.72	36.7	4.58	12.65	19.74
0.74	42.8	4.47	12.26	19.31
0.76	52.6	4.36	11.98	18.90
0.78	58.1	4.25	11.70	18.50
0.80	67.5	4.14	11.42	18.11

TABLE 5

Parameters From POWDERPUFS-V - Bruce

Parameters	Equilibrium	Fresh
(γ_{xe}) U-235	0.0022	0.0022
(γ_{xe}) Pu-239	0.0109	0.0109
(γ_{xe}) Pu-241	0.0026	0.0026
(γ_{xe}) U-238	0.0019	0.0019
$(\gamma_T = \gamma_{xe} + \gamma_I)$ U-235	0.0645	0.0645
$(\gamma_T = \gamma_{xe} + \gamma_I)$ Pu-239	0.0722	0.0722
$(\gamma_T = \gamma_{xe} + \gamma_I)$ Pu-241	0.0783	0.0783
$(\gamma_T = \gamma_{xe} + \gamma_I)$ U-238	0.062	0.062
Yield U-235 $(N\sigma_f\nu)/(N(0))$ U-238	4.856	0
Yield Pu-239	5.445	0
Yield Pu-241	0.4525	0
Yield U-238	0	0
Total Yield	10.75	0
$\mu_{xe} = \left[\left\{ \left(\frac{\gamma_{xe}}{\gamma_T} \times \text{Yield} \right)_{U-235} + \left(\frac{\gamma_{xe}}{\gamma_T} \times \text{Yield} \right)_{Pu-239} + \left(\frac{\gamma_{xe}}{\gamma_T} \times \text{Yield} \right)_{Pu-241} \right\} \Big/ \text{Yield Total} \right]$	0.096	0.0341

TABLE 5 (continued)

Parameters	Equilibrium	Fresh
ω neutrons/Kilo-barn	2.4	0
f neutrons/Kilo-barn	0.9460	0.94005
$\Sigma_{axe} = \Delta\Sigma_{aF}$ (barns)	0.2747	0.25201
Σ_{aF} (barns)	0.9177×10^{1}	7.7043
Σ_a^2 (cm^{-1})	0.4172×10^{-2}	0.38252×10^{-2}
$< \Sigma_{aF} >$ (cm^{-1})	0.2159	0.18128
V_F (cm^3)	43.261	43.261
V_{cell} (cm^3) = (lattice pitch)^2	816.53	816.53
ϕ_F/ϕ_{cell}	0.50225	0.54425
$\Delta\Sigma_{aF}/\Sigma_a^2$	1.5491	1.550
α_T	-1.583×10^{-17}	-8.902×10^{-17}
α_{xe}	0.0278	0.0302
λ_I (sec^{-1})	2.87×10^{-5}	2.87×10^{-5}
λ_{xe} (sec^{-1})	2.09×10^{-5}	2.09×10^{-5}
σ_{xe} (barns)	3.5×10^{-18}	3.5×10^{-18}

TABLE 6

Solution Iteratively of (4.22)

Equilibrium fuel: $R_F = 393$ cm $\lambda_{01}^2 = 3.39 \times 10^{-5}$

(4.22): $\phi^* = 1.756 \times 10^{15} f(\phi) - 0.8037 \times 10^{15}$

ϕ	$\overset{1}{f}(\phi)$	-	$\overset{2}{f}(\phi)$	=	$f(\phi)$	ϕ^* (from 4.22)
2.5×10^{13}	0.5152	-	0.0613	=	0.4539	NEG
3.0×10^{13}	0.5664	-	0.0652	=	0.5012	7.6×10^{13}
2.75×10^{13}	0.5422	-	0.0634	=	0.4788	3.7×10^{13}
2.6×10^{13}	0.5263	-	0.0621	=	0.4642	1.14×10^{13}
2.7×10^{13}	0.5370	-	0.0630	=	0.4740	2.86×10^{13}
2.69×10^{13}	0.5360	-	0.0629	=	0.4731	2.71×10^{13}
2.68×10^{13}	0.5349	-	0.0628	=	0.4721	2.53×10^{13}
2.689×10^{13}		by	interpolation			2.689×10^{13}

Fresh fuel

$\phi^* = 3.392 \times 10^{14} f(\phi) - 1.429 \times 10^{14}$

ϕ	$\overset{1}{f}(\phi)$	-	$\overset{2}{f}(\phi)$	=	$f(\phi)$	ϕ^*
3.0×10^{13}	0.5664	-	0.0232	=	0.5432	4.14×10^{13}
2.9×10^{13}	0.5570	-	0.0229	=	0.5341	3.83×10^{13}
2.6×10^{13}	0.5263	-	0.0221	=	0.5042	2.81×10^{13}
2.5×10^{13}	0.5152	-	0.0218	=	0.4934	2.45×10^{13}
2.52×10^{13}	0.5174	-	0.0218	=	0.4956	2.52×10^{13}

TABLE 7

Iterative Solution of (4.12) and (A1.4) for R_F and β_2

R_F	β_2	$Y_o(\beta_2 R_E)$	$J_1(\beta_2 R_c)$	$J_o(\beta_2 R_E)$	$Y_1(\beta_2 R_c)$	$J_o(\beta_2 R_F)$	$Y_o(\beta_2 R_F)$	Left-hand Side (A1.2)	Right-hand Side (A1.2)
200	0.00805	0.218	0.396	-0.369	0.277	0.450	0.424	3.24×10^4	3.3×10^4
202	0.0081	0.209	0.389	-0.373	0.283	0.433	0.434	3.23×10^4	3.3×10^4
205	0.0082	0.193	0.379	-0.379	0.293	0.410	0.446	3.19×10^4	3.24×10^4
212	0.0084	0.156	0.350	-0.390	0.316	0.352	0.473	3.12×10^4	3.10×10^4
210	0.0083	0.168	0.365	-0.386	0.305	0.375	0.463	3.15×10^4	3.14×10^4
208.5	0.0083	0.177	0.365	-0.384	0.305	0.375	0.463	3.16×10^4	3.16×10^4

TABLE 8

Solution Iteratively of (4.22)

Equilibrium fuel: $R_E = 426$ cm $\quad \lambda_{01}^2 = 0.0000331$

$$(4.22) \quad \phi^* = 1.756 \times 10^{15} f(\phi) - 0.7847 \times 10^{15}$$

ϕ	$\overset{1}{f}(\phi) - \overset{2}{f}(\phi) =$	$f(\phi)$	ϕ^* (from (4.22))
2.6×10^{13}		0.4642	3.04×10^{13}
2.5×10^{13}		0.4539	1.23×10^{13}
2.57×10^{13}		0.4611	2.50×10^{13}
2.574×10^{13}	by interpolation		2.574×10^{13}

TABLE 9

Core Data - Pickering

R_F = 147 or 168.3 cm

R_E = 389 cm

R_c = 318.4 cm

Number of channels = 390

Length of channel = 390

Lattice pitch = 28.575 cm

Core discharge irradiation = 1.8 neutrons/Kilo-barn

Fuel burnup = 7.45 MWd/KgU

L_s^2 = 154.96

L_T^2 = 221.31

M^2 = $L_s^2 + L_T^2 = 376.27 \text{ cm}^2$

Power form factor (radial) = 0.791

Power form factor (axial) = 0.702

Coolant temperature (operating condition) = 272 °C

Coolant temperature (zero power condition) = 249 °C

Fuel temperature (operating condition) = 730 °C

TABLE 10

Iterative Solution of (4.12) and (A1.4) for β_2 and R_E

Method (2) $R_F = 168.3$ $R_c = 318.4$

R_E	β_2	$Y_o(\beta_2 R_E)$	$J_1(\beta_2 R_c)$	$J_o(\beta_2 R_E)$	$Y_1(\beta_2 R_c)$	$J_o(\beta_2 R_F)$	$Y_o(\beta_2 R_F)$	Left-hand Side of (A3.1)	Right-hand Side of (A3.1)
360	0.0095	0.222	0.332	-0.368	0.330	0.455	0.420	2.56×10^4	2.60×10^4
365	0.0093	0.238	0.354	-0.361	0.314	0.472	0.410	2.60×10^4	2.60×10^4

Method (1) $R_E = 389$ cm $R_c = 318.4$ cm

R_F	β_2	$Y_o(\beta_2 R_E)$	$J_1(\beta_2 R_c)$	$J_o(\beta_2 R_E)$	$Y_1(\beta_2 R_c)$	$J_o(\beta_2 R_F)$	$Y_o(\beta_2 R_F)$	Left-hand Side of (A3.1)	Right-hand Side of (A3.1)
147	0.0078	0.367	0.502	-0.270	0.137	0.696	0.196	2.93×10^4	2.93×10^4

Table 11

Parameters From POWDERPUFS-V - Pickering

Parameters	Equilibrium	Fresh
γ_{xef} (U-235)	0.0022	0.0022
γ_{xef} (Pu-239)	0.0109	0.0109
γ_{xef} (Pu-241)	0.0026	0.0026
γ_{xef} (U-238)	0.0019	0.0019
$\gamma_T = \gamma_{xe} + \gamma_I$ (U-235)	0.0645	0.0645
$\gamma_T = \gamma_{xe} + \gamma_I$ (Pu-239)	0.0722	0.0722
$\gamma_T = \gamma_{xe} + \gamma_I$ (Pu-241)	0.0783	0.0783
$\gamma_T = \gamma_{xe} + \gamma_I$ (U-238)	0.062	0.062
YIELD^{Pu235} (from POWDERPUFS)	5.653	-
YIELD^{Pu239} (from POWDERPUFS)	4.843	-
YIELD^{Pu241} (from POWDERPUFS)	0.280	-
YIELD^{U238} (from POWDERPUFS)	0	-
$\mu_{xef}(\text{FUEL}) = \dfrac{\left(\dfrac{\gamma_{xef}^{U235}}{\gamma_T^{U235}} \times \text{YIELD}^{U235} + \dfrac{\gamma_{xe}^{Pu239} \times \text{YIELD}^{Pu239}}{\gamma_T^{Pu239}} + \dfrac{\gamma_{xe}^{Pu241} \times \text{YIELD}^{Pu241}}{\gamma_T^{Pu241}}\right)}{\text{YIELD}^{TOTAL}} \quad \dfrac{0.9332}{10.776} =$	0.0866	0.0341

TABLE 11 (continued)

Parameters	Equilibrium	Fresh
ω neutrons/Kilo-barn	1.18	0
α_T	0	-8.985×10^{-17}
α_{xe}	0.028	0.028
λ_I	2.87×10^{-5} sec^{-1}	2.87×10^{-5} sec^{-1}
λ_{xe}	2.09×10^{-5} sec^{-1}	2.09×10^{-5} sec^{-1}
σ_{xe}	3.5 c 10^{-18} cm^2	3.5×10^{-18} cm^2

TABLE 12

Solution Iteratively of (4.22)

Method 2

Equilibrium fuel $R_F = 168.3$ cm $R_E = 365$ cm $\lambda_{01}^2 = 4.66 \times 10^{-5}$

$$\phi^* = 8.869 \times 10^{14} f(\phi) - 5.554 \times 10^{14}$$

ϕ	$\overset{1}{f}(\phi)$	-	$\overset{2}{f}(\phi)$	=	$f(\phi)$	ϕ^*
5.0×10^{13}	0.6960	-	0.0675	=	0.6285	2×10^{12}
7.0×10^{13}	0.7663	-	0.0720	=	0.6943	6.04×10^{13}
7.5×10^{13}	0.7790	-	0.0728	=	0.7062	7.09×10^{13}
8.0×10^{13}	0.7929	-	0.0736	=	0.7193	8.25×10^{13}
7.82×10^{13}	0.7865	-	0.0733	=	0.7132	7.71×10^{13}
7.92×10^{13}	0.7888	-	0.0735	=	0.7153	7.90×10^{13}
7.94×10^{13}			by interpolation			7.94×10^{13}

Power threshold $\dfrac{7.94 \times 10^{13} \times 10^{2}}{8.236 \times 10^{13}} = 96.4$ percent

TABLE 12 (continued)

Method 1

Equilibrium fuel $R_F = 147$ cm $R_E = 389$ cm $\lambda_{01}^2 = 4.52 \times 10^{-5}$

$$\phi^* = 8.869 \times 10^{14} f(\phi) - 5.387 \times 10^{14}$$

ϕ	$\overset{1}{f}(\phi)$	-	$\overset{2}{f}(\phi)$	=	$f(\phi)$	ϕ^*
6.6×10^{13}	0.7544	-	0.0713	=	0.6836	6.76×10^{13}
6.5×10^{13}	0.7519	-	0.0711	=	0.6808	6.51×10^{13}

$$\text{Power threshold } \frac{6.5 \times 10^{13} \times 10^2}{8.236 \times 10^{13}} = 78.9 \text{ percent}$$

Figure 1

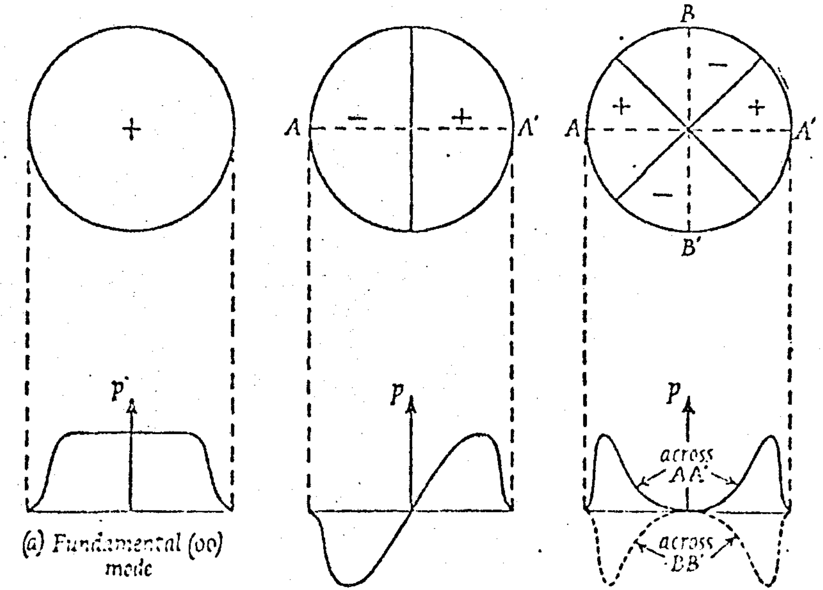

(a) Fundamental (00) mode

(b) First azimuthal (01) mode

(c) Second azimuthal (02) mode ("hot cross bun")

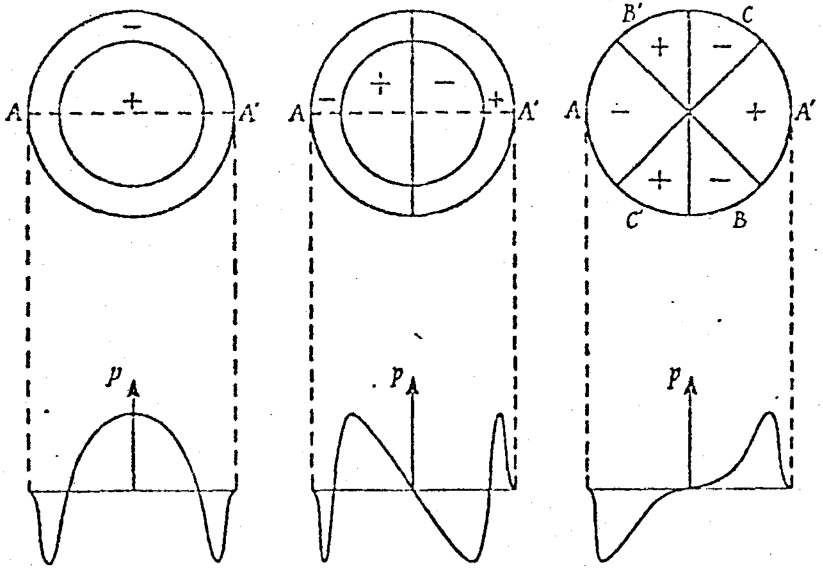

(d) First radial (10) mode ("doughnut")

(e) (11) Mode

(f) Third azimuthal (03) mode

FIG. 1 *Form of variations in different modes.* (See opposite page.)

Figure 2.

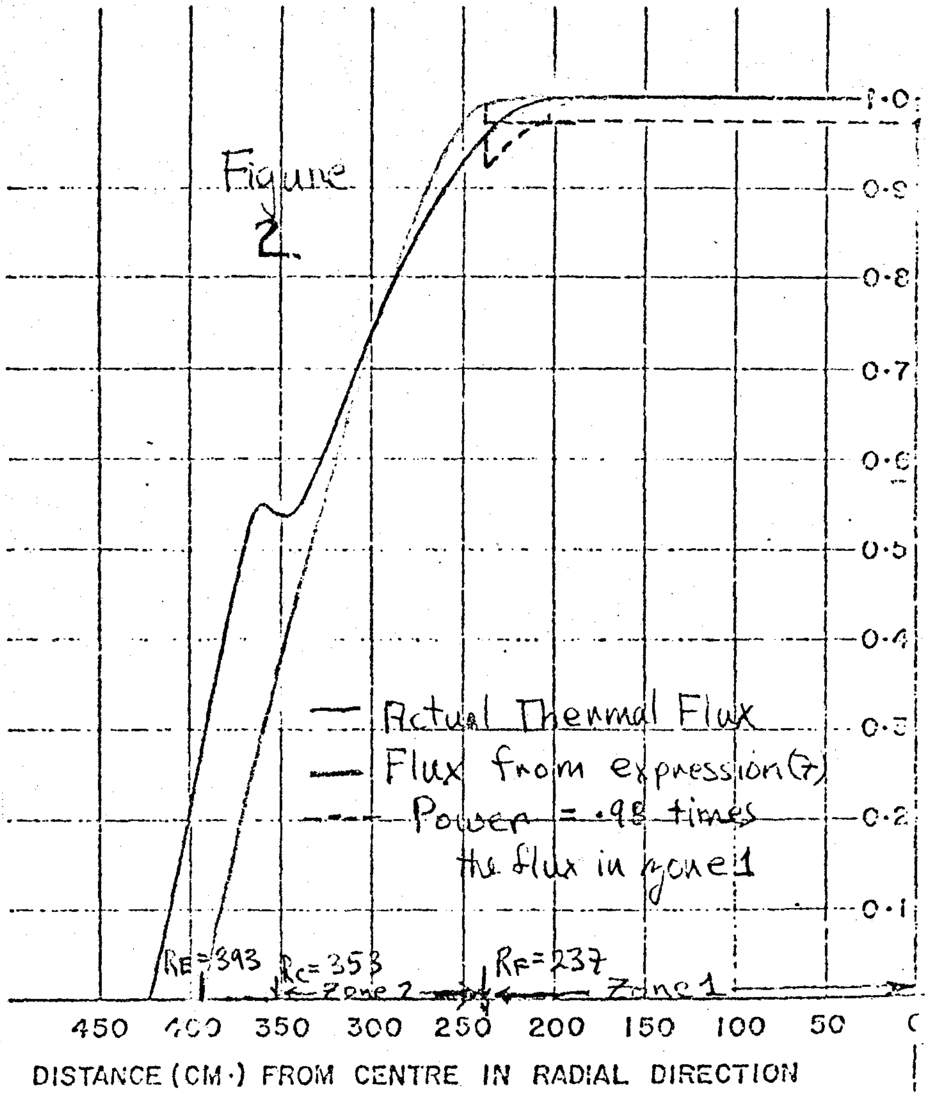
1·0
0·9
0·8
0·7
0·6
0·5
0·4
0·3
0·2
0·1
Actual Thermal Flux
Flux from expression(7)
Power = ·98 times the flux in zone 1
RE = 393
RC = 353
RF = 237
Zone 2
Zone 1
450
400
350
300
250
200
150
100
50
0
DISTANCE (CM·) FROM CENTRE IN RADIAL DIRECTION

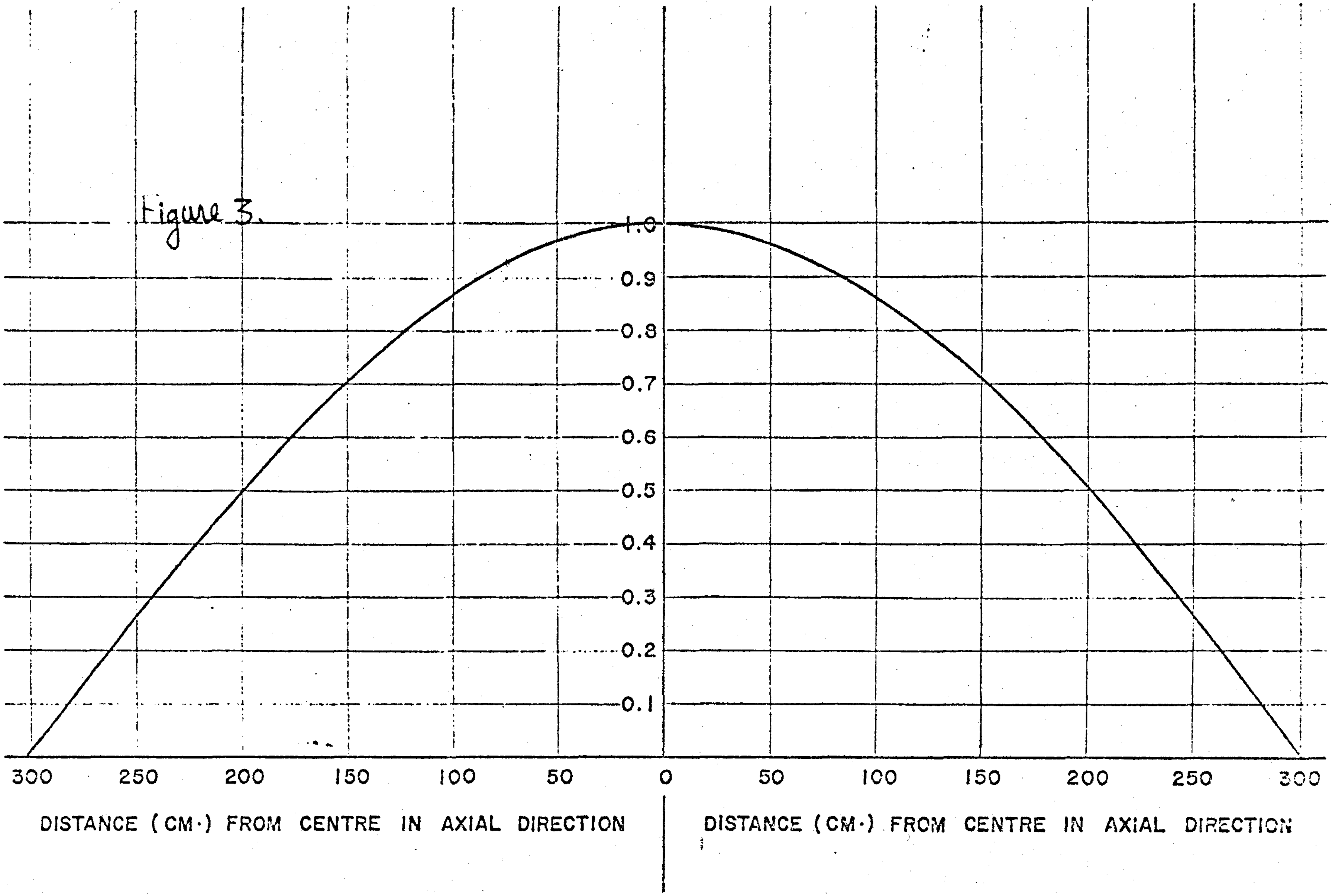

FIG 10·2·2·2. NORMALIZED AXIAL THERMAL NEUTRON FLUX AND POWER

(Reference Section 10, Preliminary Safety Report — Dou[illegible]

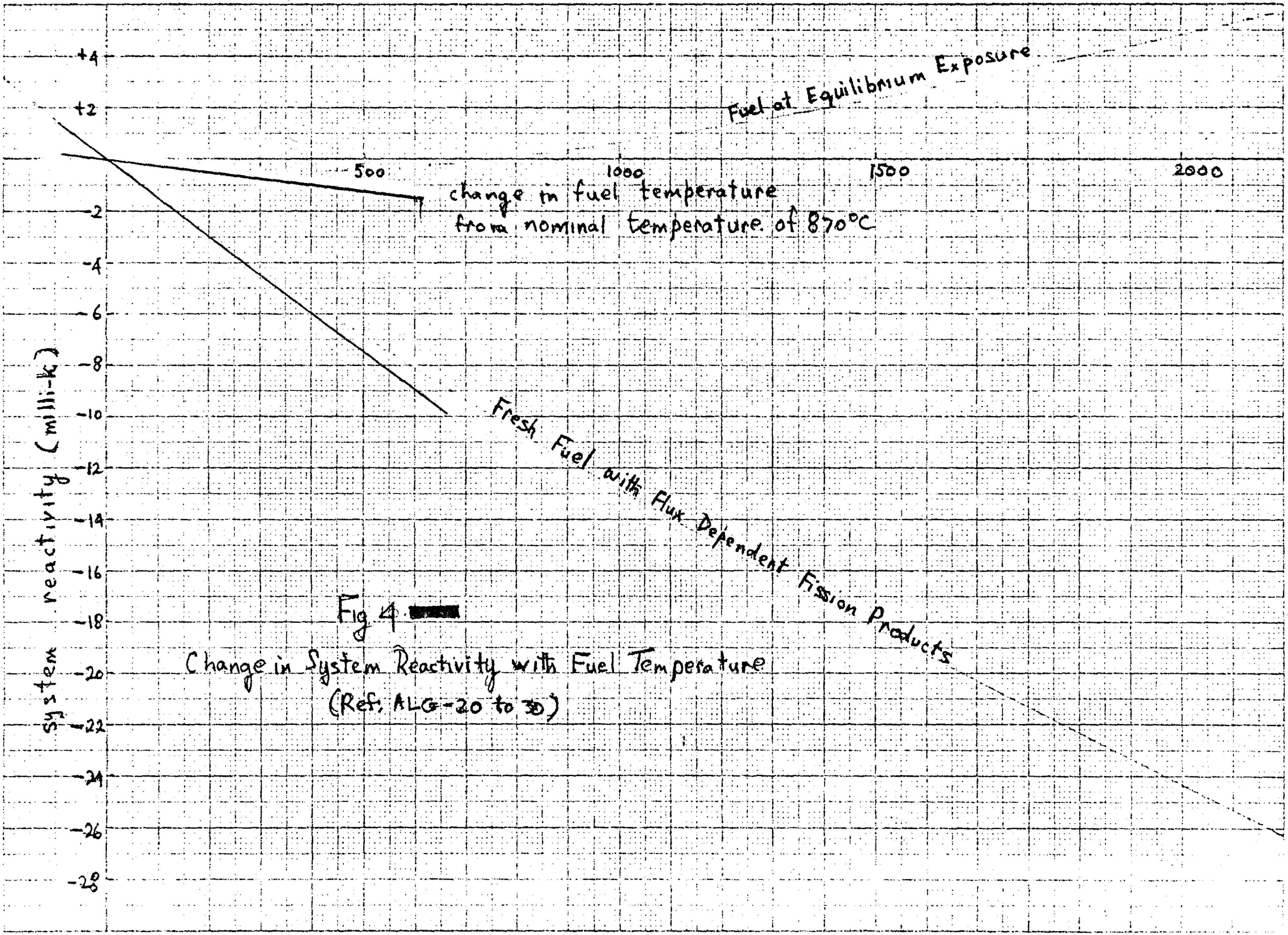

Fig 4 [redacted]

Change in System Reactivity with Fuel Temperature
(Ref. ALG-20 to 30)

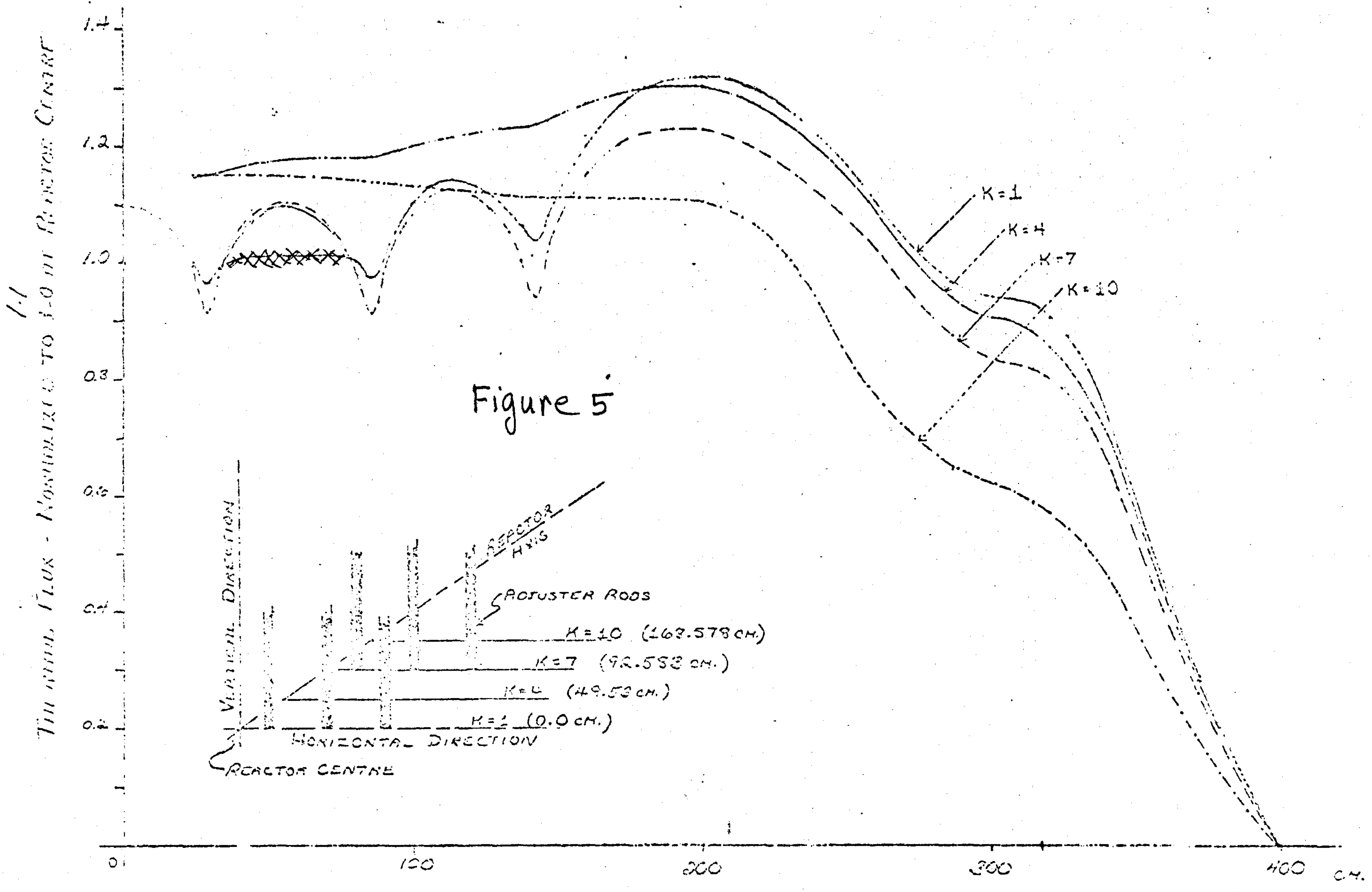

Figure 5

Radial Distance in Horizontal Direction

FIGURE ~~2.2.1~~5 NORMALIZED THERMAL FLUX DISTRIBUTION IN RADIAL, HORIZONTAL DIRECTION

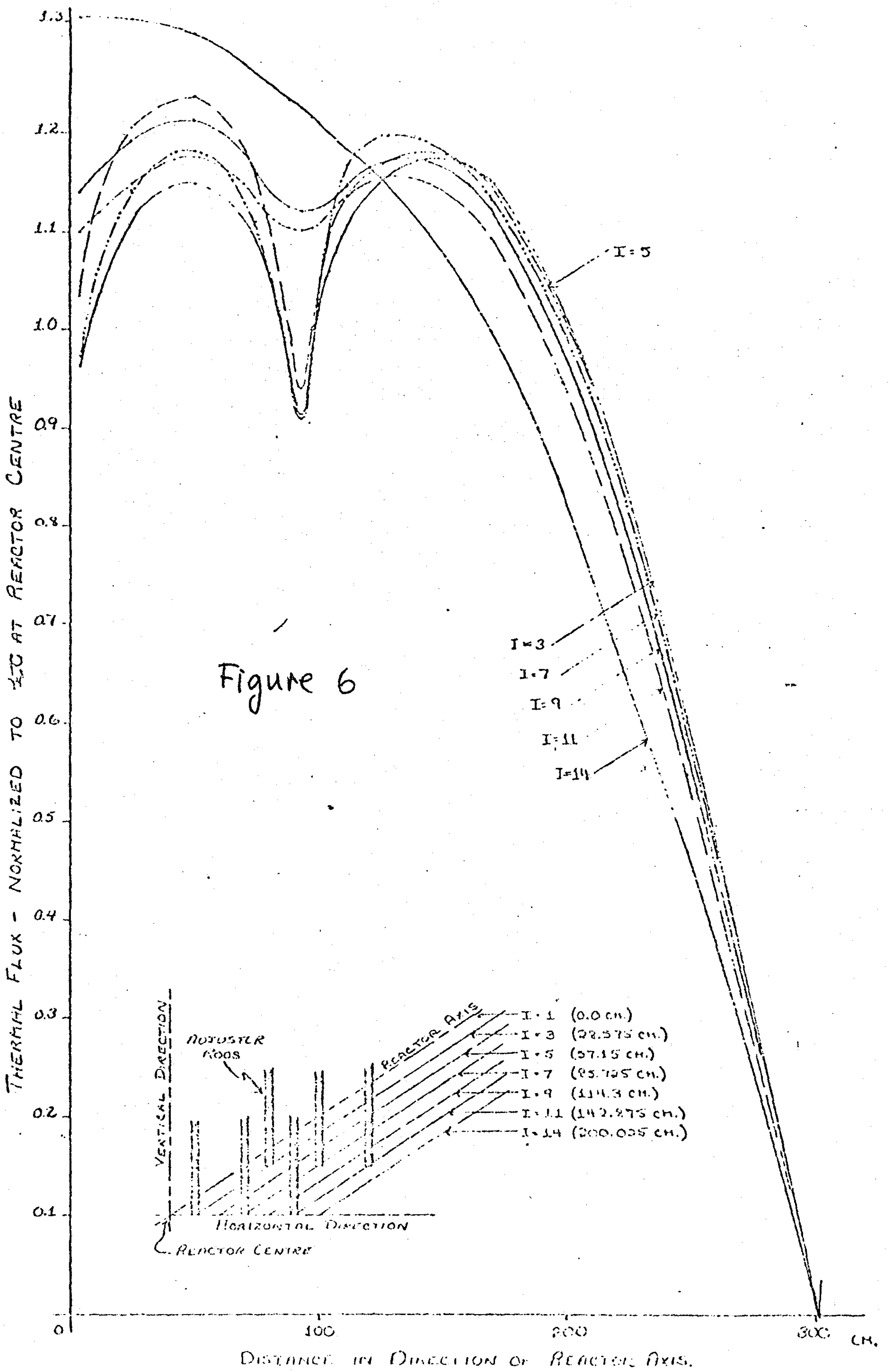

Figure 6

FIGURE ~~8.2.2~~ 6 NORMALIZED THERMAL FLUX DISTRIBUTION IN AXIAL DIRECTION

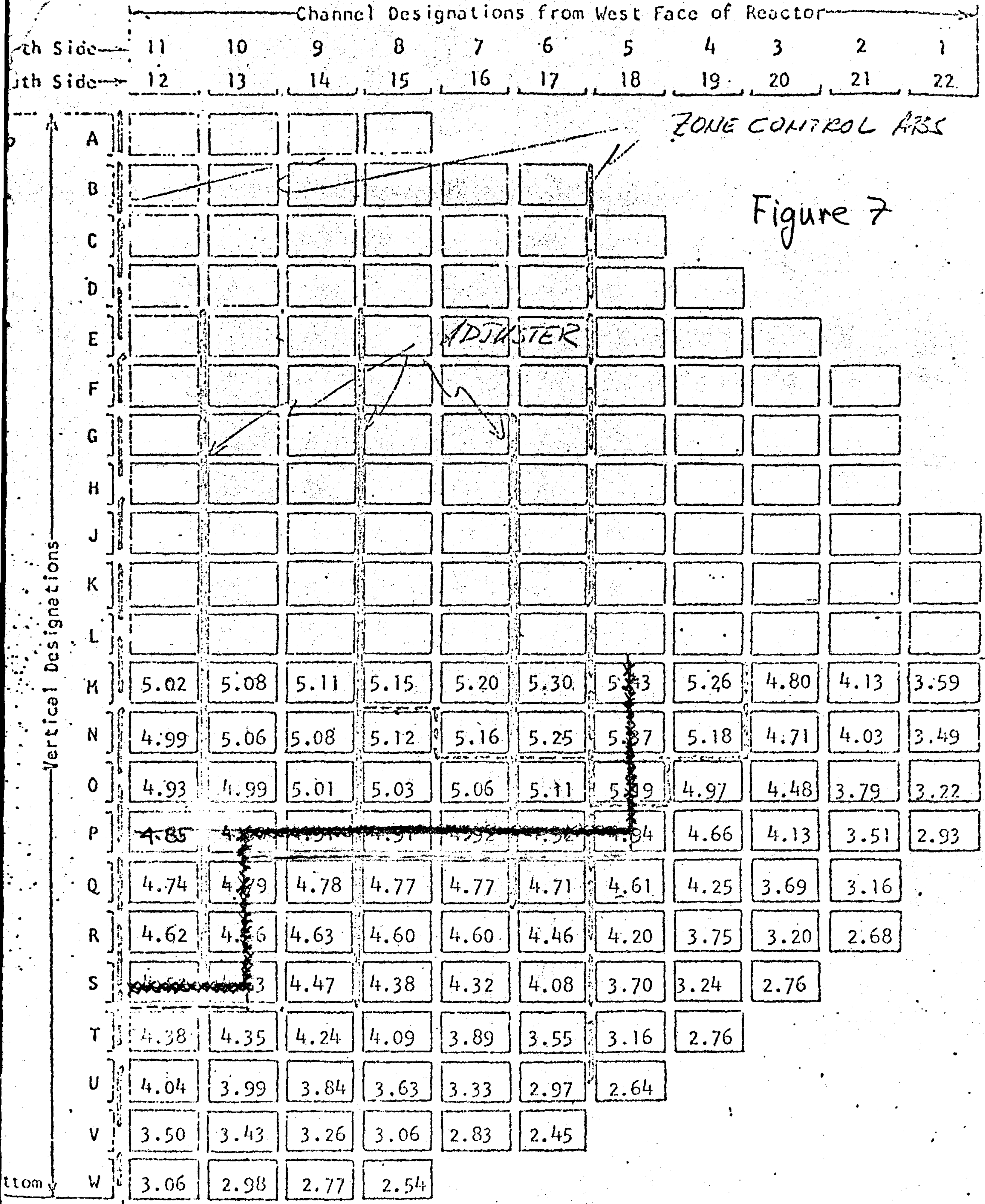

Channel Designations from West Face of Reactor th Side → th Side →	11 12	10 13	9 14	8 15	7 16	6 17	5 18	4 19	3 20	2 21	1 22
A											
B											
C											
D											
E											
F											
G											
H											
J											
K											
L											
M	5.02	5.08	5.11	5.15	5.20	5.30	5.43	5.26	4.80	4.13	3.59
N	4.99	5.06	5.08	5.12	5.16	5.25	5.37	5.18	4.71	4.03	3.49
O	4.93	4.99	5.01	5.03	5.06	5.11	5.39	4.97	4.48	3.79	3.22
P	4.85	[illegible]	4.91	4.91	4.92	4.92	4.94	4.66	4.13	3.51	2.93
Q	4.74	4.79	4.78	4.77	4.77	4.71	4.61	4.25	3.69	3.16	
R	4.62	4.66	4.63	4.60	4.60	4.46	4.20	3.75	3.20	2.68	
S	[illegible]	[illegible]	4.47	4.38	4.32	4.08	3.70	3.24	2.76		
T	4.38	4.35	4.24	4.09	3.89	3.55	3.16	2.76			
U	4.04	3.99	3.84	3.63	3.33	2.97	2.64				
V	3.50	3.43	3.26	3.06	2.83	2.45					
W	3.06	2.98	2.77	2.54							

FIGURE 7: Channel Power Distribution - MW(th) - in Nominal Operating Conditions

~~3-4-2~~

(Total Channel Power - 1655 MW(th))

7EA-2

8.3—6 EQUILIBRIUM XENON REACTIVITY LOAD VERSUS POWER LEVEL, AND MAXIMUM TRANSIENT XENON REACTIVITY LOAD ASSOCIATED WITH SHUT-DOWN FROM VARIOUS POWER LEVELS (EQUILIBRIUM FUEL CONDITIONS)

Figure 8

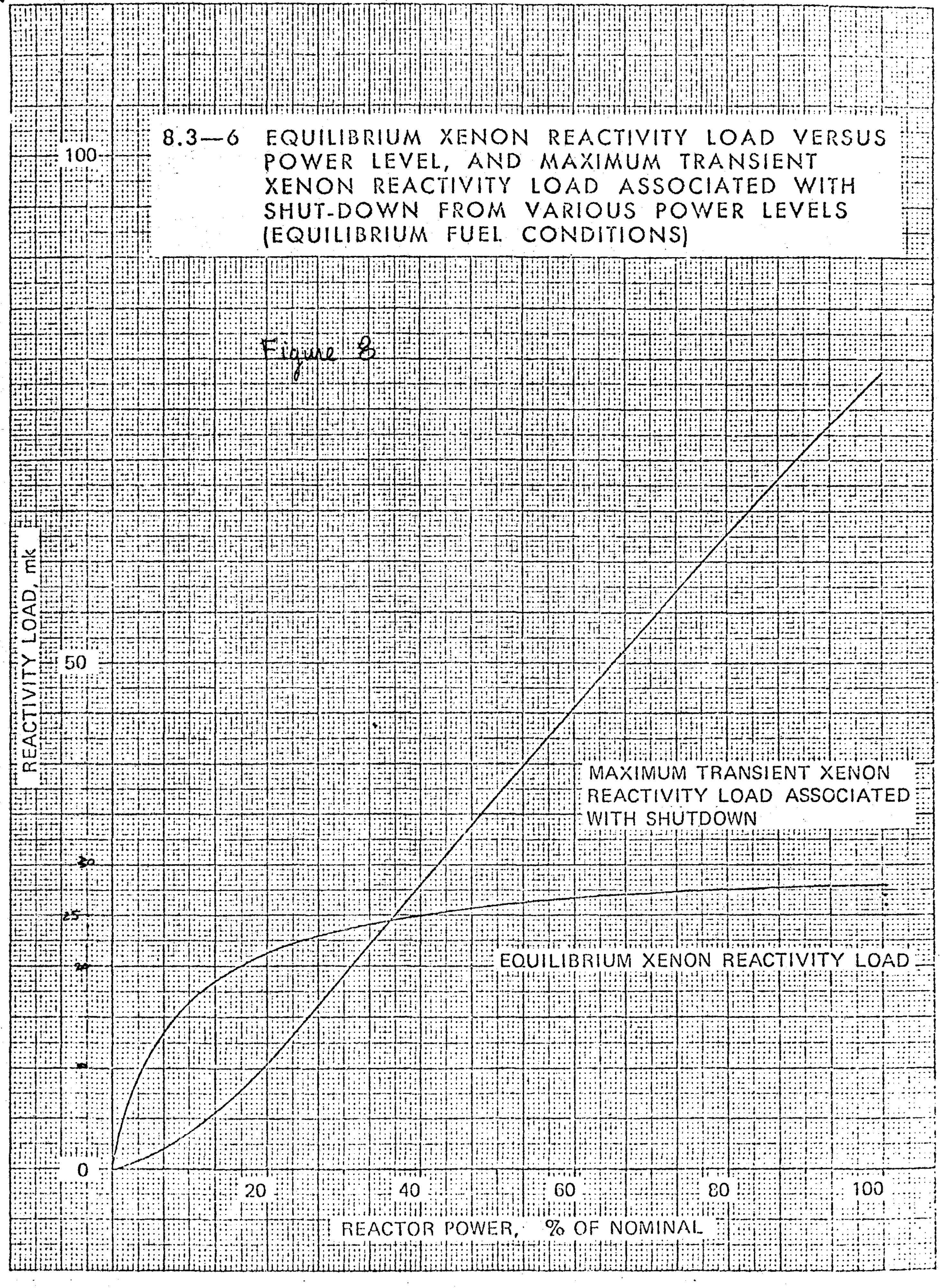

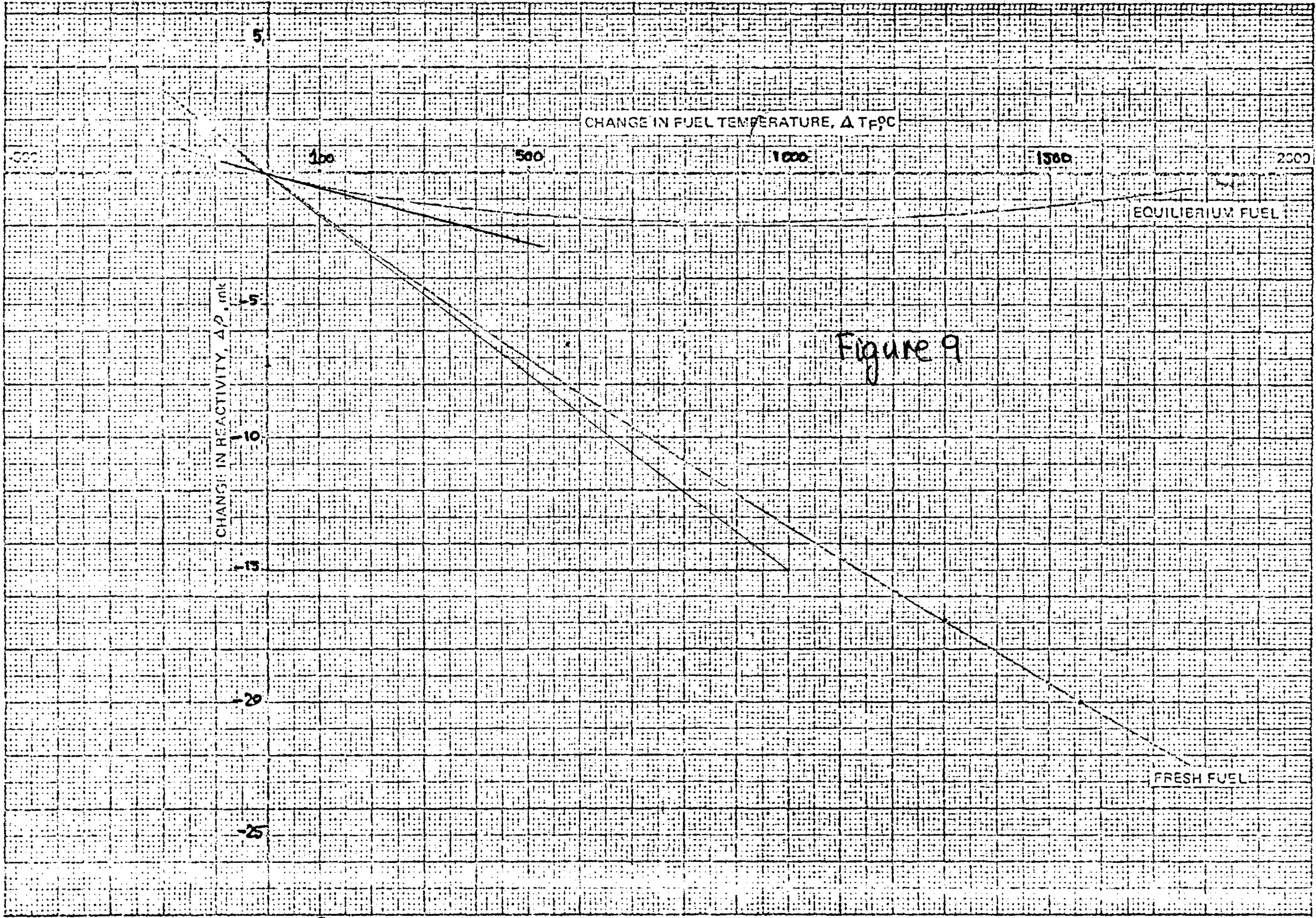

FIGURE -9 10.5-1 CHANGE IN REACTIVITY VERSUS CHANGE IN FUEL TEMPERATURE
(NORMALIZED TO NORMAL OPERATING CONDITIONS)

ARC TRIMMING OF NICHROME
THIN FILM MICROCIRCUITS

by

J.V.B. Simmons

PART B: McMASTER (ON-CAMPUS)
PROJECT

A project report submitted in partial fulfillment of the
requirements for the degree of
Master of Engineering

Dept. of Engineering Physics
McMaster University
Hamilton, Ontario
1971

* One of two project reports. The other part is designated PART A: INDUSTRIAL PROJECT.

TITLE (PART B): Arc Trimming of Nichrome Thin Film Microcircuits

AUTHOR: J.V.B. Simmons, B.Ap.Sc. (Univ. of Toronto)

SUPERVISOR: Professor J. Shewchun

NUMBER OF PAGES: i, 76

MASTER OF ENGINEERING (Engineering Physics)	McMASTER UNIVERSITY Hamilton, Ontario

ABSTRACT

Trimming of thin-film resistor components by an electrical arc is investigated in this report as an inexpensive and simple alternative to the laser trim and mechanical scribe methods. A multitude of tests were effected on Garrett Manufacturing Limited production circuits containing nichrome thin film resistors. These tests included Temperature Coefficient of Resistivity, resistance stability, substrate damage, noise performance, dynamic trim with active devices operating, width of cut as compared to mechanical scribe and laser trim techniques, and optimum parameters for trimming. In all cases the trimmed circuits were within the design specifications of the resistor properties under test. It is the conclusion of the author that the obvious attributes of the arc-trim method as well as its outstanding performance in the above tests, warrants its serious consideration as a viable alternative to the laser trim and mechanical scribe methods of altering resistance levels.

ACKNOWLEDGEMENTS

The author is grateful for the assistance of Bob Anderson and Robert Yager in the many experiments described in this report. In particular, the interest and insight shown by Mr. R. Yager was a major facotr in seeing this project to its successful conclusion. The author is also indebted to Dr. J. Shewchun for his direction and helpful suggestions. The many discussions held at Garrett Mfg. Ltd. always provided a source of ideas in the course of the experimental work and the author is thankful to the staff present at these encounters. Finally the report was funded by Garrett Mfg. Ltd. - Research Report No. 5304-5.

Table of Contents

1.0 INTRODUCTION

A thin film circuit begins with a passive (insulating) substrate made of glass or ceramic. Upon this insulating substrate, the passive components of the eventual circuit are deposited and interconnected. These depositions can employ a large number of metallic or metal-dielectric materials (called cermets), with a wide variety of electrical characteristics. The electrical characteristics of the thin-film components are determined primarily by the material employed for the film and by the geometry of the component pattern.

The material, in turn, stipulates the fabrication process to be employed. The two thin-film materials investigated in this report are nichrome and tantalum, the former deposited on the substrate by vacuum evaporation whereas the latter material is deposited by cathode sputtering. The tantalum received only a cursory examination, the main investigation being confined to nichrome.

Thin-film resistive elements are dependent upon the resistivity of the material, the thickness of the deposition, and the length-to-width ratio for their electrical properties.

Materials with different resistivities may be selected to fit the dimensional requirements of the substrate. Nichrome displays resistivities in the 50 - 400 ohms/sq. range with a temperature coefficient of resistivity in the range ± 25 - 100 parts per million per degree Centigrade. It adheres well to the substrate. Tantalum, on the other hand has a 50 - 500 ohms/sq. resistivity range with a T.C.R. of ± 100 - 200. The metal displays excellent process control, good adhesion, as well as being highly stable.

Practical film thicknesses range from approximately 100 to 1000 angstroms (Å). Films thinner than 100 Å generally are impractical because they tend to become very non-uniform (due primarily to discontinuities).

A serious limitation of thin-film resistors is the uncertainty in the final value of resistance of the deposited metal. The inherent statistical nature of the effect can be attributed to substrate undulations as well as impurities entering the resistor material during deposition. The range of resistance uncertainty can be minimized by effective process control, however this characteristic is present no matter what deposition process is employed.

It is apparent that a method of adjusting the resistance value after deposition would enable more highly sophisticated thin film networks to be produced as well as lessen the number of circuits rejected because a resistance value fell outside an acceptable tolerance band. An attractive method considered by virtue of its relatively small capital investment, was the removal of resistor material by an electrical spark or arc confined to a very small portion of the resistor. The intention being that by successively arcing away minute quantities of resistor material, the resistance could be increased by any desired amount. No readily apparent upper limit to the magnitude of the trim was found to exist. Even excessively large (100%) trims did not seriously alter such resistor characteristics as temperature coefficient of resistance, temperature stability and noise. The lower limit would seem to be a function of the skill of the operator at removing very small amounts of resistor material as well as the capabilities of the resistance measuring devices at detecting small enough resistance changes. To detect one part in 10^6 or 10^7 resistance change represents a formidable instrumentation problem.

In this report, the experimental method for trimming thin film microcircuit resistors by the electric or arc method will be described. To determine the effectiveness of the trim in terms of total circuit performance, tests were conducted on Temperature Coefficient of Resistance, resistance stability, substrate damage, noise performance, dynamic trim with active devices operating, width of cut as compared to mechanical scribe and laser trim techniques and optimum parameters for trim. These will be described in some detail.

2.0 TRIM APPARATUS

The apparatus for trimming thin film resistors is basically simple, consisting of a pulse generator capable of supplying a kilovolt range adjustable pulse to a sharply pointed tungsten stylus which is either in contact with or slightly above the thin film surface that is to be cut. The motion of the stylus relative to the film surface can be accomplished either by moving the stylus or the film. For the study reported here the tungsten stylus was moved although in practical production application situations the movement of the film substrate is obviously preferable. In this case a loaded tungsten stylus in a configuration similar to the needle in a record player arm would be used.

The probe is made of tungsten which is a very strong metal possessing a melting point higher than most metals. These two properties are quite useful for the arc-trim method, since the probe is subjected to a localized, intensely hot spark which might cause other metals to vaporize or sputter. The probe is electrically etched in a solution of potassium hydroxide to a sharp point, necessary in part for very fine trims of the order of two tenths of one thousandth of an inch. The fact that the metal is quite strong insures a long life for the probe and minimizes the inconveniences of having to replace it after a short period of operation. The resistors array is viewed through a microscope which displays the surface at a magnification of 30 times the actual size. The probe is mounted on a micro-positioner which facilitates three dimensional movement to any resistor on the device under trim.

The description of the apparatus in this section will be presented in terms of a setup for trimming two specific nichrome thin-film resistor circuits: a twelve bit analog to digital ladder (GH 1039) and a sensor bridge resistor network (GH 1025). A simplified schematic of the experimental setup employed is shown in figure 1. With the high voltages employed in arc-trimming, there existed the possibility of damaging the ohmmeter used in sensing resistance values. Therefore, by way of a relay, the arc and read functions were separated physically from each other.

The pulse generator is typically set for a 10 kHz. pulse repetition rate, each pulse being 5 μsec in width and the voltage adjusted for optimal cutting. Before being applied to the tungsten probe, the voltage pulse train is passed through a 30:1 step-up transformer so that the actual arcing takes place at a voltage in the kilovolt range. The voltage train is gated from a voltage signal supplied to the generator by a push button switch.

Any two of the thirteen operational pins on the GH 1039 device can be selected by two thirteen position switches (see figure 2 for the

GH 1039 schematic). When the read function of the relay is initiated, the selected pins are switched to the digital ohmmeter.

Sometimes as in the case of the GH 1025 device, it is necessary to know only the ratio of two resistors. In this case, with the ohmmeter in "ohms ratio" function, the common arm of each of the two resistors is grounded, and the free ends connected to the ratio inputs of the ohmmeter via the selector switches and the relay. The common terminal of the ohmmeter is also grounded.

3.0 TRIM TECHNIQUE AND OPTIMUM PARAMETERS FOR RELATIVELY EASY TRIMMING

The actual cutting procedure is relatively easy and a trim can be affected in a very short period of time. The probe is lowered until it rests lightly on the surface of the substrate in close proximity to the resistor to be trimmed. The voltage is then applied to the probe, resistor material being vaporized away as the probe is moved along the surface of the resistor by means of the x-y movement of the micropositioner.

The vaporizing of the resistor material occurs very quickly which is desirable since a high rate of slue of the tungsten stylus would be required for production line operation. In addition, the cutting process is self-quenching. If the tungsten probe is held on the resistor material and not moved, a hole is burned out quickly after which the arcing ceases. The quenching occurs presumably when the air gap is large enough to support the voltage without a breakdown. The magnitude of the voltage pulse determines to some extent the width of the hole and hence the width of the cut.

Occasionally it was found that substrate surface undulations would prevent a good cut from being maintained over the length of the resistor. This occurred since the probe was moved, at a constant height, relative to the substrate holder table. Although this was not really a problem in the trimming done to date, in actual production it would be undesirable and could be overcome by using a loaded stylus and moving the substrate relative to it.

An optimum cut is a trim into the body of a resistor such that the cut is clean, well-defined, and as fine as possible after the resistor material has been vaporized away. A high rate of slue should also be maintained while cutting continuously into the body of the resistor.

The effect of variations in the three pulse-generator variables on the ability to make an optimum cut (maintaining a high rate of slue) was investigated. The three parameters were the number of pulses per second (I.R.R.), the width of each pulse (P.W.), and the amplitude of the pulse (P.A.).

Initially, the three parameters were set to the nominal values used throughout the experimental work since these settings, determined by trial and error, provided an optimum cut on the GH1039 nichrome thin-film resistors [I.R.R.=10kHz, P.W.(tungsten probe)=5μsec., P.A.(tungsten probe)=1500 volts]. Maintaining the latter two parameters constant, the repetition rate was varied. A 10% adjustment in the rate resulted in the width of the cut increasing markedly. In general, the pulse repetition rate was found to be the most sensitive parameter in the trim process.

Next, the I.R.R. and P.A. were kept at their optimum values and the pulse width varied from the 5μsec. mean position. It was found that an optimum cut could be made over the range 4μsec.-6μsec., above which the width of the cut increased considerably. Lower than 4μsec. pulse widths resulted in regions of the cut where resistor material remained behind. In order to make a satisfactory cut at small pulse widths, the stylus had to be moved back and forth several times over the length of the cut.

When the I.R.R. and P.W. were held constant and the pulse amplitude varied, it was found that pulse amplitude was the least sensitive parameter in adjusting for an optimum cut.

When initiating a trim for the first time on a specific device it is not obvious which pulse generator settings will result in an optimum trim. The process of obtaining these values is initially one of trial and error. However, from the results of the investigations conducted, this process can be greatly speeded up. Since the repetition rate was found to be the most sensitive parameter, it is generally wise to fix its value to some reasonable rate such as 10kHz. Similarly the pulse width can be set to some reasonable value such as 5μsec. Since the voltage of the pulse provided the largest range of adjustment over which an optimum cut could be maintained, it is obvious that this parameter should be varied first in the initial set-up. If the width of the cut is too large or improper at all voltage settings, the pulse width should be decreased, say twenty percent, and the pulse voltage varied over its entire range as before. Similarly if there is no vapourization of resistor material at any of the voltage settings, the pulse width should be increased, say twenty percent, and the voltage search initiated again. This systematic approach should provide the settings for an optimum trim with the least amount of effort.

It has been found that for different pulse repetition rates there is usually a small range of pulse widths and large range of pulse amplitudes over which acceptable trims can be obtained.

In the course of the experimental work it was found that once instrument parameters for an optimum cut were determined for a particular resistor on any given circuit such as GH1039, these parameters were true for all other resistors of the circuit and thus the voltage did not have to be changed for each new resistor to be trimmed. This represented a considerable saving in time. The optimum voltage was, however, found to be slightly different for the GH1025 circuit. Fortunately, the repetition rate and pulse width did not have to be changed. Similarly with the tantalum thin film resistors, a unique voltage level, common to all the resistors on the device, existed.

4.0 THIN FILM CIRCUITS EMPLOYED IN TRIMMING

Three thin film circuits supplied by Garrett Manufacturing were employed in the experimental studies: a twelve bit analog to digital ladder, (GH 1039); a sensor bridge resistor network,(GH 1025); and a servo loop signal conditioner (GH 1042).

The GH 1039 was used to test the feasibility of direct absolute trims to a specified resistance value. Included was an investigation of the ease with which each particular resistor could be brought into specification and the effect of arc trimming on the physical characteristics of the resistor.

The GH 1025 is a circuit in which the ratios of two resistors are specified to within certain tolerance levels. GH 1025 was used primarily to gain experience with the trim technique and determine its versatility once the major features had been established on GH 1039.

Trimming of the servo loop signal conditioner was carried out since it was felt desirable to find out whether arc-trimming could be carried out on circuits consisting of thin-film resistors and active devices, such as operational amplifiers, in close proximity to one another, with no harmful effects on the operating characteristics of the active devices.

4.1 TWELVE BIT ANALOG TO DIGITAL LADDER (GH1039)

Figure 3 shows the actual surface of the GH 1039 resistor array while, as mentioned previously, figure 2 presents a simplified schematic version. The R and 2R resistors labeled on the schematic are displayed in part in figure 4. Figure 3 consists of R-2R blocks as shown in figure 4. It is evident from figure 3 that there is additional resistor material which is not shown in figure 4. This appears as thin lines which run from each of the three bonding pads opposite the pin number into the region above the dark horizontal conductor which appears along the length of the R-2R bit. In practice, a gold wire is bonded from a pin to one of these three pads. It is evident from figure 3 that different resistance values will be obtained depending on which pad is bonded to since varying lengths of resistor material are by-passed. Similarly, in figure 4 there are lines missing which represent resistor material associated with the R resistor. These missing lines actually incorporate most of the resistance associated with the R and 2R resistors. The white regions in figure 4 represent resistors while the black portions depict conductor material. The trim is generally restricted to the resistors shown in figure 4, although the main resistors connected to the pads can be trimmed. This is not the intended procedural method however.

Specifications call for the bonded values of the R resistors to be in the range to 16,000 to 22,000 Ω while the bonded values of the

2R resistors must lie between 36,000 Ω and 44,000 Ω. The 2R resistors can be brought into this range by selecting one of the three appropriate bonding pads. Referring to figures 3 and 4, bonding to the middle pad adds 4000 Ω while bonding to the pad on the bottom (figure 4) subtracts 4000 ohms. The pad on the top (marked A) is bonded to if the resistor is in its nominal range. The R resistors can be brought up in value 2000 Ω by bonding to the pad preceeding the one marked A. Normally this section is bonded out and the short removed if an increase of 2000 Ω is required. (Thus a coarse trim of ± 10% on the 2R resistors and - 10% on the R resistors can be affected by simple wire bonding.) The appropriate pads of each R-2R combination are bonded to their related pins.

Referring again to figure 3, initially all the nodes between the R-2R resistors (marked J) are bonded to the common line which connects to pin 20. The common line runs down the centre of figure 3. All the R resistors are therefore shorted out. These shorts are removed in the process of trim as will be discussed in a subsequent paragraph.

The fine trim on the 2R resistors consists of cutting out the appropriate "spread-trim" loop. This section, represented by figure 4, consists of a series string of resistors each with a shorting section which can be cut or opened. The short is actually a resistor in parallel with the main adjustment resistor. The trim range is .01% to 5% of nominal in 10 binary steps, each step increasing the resistance value.

The fine trim on the R resistors is the same except that it covers the range .01% to 10% in 11 binary steps. (Refer to figure 4). The purpose behind these geometrically intricate spread trim loops is that in a digital to analog ladder the values of each of the 2R resistors should be identical to within the binary quantization error* of the binary word length associated with the most significant bit. In the GH 1039, there are twelve bits (n = 12) and the binary quantization error is .01%. The 2R resistors should be identical to within ±.01%. This necessitates a measuring device capable of measuring resistance to at least half an order more of accuracy, that is,one that measures five figures with an accuracy of .005%.

The ohmmeter employed in thisstudy, although possessing a resolving capacity of .001% (1 ohm in 100,000 ohms), was guaranteed to have a long term accuracy of .01%. However, the 24 hour accuracy was .005%. Therefore, no problem was encountered on the devices under study since they could be trimmed in very short period of time within which it could safely be assumed the relative error would not change. Thus, even if the resistance values displayed were slightly in error, they would be incorrect by the same amount for all resistors that were trimmed and so relative to one another, the resistance levels would be within specification.

* $\pm \left\{ 1/2 \left(\frac{1}{2^n - 1} \right) \times 100 \right\}$

In the actual trim process, the highest 2R resistor is noted and all other 2R resistors are trimmed to this value. According to the specification, 2R resistors numbered 10, 11, 12 and 13 are trimmed to the reference value minus five ohms (RSI). After this has been completed, the R resistors are trimmed to one-half of the associated 2R resistor (refer to figure 2). To get at the first R resistor, the first bond to the common line is broken. The value that is measured is obviously the sum of 2R and R. Since 2R is known the difference between R and nominal can be deduced. The trimming is carried out by arcing out the appropriate spread-trim loop until the R resistor is trimmed. This process is repeated in sequence until all R resistors have been trimmed.

The trim method which had been used prior to the arc trim was to cut the appropriate spread-trim loop mechanically with a diamond stylus. The resistor material was not actually removed but rather "snow plowed" out of the way of the diamond stylus. The intense pressure to which the substrate is locally subjected to by this cutting method is not desirable since any stressing of substrate material can result in the propagation of a crack along such a path. Also it was found in practice even after cutting out the spread-trim loops, that a 2R or R resistor could still be out of specification. This could be corrected easily with the arc trim method by cutting into the body of the resistor associated with the .01% trim loop or some other trim loop of low percent change.

The experimental work substantiated the initial belief that the arc-trim method could quickly bring the GH 1039 to the specifications as laid down in Garrett Specification "Section 3 - Trim Procedure R-2R Ladders", (See "GH 1039 - General" for details), by arcing out the appropriate "Spread-Trim loop". In addition, if a further fine trim was required to bring a particular resistor to the reference value, a trim could easily be executed in the main body of the resistor associated with the .01% spread-trim pad. Coarser adjustments could be carried out by cutting into the main body of the resistor associated with the .02%, .04%, etc., spread-trim loops. Some typical cuts and the associated resistance changes are displayed in photographs 1 through 6, and summarized in table 1. Orientation can be achieved by referring to figure 4 and noting that in photograph 1, the grey material with the vertical black line through it is resistor. The black rectangle is substrate material, while the conductor appears as grey with tiny black "pox" marks.

It should be evident that the black horizontal lines in the resistor which represent the cut actually represent the ceramic substrate showing through after the resistor material has been vaporized away by arcing. It is also obvious from photograph 1 that the .01% spread-trim loop shorting resistor has been cut and the trim resistor associated with this loop has been arced into approximately half the total length of the resistor. The initial and final values of the resistance were 40,010Ω and 40,025Ω respectively, a net increase of 15 ohms. In photograph 2, the resistor associated with the .01% spread-trim loop has again been cut into, this time only about two-thirds as far as the cut in photograph 1. The resistance change from Table 1 is shown to be only two ohms. It should be clear that a smaller increase in resistance can be achieved by cutting into the resistor a shorter distance. Photographs 3 and 4 show cuts into the body of the resistor associated with the .02% spread-time loop. In photograph 3, a cut about half the length of the resistor represented an increase in resistance of 25 ohms, while in photograph 4, a shorter cut increased the resistance 5 ohms. Further experimentation showed that by cutting into the resistors associated with the .04%, .08%, .16% and .32% or higher spread-trim loops respectively, the resistance could be altered by an increasingly large amount. In the majority of cases, it wasn't necessary to cut into the body of any resistor associated with the .32% or higher spread-trim loops, since most 2R or R resistors were not that far below reference value. As an experiment, however, the value of a 2R resistor was increases by 3000 Ω by cutting into the resistors associated with the higher percentage change spread-trim loops.

Photograph 5 displays three successive rectangular cuts into the resistor associated with the .02% spread-trim loop. The first cut actually lowered the resistance one ohm, whereas the next cut raised the resistance four ohms and the final cut increased it another five ohms.

Exactly the same technique was used in photograph 6 except that it was carried out on the .01% resistor. The first cut lowered the resistance four ohms while the next cut increased it three ohms and the last cut raised the resistance another two ohms. Comparing the final cut in photograph 6 with the one in photograph 2, the resistance changes are about equal even though much more resistor material has been removed by the cut in figure 6. It is concluded from this effect that it is the depth of the cut into the body of the resistor that makes the significant change in resistance rather than the amount of resistor material removed. The origin of the initial drop in resistance is not understood at this time.

4.2 SENSOR BRIDGE RESISTOR NETWORK (GH 1025)

The schematic of the GH 1025, a sensor bridge resistor network, is shown in figure 5. Specifications call for only R_2 and $R_1 + R_2$ to have absolute resistance values of 496.0 Ω ± 4 Ω and 933.8 Ω ± 0.40 Ω, respectively. The other resistors are specified only in that the following ratios must exist:

$$\frac{R_4}{R3 + R_4} = .3850 \pm .0029$$

$$\frac{R_6}{R5 + R_6} = .7910 \pm .0055$$

$$\frac{R_8}{R_7 + R_8} = .5000 \pm .0002$$

Figure 6 shows a pictorial layout of the thin film circuit. Resistors R_1 and R_2 each have two trim tab resistors associated with them as marked. The absolute values of R_1 and R_2 are adjusted by trimming into the body of these trim tab resistors. The main resistor chain is not normally trimmed. For the ratio specification, such as that associated with R_7 and R_8, a trim is made into the main body of the resistor as shown in figure 6.

Of the GH 1025 circuits supplied by Garrett, all had the absolute resistance value of R_2 and $R_1 + R_2$ greater than those as laid down in the specifications. Therefore, the absolute resistance values in the specifications could not be achieved. However, it is evident that the most stringent absolute resistance specification is that R_1+R_2 have the value of 933.8Ω ± .40Ω. Hence, if these resistors could be trimmed in steps smaller than 0.4Ω, it seemed reasonable to assume that the original absolute specifications could be met on good units with values in the tolerance band. By electrically arcing into the body of either R_1 or R_2, it was found that the ±.40Ω specification could easily be achieved.

The ratio specifications were tackled next. With the ohmmeter in the ratio mode described in the section 2.0, a trim was initiated into the main body of, for example, either R_3 or R_4, depending on whether the ratio needed adjusting downwards or upwards respectively. It was found that all three ratio specification requirements could easily be met, the most stringent being the $\dfrac{R_8}{R_7 + 7_8}$ requirement of 0.500 ± .0002.

Some typical values achieved on a ratio trim are as follows:

$$\frac{R_4}{R_3 + R_4} = .3845$$

$$\frac{R_6}{R_5 + R_6} = .7913$$

$$\frac{R_8}{R_7 + R_8} = .4999$$

As in the case of the GH 1039, these ratios, when remeasured at various times up to 48 hours after the trim (always at the same temperature), remained at their trimmed values.

4.3 SERVO LOOP SIGNAL CONDITIONER (GH 1042)

A schematic diagram of the Servo Loop Signal Conditioner is shown in figure 7. The Servo Loop Signal Conditioner is a hybrid circuit containing thin and thick film resistors, 709 and 741 operational amplifiers, discrete diode and discrete transistor chips. Six thin film resistors are connected to the inverting input of a 709 operational amplifier $^{(Z1)}$, each with one end brought out to separate pins on a 20 pin package. The six thin film resistors, $R1_A$ to $R1_F$, are normally trimmed to specific resistance values and resistance ratios.

The objective in trimming this device was to investigate the possibility of damaging active devices in close proximity to resistors being arc trimmed. The input resistors association with the 709 operational amplifier (Z1) were selected for the test. No attempt was made to trim the input resistors to specific values, instead gross trims were made. The investigation was confined to the circuitry associated with the 709 operation amplifier (Z1) and the remaining circuitry was ignored. The trim procedure will be described in section 9.0.

5.0 TEMPERATURE COEFFICIENT OF RESISTANCE

Tests were conducted to determine the effect of the arc trim method on the Temperature Coefficient of Resistance (TCR). These tests were prompted by the concern that the resistor material in the localized region around the cut had been subjected to an intense temperature fluctuation in the vaporization process of the cutting and that possible changes in the chemical and physical properties of the film along with exposure of resistor material to the ambient might seriously affect the TCR. Normally, the TCR is in the 0 - 100 parts per million per °C range.

The tests were conducted on the GH 1039 and GH 1025 circuits. Two major types of tests were conducted. In the first, experiments were carried out on the GH 1039 to determine if arc trimming into the spread trim loop resistors with the shorting resistors opened caused any change in TCR. Trimming of the spread trim loop resistors results in small resistance changes (a few percent at most) compared to the main chain resistors (R or 2R). Furthermore, it was assumed and indeed verified through the experiments, that opening the shorting resistors by arc trimming did not alter TCR. This would be expected since no current flow occurs in this region once the path is broken. On the other hand, a trim into the spread trim loop resistor means that current will flow adjacent to a region of trim which might affect TCR. In the second major trim test, the effect of a gross trim 100% into the body of a main resistor was checked out on the GH 1025 circuit.

The experimental setup consisted of a temperature controlled enclosure, a Delta Design MK2300 model. The resistor was placed inside and the door sealed. The small conduction losses through the lead in wires attached to the resistors under test were ignored and the temperature of the sensing device in the oven was assumed to be the temperature of the resistors. The temperature was decreased to -50°C by introducing dry ice into the enclosure. After waiting a sufficiently longer period of time such that the resistor had come into equilibrium with the surroundings, the resistance, monitored continuously on a digital ohmmeter, was noted. The temperature was then increased in 20°C increments to 70°C by means of an internal heater in the temperature chamber. The resistance was noted at each temperature level after equilibrium had been established. Since the T.C.R. appeared to be linear with temperature, the T.C.R. of a given resistor was taken as the arithmetic means of the six TCR's. calculated over the six 20°C temperature intervals.

The first major test was conducted with the GH 1039 in which some of the spread trim loops were adjusted and others were left untouched so as to serve as a reference. Trims were performed only on the 2R resistors since these were the only ones which were readily accessible for measurement of direct absolute resistance. The results of the test, summarized in Table 2, show that the TCR's of the trimmed and untrimmed resistors were found to be essentially the same (approximately 30 parts per million per °C). The trims were carried out on the .01% spread trim loops. The lack of change in TCR was anticipated since the spread trim loop resistors, which are in series with the main body resistors, are only a small fraction in value of the main body resistors (approximately .01% of the 42,000Ω main resistor). Any change in TCR of the spread trim loop resistors would be masked by the large resistance ratio. Although this test proved that a circuit designed for trimming in a specific way (such as GH 1039) would not experience a TCR degradation by the arc trim method, it did not really establish the bulk TCR properties of the nichrome film and its ability to resist TCR change in the trim process. For this purpose a TCR check should be carried out on a resistor with a trim into the main body (rather than into a trim tab or spread loop resistor) such that a gross change in resistance, say 100%, is effected. The main body 2R resistors on the GH1039 are unsuitable for such a test since their value would have to be increased into the 80,000Ω vicinity (from approximately 40,000Ω) and the length to width ratio is so high that this would be an extremely difficult trim into the body. Such a test was, however, performed on the GH1025 where the geometry was more suitable.

Two tests were conducted on the GH1025 Sensor Bridge Resistor Network Circuit. In the first, a 10% trim was carried out into the body of typical resistors and in the second, the major trim test, a 100% trim was carried out.

Table 3 lists the results of tests on the GH1025 in which the R_6 resistor was increased in value by 10% by cutting into the main body of the resistor. R_8 was an untrimmed resistor used for reference. The uncut resistor had a T.C.R. of 63.5 p.p.m. per °C, whereas the trimmed resistor actually had a slightly lower T.C.R. of 61 p.p.m. per °C. This 4% difference in T.C.R. is well within the statistical deviation of the T.C.R. of the uncut resistor, shown in the third column of table 3.

In the major trim test, a 100% increase in resistance was made and the circuit was checked carefully for T.C.R. change. As mentioned earlier, this was considered to be the most significant test in terms of revealing whether the arc-trim process caused any degradation of T.C.R.

Table 4 lists the results of this particular test. R_1 of GH1025 was trimmed for a 100% increase in resistance by cutting into the two trim pads provided as well as into the main resistor chain. R_2 was untrimmed and used as a reference. The temperature was increased in 20°C intervals from -70°C to 90°C. The T.C.R. of the untrimmed resistor was found to be 80 p.p.m./°C ± 10 p.p.m./°C, the magnitude of the statistical error being derived from the deviations in the nine T.C.R.'s determined at each 20°C interval.

The T.C.R. of the trimmed resistor was found to be 88 p.p.m./°C ± 10 p.p.m./°C. Although the possibility of a slight T.C.R. increase after trim is evidenced from these results, the increase is well within the statistical deviation.

The conclusion reached from the T.C.R. tests was that the arc-trim procedure does not noticeably change the T.C.R. of the original material. Differences in T.C.R. between the tested substrates of a circuit such as GH1025 indicate that the T.C.R. itself is probably not that well controlled. Indeed, the GH1039 substrate had a low of 30 p.p.m./°C, whereas the substrate used to generate the results in Table 4 has a T.C.R. of 80 p.p.m./°C.

6.0 RESISTANCE STABILITY

Another important consideration associated with resistor trim techniques is that they not affect the stability of the resistor after trim. The stability specification for the Garrett nichrome film resistors is less than a 0.1% change in resistance per 1,000 hours at 150°C storage.

Since stability is usually an aging process and such processes can be accelerated with temperature change, it is usual to subject the resistors to a temperature cycling process. In the tests conducted, the resistors were placed in a Delta Design MK 2300 temperature controlled chamber and cycled twice from -65°C to +125°C and then brought back to room temperature. Dry ice was used to acheive the -65°C temperature. The resistors were measured with a digital ohmmeter before and after the temperature cycling.

Table 5 shows the results of the stability test carried out on the GH 1039. Thirteen 2R resistors were trimmed by trimming into the body of the spread trim loop resistors. No significant change in the trimmed resistors was observed as a result of the temperature cycling. The results are well within the specification of less than a 0.1% resistance change.

A similar test was performed on the GH 1035 in which the trimmed ratios $\frac{R_4}{R_3+R_4}$, $\frac{R_6}{R_5+R_6}$ and $\frac{R_8}{R_7+R_8}$ were measured before and after temperature cycling. No change was measured.

These tests proved in a very positive fashion that the arc trim procedure does not affect the resistance stability of nichrome thin film resistors.

7.0 NOISE PERFORMANCE

When trimming directly into the body of a resistor, obviously the current flow lines are redistributed within the resistor in the vicinity of the cut. Also there is a possibility that the temperature gradients established during arcing might change the physical characteristics of the resistor in the vicinity of the arc. Naturally, the possibility of altering the current noise through the thin-film resistors should, therefore, be investigated.

The method for determining current noise is described in MIL-STD-202D, Method 308. The method employed in this test has been designed to evaluate accurately the "noisiness" or "noise quality" of individual resistors in terms of a noise-quality index. The noise-quality index, expressed in decibels (dB), is a measure of the ratio of the root-mean-square value of current-noise voltage (in microvolts) to the applied dc voltage (in volts). The pass band associated with the noise-quality index is one frequency decade, geometrically centered at 1000 hertz.

Normally, measurements of current noise are carried out on a Quan-Tech Laboratories Model 315 Resistor Noise Test Set. Since a Quan-Tech was not available, the apparatus shown in Figure 7 was assembled consistent with the MIL specification. The apparatus and procedure are essentially the same as described in Method 308. It was necessary to decouple the voltage supply with R1, C1 to get a low background noise.

The 0.15 second time constant gives better than 50 dB. rejection above 500 hertz. The isolation resistor R2 was selected by using similar resistors for R2 and R3 until a low noise type was found. A 0.1% wire-wound type was found which introduced very little background noise.

The system was calibrated by opening the box, connecting the signal generator (to terminal B) and adjusting the gain of the amplifier to give a convenient +60 dB reference on the wave analyzer for 1 mV across R5. After the signal generator was disconnected the box was closed, the voltage supply was set to 0V, and the system or background noise was measured. The procedure for measuring the actual current noise involved the following: opening the box, setting the voltage supply to give 50V across the resistor under test by connecting a high impedance DVM between point A and ground, disconnecting the DVM, closing the box and recording the noise as indicated on the Wave Analyzer. The calculation of the noise index is described in Method 308.

The current noise of the thin film resistors was found to decrease with trimming, the greater the trim, the greater the noise decrease. A typical GH1039 2R resistor gave the following noise indices (for 50V across the resistor).

Resistance of 2R	Noise Index	Operation Performed
42.71K	-7.5 dB	Resistor untrimmed
46.41K	-9.0 dB	All spread-trim loops cut open
48.02K	-13.5 dB	Cut into spread trim resistor
50.10K	-17.5 dB	Further cut into spread trim resistor

A net decrease of 10 dB was noted for large trims. A small trim of a few percent produced, typically, a noise decrease of 1 dB.

As a check on the accuracy of the noise measurement apparatus, the noise of two fixed resistors was measured on passed on to Garrett to be checked on a Quan-Tech 315. The noise of a 100K carbon composition resistor at 200 volts was -4 dB or .63μV/V. A Welwyn 100K M12D resistor had a noise index of -32.2 dB or .025 μV/V.

As a follow up to the unexpected noise decrease in the thin film resistors, a crude anneal in the resistors was attempted to see if the noise properties could be changed. The noise of an untouched resistor was measured; the resistor was heated by passing current through it at two watts dissipation, and the noise remeasured. The following results were obtained:

Initial resistance	40.30K
Initial noise	-8 dB
Noise after 10 min. bake at two watts dissipation	-13 dB

Noise after further 11 min. bake	-15 dB
Noise after further 35 min. bake	-19 dB
Final resistance	40.78K

The above results suggest that thermal annealing can cause a decrease in noise. A possible argument is that the decrease in noise due to arc trimming is a result of such thermal annealing when resistor material is being removed by vapourization. However, the amount of area affected in the arc trim is relatively small and this seems inconsistent with the gross thermal anneal results presented above. Furthermore, in laser trim situations, results have been reported which show an increase in noise and similar thermal effects are present in that trim process as in the arc trim.

A further brief experiment was performed in an attempt to clarify the unexpected large noise decrease. It was postulated that the decrease in noise might be associated with processes occuring when the current from the application of the high voltage on the probe flows through the aluminum-nichrome interface (making up the bonding pad) and the body of the resistor material. The actual arc cut of the resistor might not influence the noise performance. In order to check the hypothesis, an arc trim was attempted on the aluminum pad of a typical resistor. Ground contact was made on an aluminum pad at one end of a 2R resistor and the cutting probe was brought close to the surface of the aluminum pad at the other end of the resistor. Current flow was, therefore, through the total body of an untrimmed resistor. There was no apparent cutting of the aluminum pad. There was also no change in the noise index of the resistor. This experiment would suggest that the aluminum-nichrome interfaces are not responsible for the decrease in noise and that the noise decrease is an intrinsic property of the arc cut into the nichrome resistor material.

8.0 SUBSTRATE DAMAGE AND A COMPARISON OF ARC, LASER AND MECHANICAL STYLUS CUTS

In any trim process where resistor material, which is usually attached firmly to the substrate, is removed, the question naturally arises as to whether the substrate sustains any damage. If there is damage it can appear as a degradation of the electrical characteristics of the film resistors or a more violent event such as fracture of the substrate itself. The arc trim method was examined to see if substrate damage was incurred and, in addition, a comparison of the process was made with the mechanical stylus and laser trim techniques.

The ideal trim technique should leave the substrate free from microscopic fissures or severe strain, either thermal or physical. Mechanical trimming exerts intense pressure on the substrate with the distinct possibility of the creation of faults such as cracks. In addition, the cuts are not likely to be clean and this may lead to undesirable electrical effects. Electrical arcing should subject the substrate to very little physical pressure and less thermal stress than say the laser beam technique. Photographic and chemical etching studies were carried out in an effort to substantiate some of these claims.

The mechanical scribing method using a diamond stylus was thought to damage the substrate severly while removing resistor material during a cut. Photographs, taken at high magnification, which compare a mechanical and an arc-trim cut show this to be indeed true. As well, they demonstrate that the arc-trim causes minimal substrate damage. In photograph 7, taken at a magnification of 25X, two resistors are shown, the widest cut on each of these resistors was produced by a mechanical scribe, while the other cuts represent resistor material that has been electrically arced away. What is visibly evident in this photograph is that the mechanical scribe has affected the substrate since a line appears on the substrate on either side of the spread-trim loop. The stylus was brought down on the extreme left of the spread-trim loop and moved from left to right cutting out the spread-trim loop and continuing across the ceramic substrate and finally cutting into the main body of the resistor. The movement of the tungsten probe in the arc trim method was carried out analogously. However, arcing does not, of course, occur on the insulating substrate. It can be seen that no such abrasion is present on the ceramic substrate. Photograph 8, at a magnification of 100X, shows only the spread-trim loop of the middle resistor in photograph 7. The substrate damage from the mechanical scribe is more clearly evident as well as the lack of it with the arc-trim cut. The actual "tailings" scraped from the substrate can be seen in photograph 9, taken at a magnification of 250X. Photographs 10 and 11 show the mechanical and arc cuts, respectively of photograph 8 at a magnification of 500X.

As mentioned earlier, the pressure which the tungsten probe exerts on the substrate is practically negligible, Photograph 12 displays another test which was carried out to determine whether just moving the probe across a resistor without trimming (power shut off) would change the resistor. The nichrome resistor material is much softer than the ceramic substrate and much more susceptible to damage from the probe. In the test, the probe was moved from left to right arcing part of the way, then simply moving over the resistor material and then finally arcing the last one-third.

After the first arcing step, the resistance was noted. Then after passing over the middle one-third of the resistor, the resistance was again measured. No resistance change could be detected. This test was repeated with similar results on several spread-trim loops. Photographs 13 and 14 show the lower and upper resistors respectively of photograph 12 at a magnification of 50X. Some light resistor damage is evident in photograph 13. However, as stated before, no change in the total 2R resistance could be detected. Photographs 15 and 16, at a magnification of 100X, display again the lower and upper resistors respectively.

Photograph 17, shows an interesting effect which occurred somewhat accidentally while a substrate was being removed from the header packaging container. The unit was evidently subjected to some stress and the substrate cracked along one of the mechanical scribes and not along an adjacent electrically arced cut. This confirms an earlier stated suspicion, namely, that a mechanical stylus severly stresses the substrate, to the point where catastrophic failure can occur, an obviously undesirable effect.

Photographs 18 and 19 show a laser trim and an arc trim side by side. The magnification for both is 50X. The photographs are, again, of one of the spread-trim loop resistors on a GH1039 circuit. The electrical arc appears as a cleaner, more highly resolved line of vaporized resistor material, while the laser trim appears to leave resistor material behind and is poorly defined. The width of the arc cut is approximately 0.0002 inches. The poor quality of the laser trim is more evident in photograph 20 where the substrate appears as a different texture of black between the region on the left and the substrate region exposed after the resistor material had been vaporized away. Note also the fine line on the substrate to the left of the resistor indicating some substrate damage as the laser beam passed over the insulating substrate. There is no such line on the substrate adjacent to the electrically-arc region since the substrate is an insulator and the arc is extinguished. Also, there is very little pressure on the tungsten stylus.

Experiments were conducted in order to assess the amount of substrate damage in the actual channel of the arc cut. All three trim methods: arc, laser and mechanical are somewhat violent. The characteristics of the mechanical and laser cuts have been described and the amount of substrate damage noted. The arc cut is somewhat more difficult to assess because it is not thought to be severe (due to the low pressure of the tungsten stylus) and occurs only in the channel of the cut (it is self-extinguishing when bare substrate is reached). Chemical etching of the nichrome in the cut region along with microscopy was employed. There is evidence of some removal of substrate material due to the arc process but this may be just the adherance layer which binds the nichrome to the substrate.

The general conclusion reached was that the arc trim process does the least damage to the substrate of the three basic trim methods: arc. mechanical and laser. Furthermore, the arc cuts have generally been finer, cleaner and more highly resolved.

9.0 DYNAMIC TRIM WITH ACTIVE DEVICES (SERVO-LOOP SIGNAL CONDITIONER)

A trim of thin film resistors on a substrate containing active devices was attempted (servo-loop signal conditioner, GH1042). See figure 7 for details of the circuit. Two experiments were carried out to determine whether active devices would be damaged when thin-film resistors, in close proximity to the devices, were trimmed.

In the first, it was decided to trim the resistors connected to the input of the 709 operational amplifier. One end of each of 6 resistors (RIA-RIF) is brought out to pins 1,2,3,5,6,7. The other ends are connected the inverting input of the op-amp and brought out to pin 20. Since RIA equals RIF it was decided to leave these two untouched so that the amplifier could be checked at unity gain before and after the trim. Trims were confined to RIB, RIC, RID and RIE. Three tests were usedto check the op-amp performance: overall unity gain operation, input bias current, and input offset voltage. There was no noticeable change in operation before and after the trim. The maximum undistorted voltage was 9.0 volts r.m.s. The bias current was .3μA and the input offset voltage was -2.0mv. During the trim of RIB through RIE, the inverting input (pin 20) was grounded but main power (+ and -15V) was applied to the amplifier.

In the second experiment, RIF was included as a feedback resistor to give a unity gain amplifier (RIA was connected across the input to ground) and it was trimmed to give an increase in gain. Testing was done both with the input (pin 20) grounded and ungrounded and main power and input signal applied. No change in circuit operation was detected.

The results of the second test were somewhat surprising since it was felt that, with the op-amp operating and the input ungrounded and exposed, the high voltage from the trim probe on the feedback resistor would cause a failure. However, a simple analysis shows that for a specific approach to the trim, the voltages on the op-amp can be quite reasonable. Figure 9 shows a schematic of the trim circuit used with the 709 (Z1) amplifier of the GH1042. If the assumption is made that the resistance across the arc is approximately $10^6\Omega$, then for the situation where the trim is conducted on the feedback resistor (RIF) near the op-amp output end, such that $RIF_2 \approx 0$, $RIF_1 \approx 5x10^4\Omega$, the current flow is determined by the arc resistance and the limiting $10^6\Omega$ resistor in series with the pulse circuit. The current through the output of the op-amp is thus approximately $5x10^{-4}$ amp. The maximum voltage across the input to the op-amp is approximately .025 volts which is reasonable. If on the other hand the trim is carried out near the op-amp input end of RIF such that $RIF_1 \approx 0$, $RIF_2 \approx 5x10^4\Omega$, then it is easy to see that the voltage across the input will be approximately 12.5 volts. The maximum allowable is approximately 5 volts. This situation should be avoided, and was the case in the trims conducted.

The results with the dynamic trim on the GH1042 containing active devices lead to the conclusion that the arc-trim method can be compatible with trim situations where the electronic circuit must be operating in order to be adjusted properly.

10.0 TANTALUM THIN-FILM RESISTORS

Experiments were performed to see whether the arc trim method developed with nichrome was more general and could be used on other materials such as tantalum. No difficulty was encountered.

The optimum method of trimming the tantalum thin-film resistors supplied by Garrett was found to be similar to that employed in trimming nichrome. The voltage on the pulse generator was doubled so that the voltage on the tungsten probe was approximately 2000 volts, however, all other generator parameters remained identical to those used in trimming the nichrome. Generally, it was found that the tantalum could be trimmed at a high slue rate with a clean, narrow cut being maintained over the length of the trim. A typical trim is shown in photograph 20.

A major (100%) trim was performed into the body of a tantalum resistor and then the T.C.R. of this resistor compared to an untrimmed resistor. The T.C.R. was found to be -112 p.p.m./°C for each resistor, with no noticeable change due to trimming. The results obtained are summarized in Table 6.

11.0 CONCLUSIONS

It is concluded from this work that the arc-trim method represents a viable alternative to the mechanical or the laser trim systems. The cost and physical simplicity of the equipment and trim procedure are obvious strong points. Adding to this are the results of the experiments carried out, which demonstrate that no device characteristics are seriously altered, by arc trimming.

TABLE 1

Data showing typical trim resistance changes that can be made by cutting into the body of the spread trim loop resistors of the GH 1039 circuit. The 2R resistors are being trimmed.

Photograph Number	Resistance Before Trim (OHMS)	Resistance After Trim (OHMS)	Change in Resistance (OHMS)
1	40010	40025	+15
2	40084	40086	+2
3	38980	39005	+25
4	38910	38915	+5
5	38953	38952, 38956, 38961	-1, +3 +8
6	40064	40060, 40063, 40065	-4, -1, +1

TABLE 2

Results of TCR measurements on 6 typical 2R resistors on the GH 1039 circuits, three of which were trimmed and three untrimmed. The untrimmed resistors served as reference. The resistors trimmed were associated with the .01% spread trim loop.

	Trimmed			Untrimmed		
Temperature °C	Resistor A R:ΔR (OHMS)	Resistor B R:ΔR (OHMS)	Resistor C R:ΔR (OHMS)	Resistor D R:ΔR (OHMS)	Resistor E R:ΔR (OHMS)	Resistor F R:ΔR (OHMS)
-50	42036 >25	41940 >23	42233 > 24	42040 > 24	41639 > 26	39222 > 24
-30	42061 >24	41963 >23	42257 > 23	42064 > 22	41665 > 24	39246 > 23
-10	42085 >27	41986 >24	42280 > 26	42086 > 26	41689 > 26	39269 > 25
+10	42112 >24	42010 >23	42306 > 24	42112 > 23	41715 > 25	39294 > 23
+30	42136 >26	42033 >23	42330 > 23	42135 > 23	41740 > 25	39317 > 23
+50	42165 >24	42056 >23	42353 > 23	42158 > 22	41766 > 26	39340 > 23
+70	42186	42079	42376	42180	41791	39363
Average TCR (ppm/°C)	29.7	27.4	28.4	27.4	30	29.9

TABLE 3

Results of T.C.R. measurements on a typical trimmed and untrimmed resistor on the GH1025 circuit. The untrimmed resistor served as a reference. The R_6 resistor was trimmed for an increase of 10%. Trimming was into the main body of the resistor.

Temperature °C	R_8 (Untrimmed reference)		R_6 (Trimmed for a +10% increase)	
	R (Ohms)	ΔR	R (Ohms)	ΔR
-50	415.87		879.40	
		> .58		> 1.1
-30	416.45		880.50	
		> .50		> 1.09
-10	416.95		881.59	
		> .53		> 1.1
+10	417.48		882.69	
		> .56		> 0.89
+30	418.04		883.58	
		> .49		> 1.05
+50	418.53		884.63	
		> .51		> 1.11
+70	419.04		885.74	
		> .54		> 1.09
+90	419.58		886.83	
Average T.C.R. (p.p.m./°C)	63.5		61.0	

TABLE 4

Results of T.C.R. measurements on a typical trimmed resistor subjected to a 100% resistance increase. The trimmed resistor was R_1 of the GH1025 circuit, with the trim being made into the two trim pads provided, as well as into the main resistor chain. R_2 was used as a reference resistor.

Temperature °C	R_2 (Untrimmed reference)		R_1 (Trimmed for a 100% increase)	
	R	ΔR	R	ΔR
	(OHMS)		(OHMS)	
-70	437.16		848.81	
		> .64		> 1.36
-50	438.80		848.17	
		> .71		> 1.54
-30	438.51		849.71	
		> .61		> 1.42
-10	439.12		851.13	
		> .68		> 1.52
+10	439.80		852.65	
		> .73		> 1.53
+30	440.53		854.18	
		> .67		> 1.40
+50	441.20		855.58	
		> .81		> 1.66
+70	442.01		857.24	
		> .75		> 1.55
+90	442.76		859.79	
Average T.C.R. (p.p.m./°C)	80 ± 10		88 ± 10	

Table 5

Resistance stability test performed on 2R resistors of the GH 1039 circuit. The resistors were trimmed by trimming into the body of the spread trim loop resistors. The resistors were cycled twice from -65°C to +125°C.

2R Resistance Value (ohms)

Resistor Number	Before Cycling	After Cycling
1	42131	42131
2	42134	42134
3	42135	42135
4	42134	42134
5	42139	42139
6	42138	42138
7	42134	42135
8	42031	42032
9	42131	42130
10	42327	42325
11	41857	41857
12	41738	41738
13	39315	39314

TABLE 6

Results of a T.C.R. test performed on tantalum resistors to determine the effect of arc trimming. A typical circuit was provided by Garrett. One resistor was used as a reference while another had its resistance increased by 100%.

Temperature	Untrimmed Reference Resistor		Trimmed Resistor (100% Increase)	
°C	R	ΔR	R	ΔR
	(Ohms)		(Ohms)	
-70	443.65		392.04	
		> 1.08		> .93
-50	442.57		391.11	
		> 1.08		> .95
-30	441.49		390.16	
		> 1.07		> .96
-10	440.42		389.20	
		> .95		> .85
+10	439.47		388.35	
		> .95		> .86
+30	438.52		387.49	
		> .96		> .85
+50	437.56		386.64	
		> .84		> .78
+70	436.72		385.86	
		> .87		> .78
+90	435.85		385.08	
Average T.C.R. (p.p.m./°C)	-112		-112	

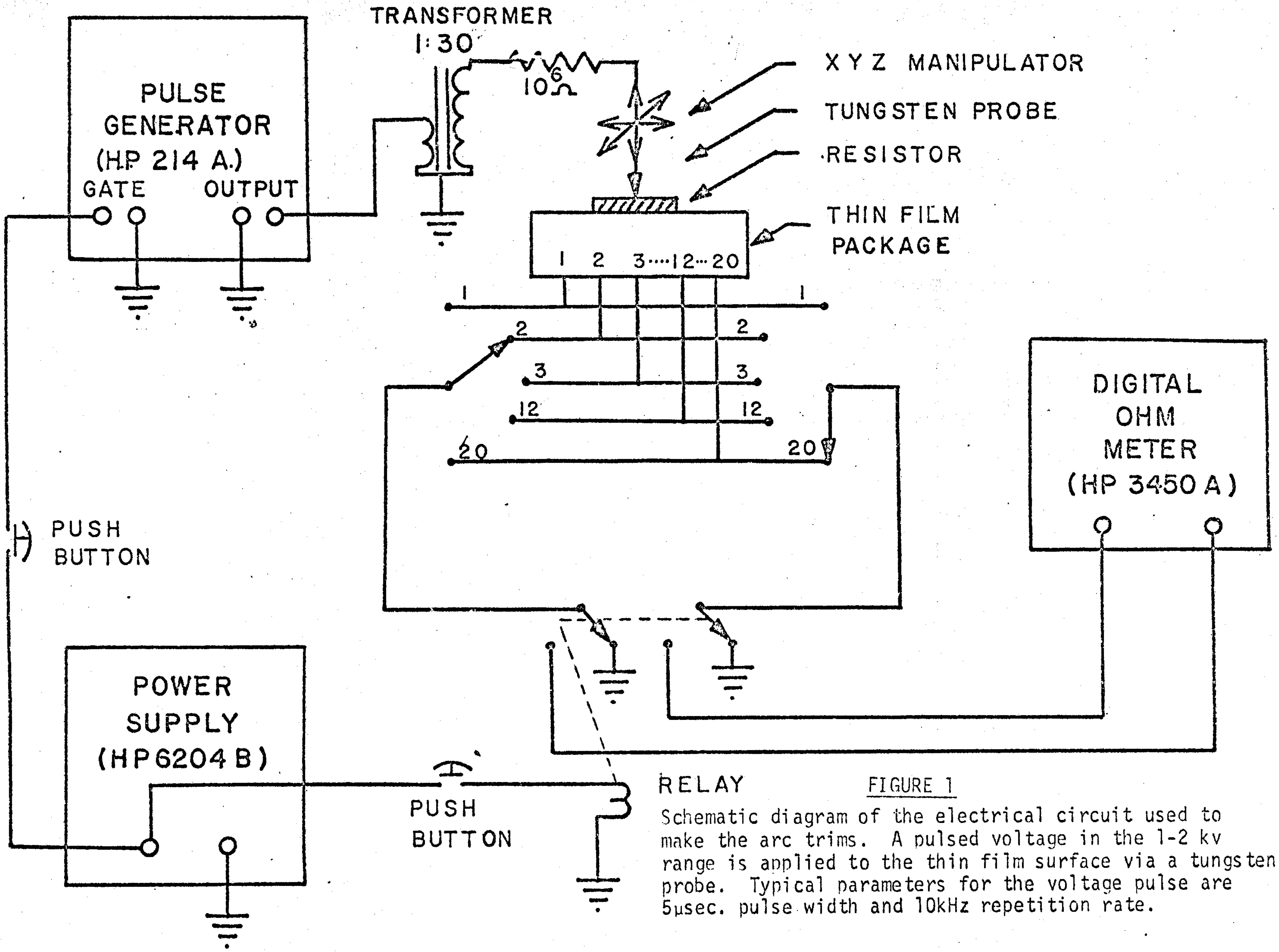

FIGURE 1

Schematic diagram of the electrical circuit used to make the arc trims. A pulsed voltage in the 1-2 kv range is applied to the thin film surface via a tungsten probe. Typical parameters for the voltage pulse are 5μsec. pulse width and 10kHz repetition rate.

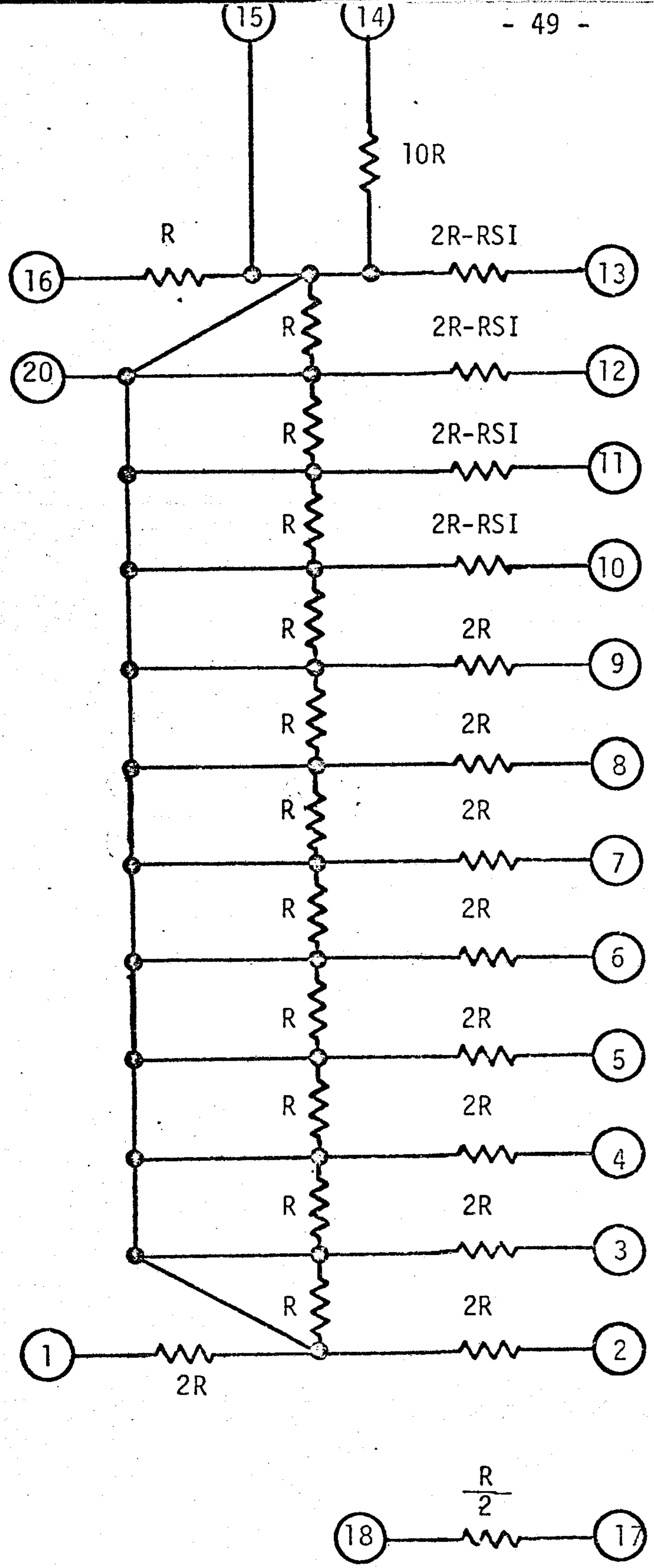

Figure 2: Schematic diagram of the GH1039 circuit, a twelve bit analogue to digital ladder. The R resistors are generally in the 20,000Ω range and the 2R resistors in the 40,000Ω range. RSI is 5Ω.

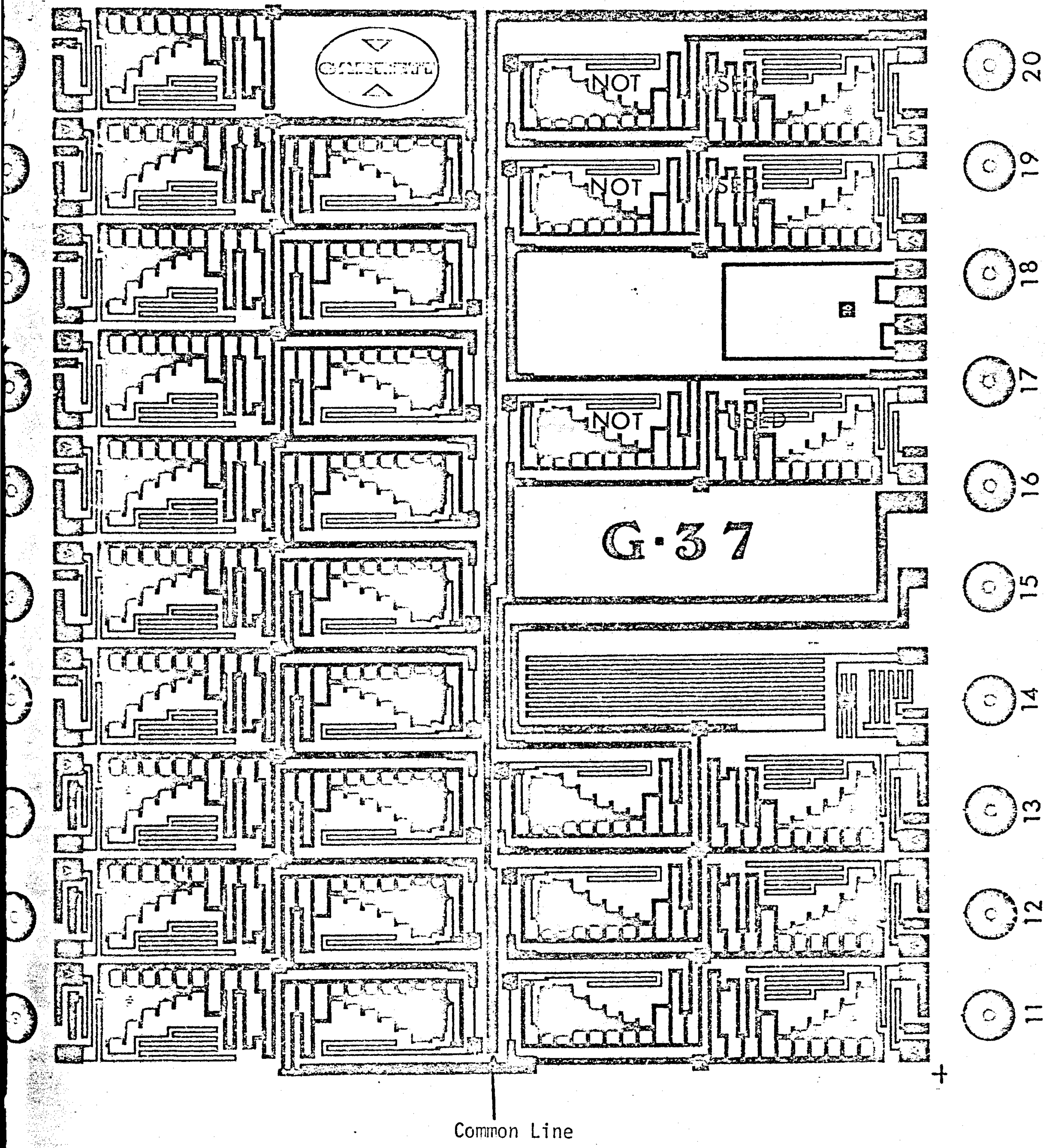

Figure 3: Thin film surface layout of the GH1039 circuit, a twelve bit analogue to digital ladder. The network consists of R-2R blocks as shown in magnified form in figure 4. Connection between blocks is made at pad J.

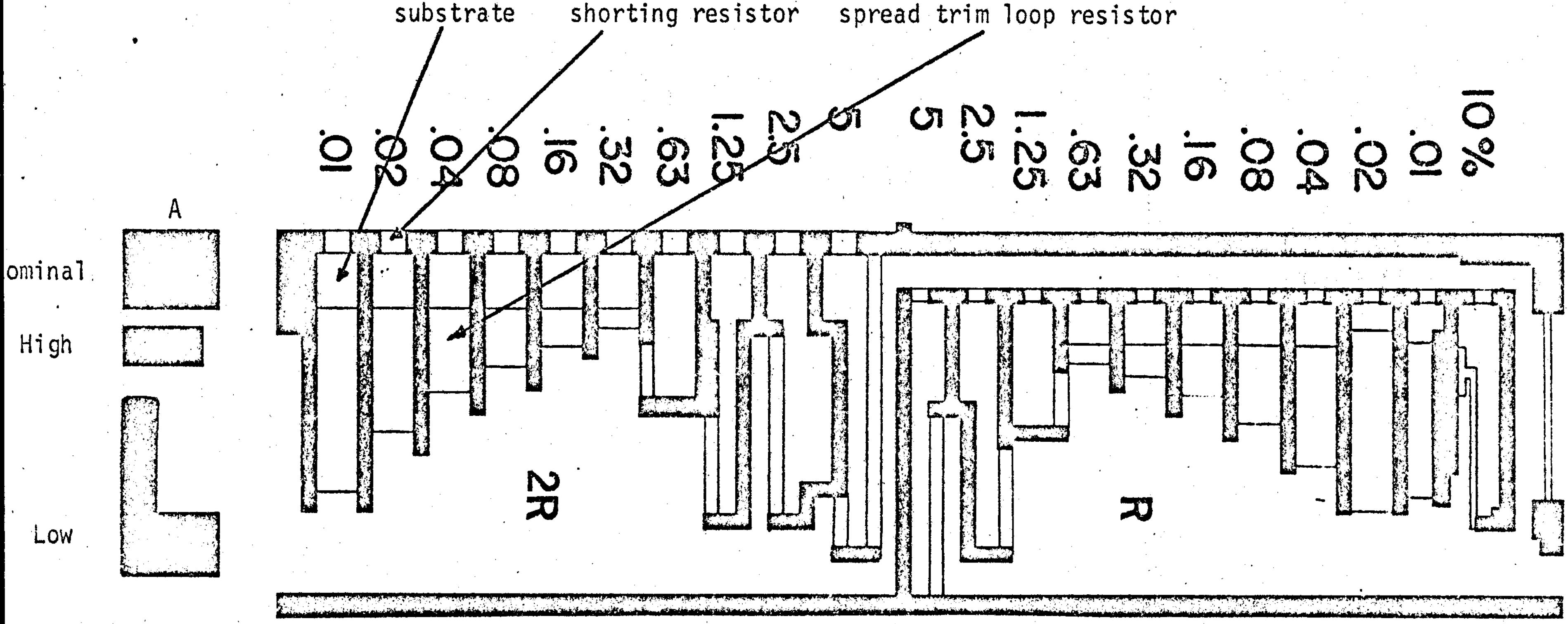

Figure 4: A typical R-2R block contained in figure 3. The main chain resistors are not shown but are present in figure 3. The white regions represent resistors while the black regions represent conductor. The numbers shown indicate the percent change in resistance that can be made by opening the corresponding shorting resistor of the spread trim loop.

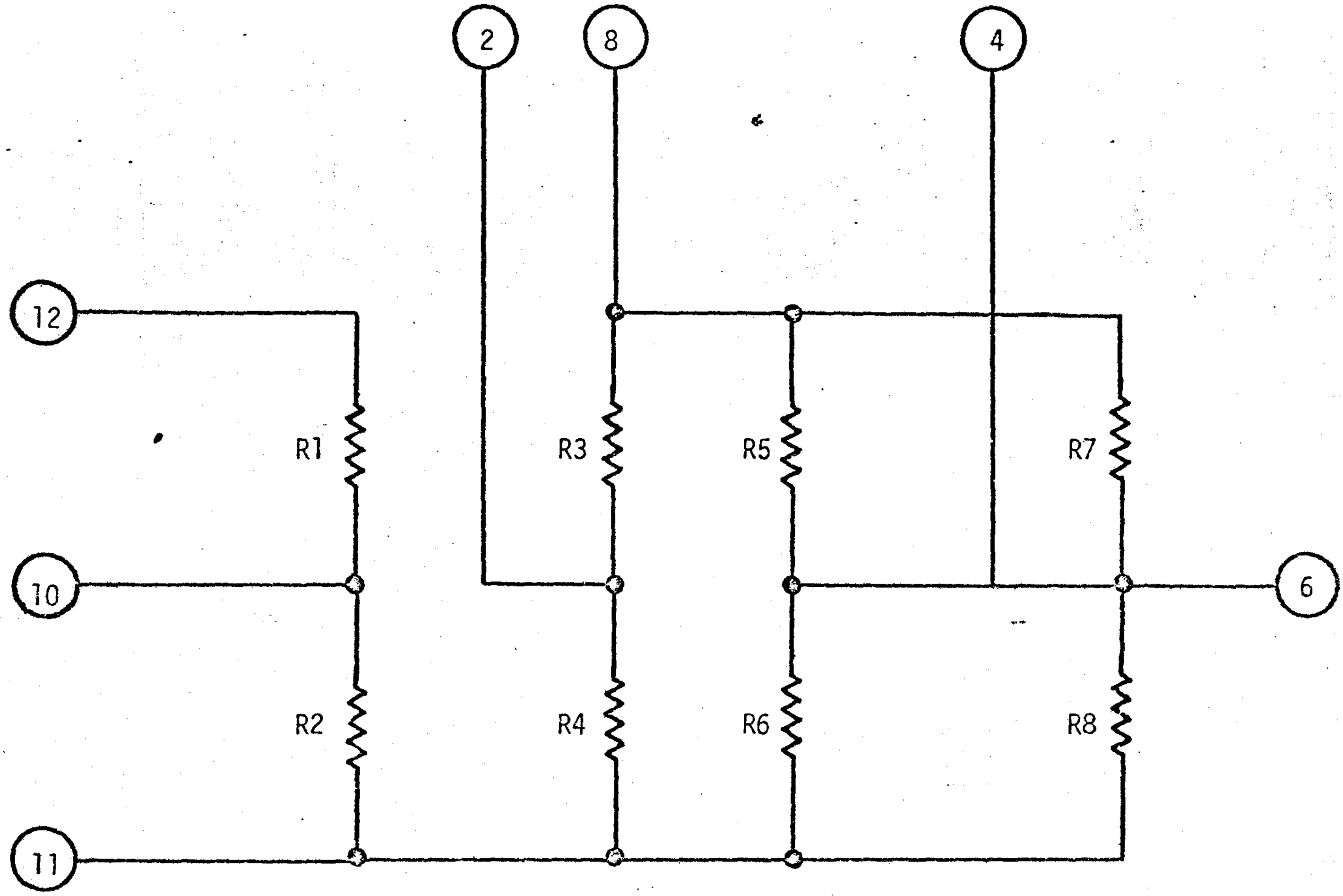

Figure 5: Schematic of the GH1025 sensor bridge resistor network.

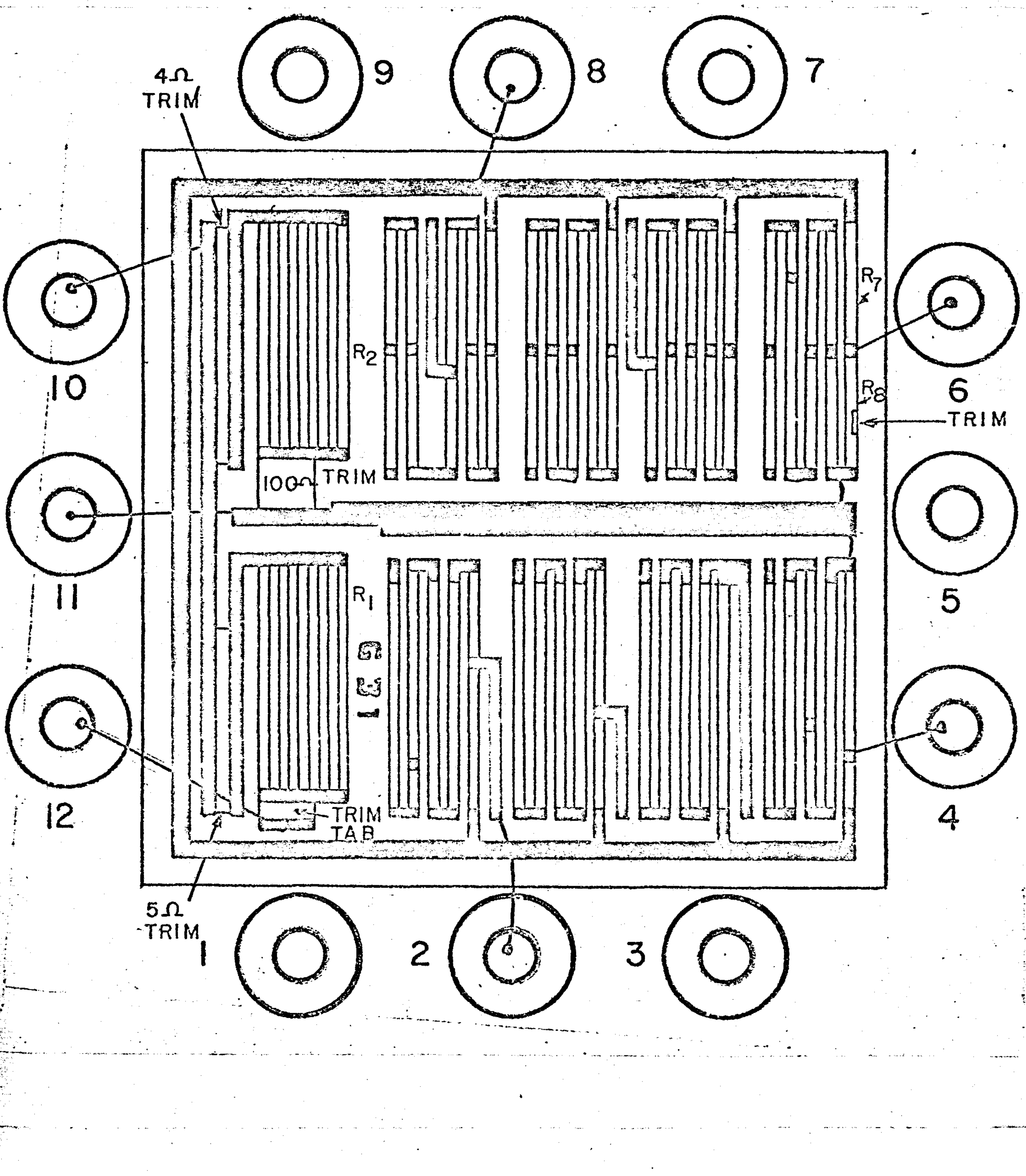

Figure 6: Pictorial layout of the GH1025 circuit, a sensor bridge resistor network. Resistors R_1 and R_2 have two trim tab resistors which are used to adjust their absolute values to the specification values. For the ratio specification, a trim is made into the main body of a resistor as shown (R_8 for example).

GH1042

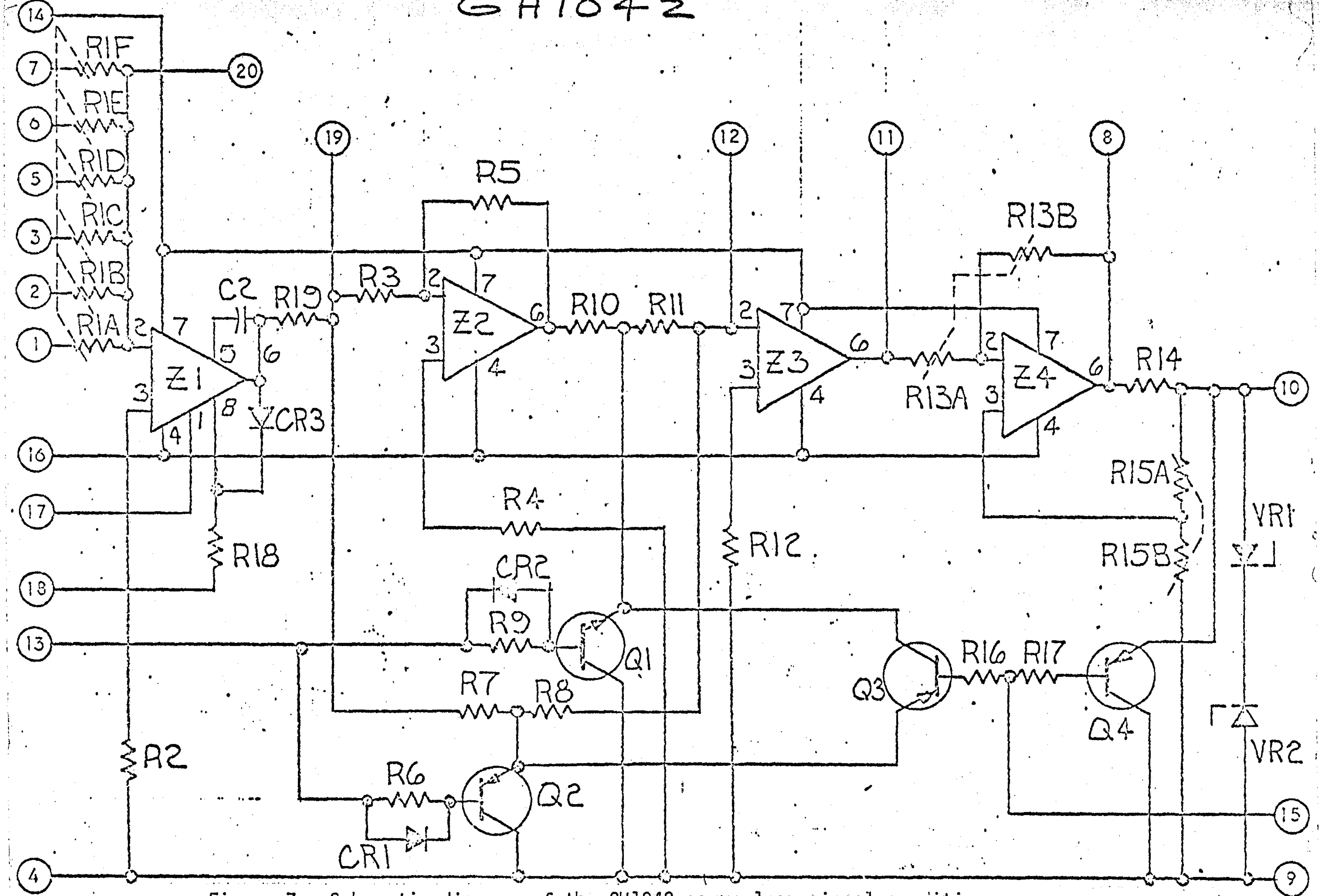

Figure 7: Schematic diagram of the GH1042 servo loop signal conditioner circuit on which dynamic trim tests with operating active devices were carried out. Specifically, the input resistors, RIA to RIF, connected to the Z1,709 operational amplifier were trimmed.

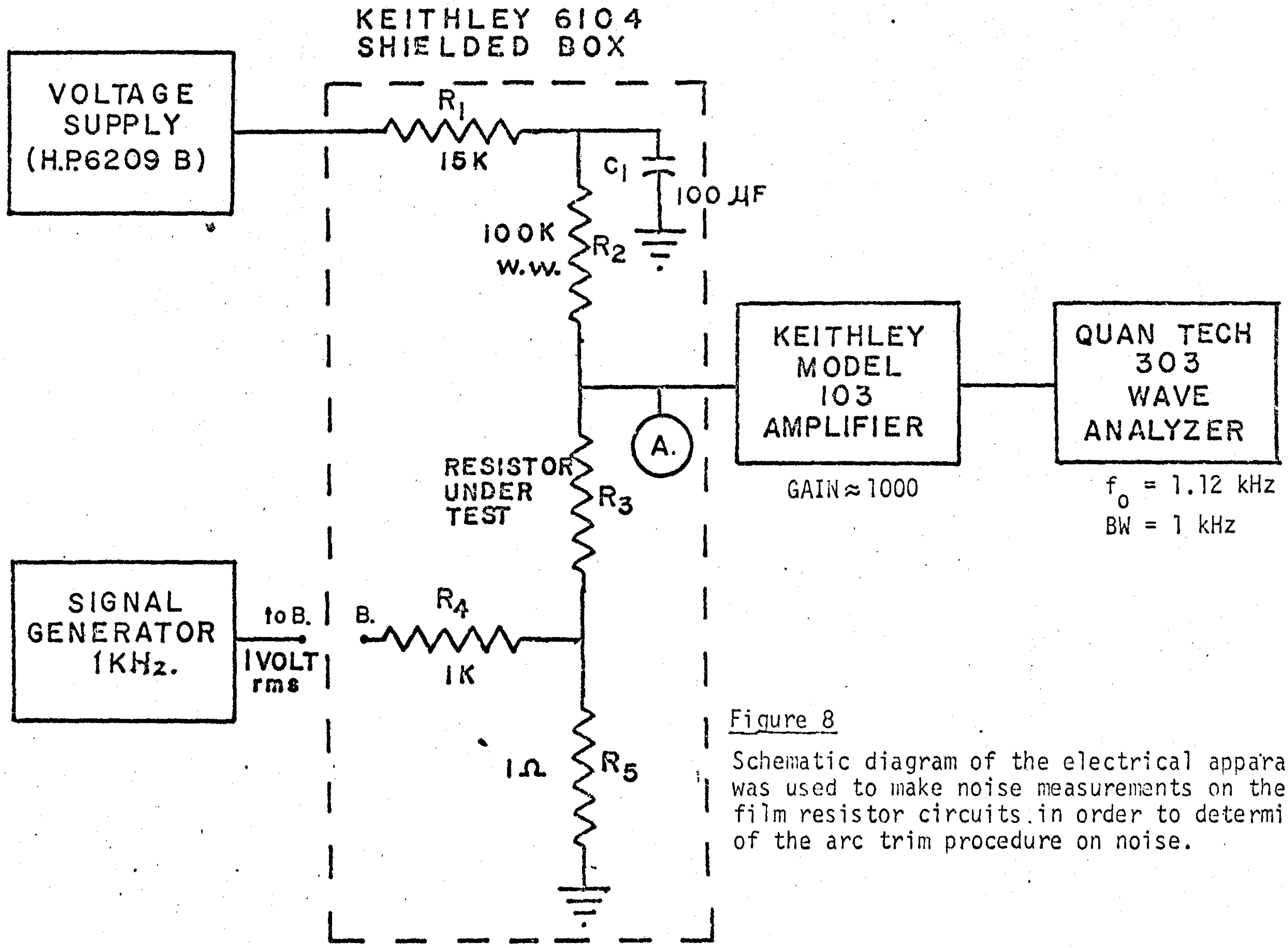

Figure 8

Schematic diagram of the electrical apparatus that was used to make noise measurements on the nichrome film resistor circuits in order to determine the effect of the arc trim procedure on noise.

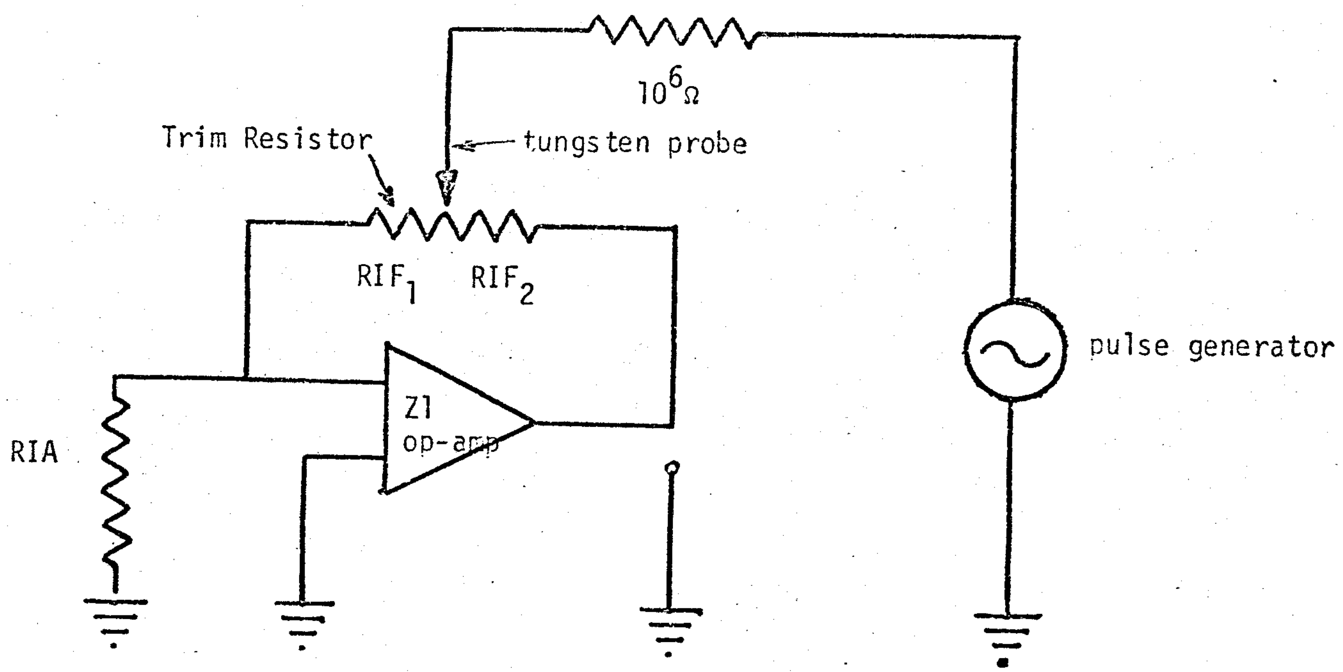

RIF = $RIF_1 + RIF_2 = 5 \times 10^4 \Omega$

RIA = $5 \times 10^4\ \Omega$

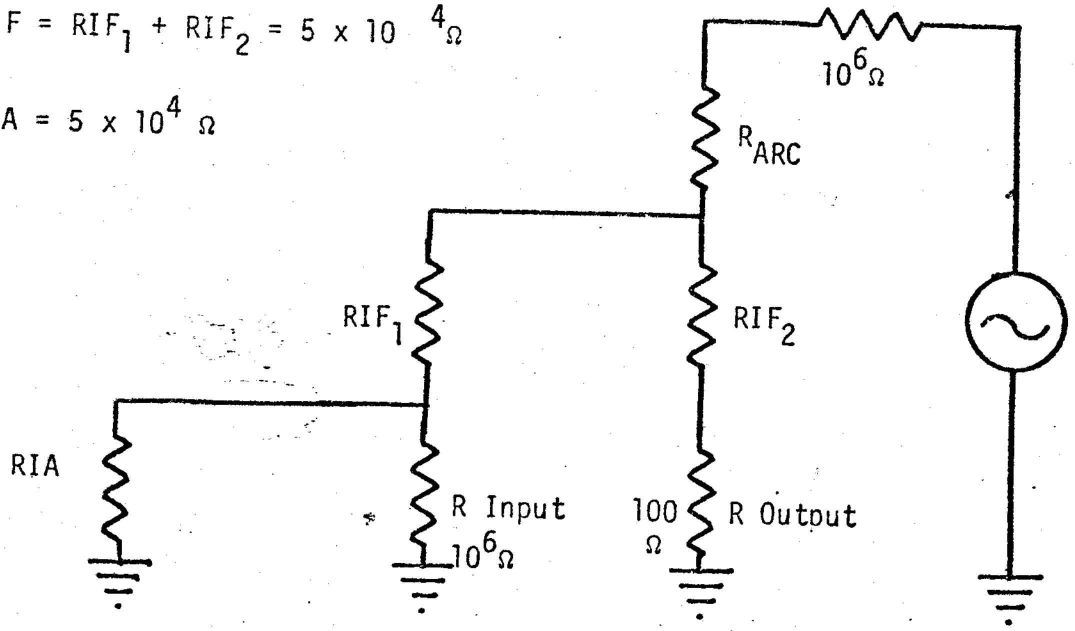

igure 9: Schematic diagram of the circuit used to check the arc trim method on active devices. The op-amp was the Z1,709 unit of the GH1042 circuit. The op-amp was in dynamic operation as an amplifier during the trim and the trim was performed in the feedback resistor, RIF.

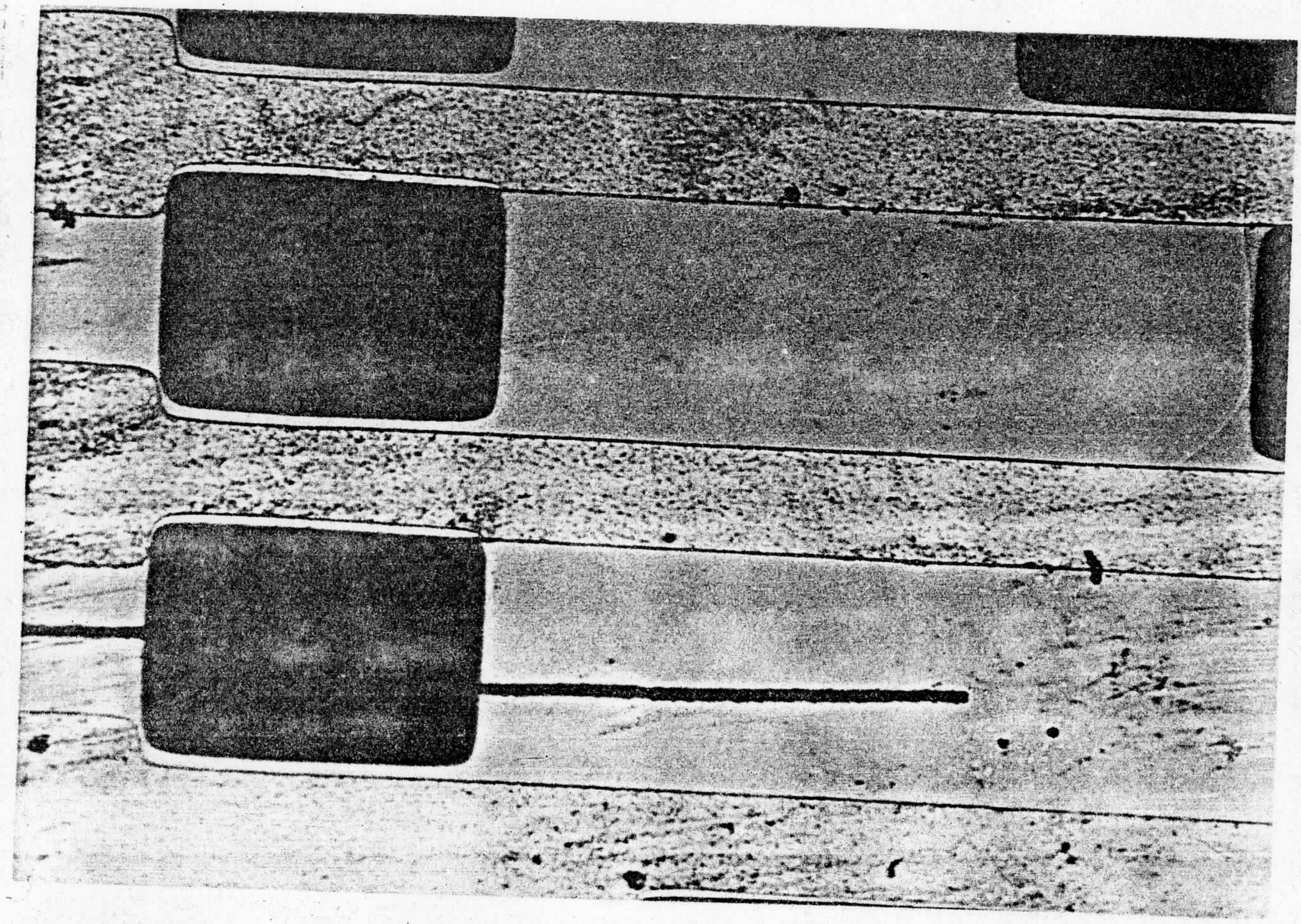

Photograph 1: Photograph of an arc trim made on the .01% spread trim loop of the 2R resistor of GH1039 circuit. The black rectangular region represents bare substrate. On either side is nichrome resistor material. The speckled material is conductor. The cut on the left opens the shorting resistor while the other cut is into the spread trim resistor, approximately 50% of the way through. The cut into the spread trim loop caused a 15Ω change in 2R. Magnification is 25X.

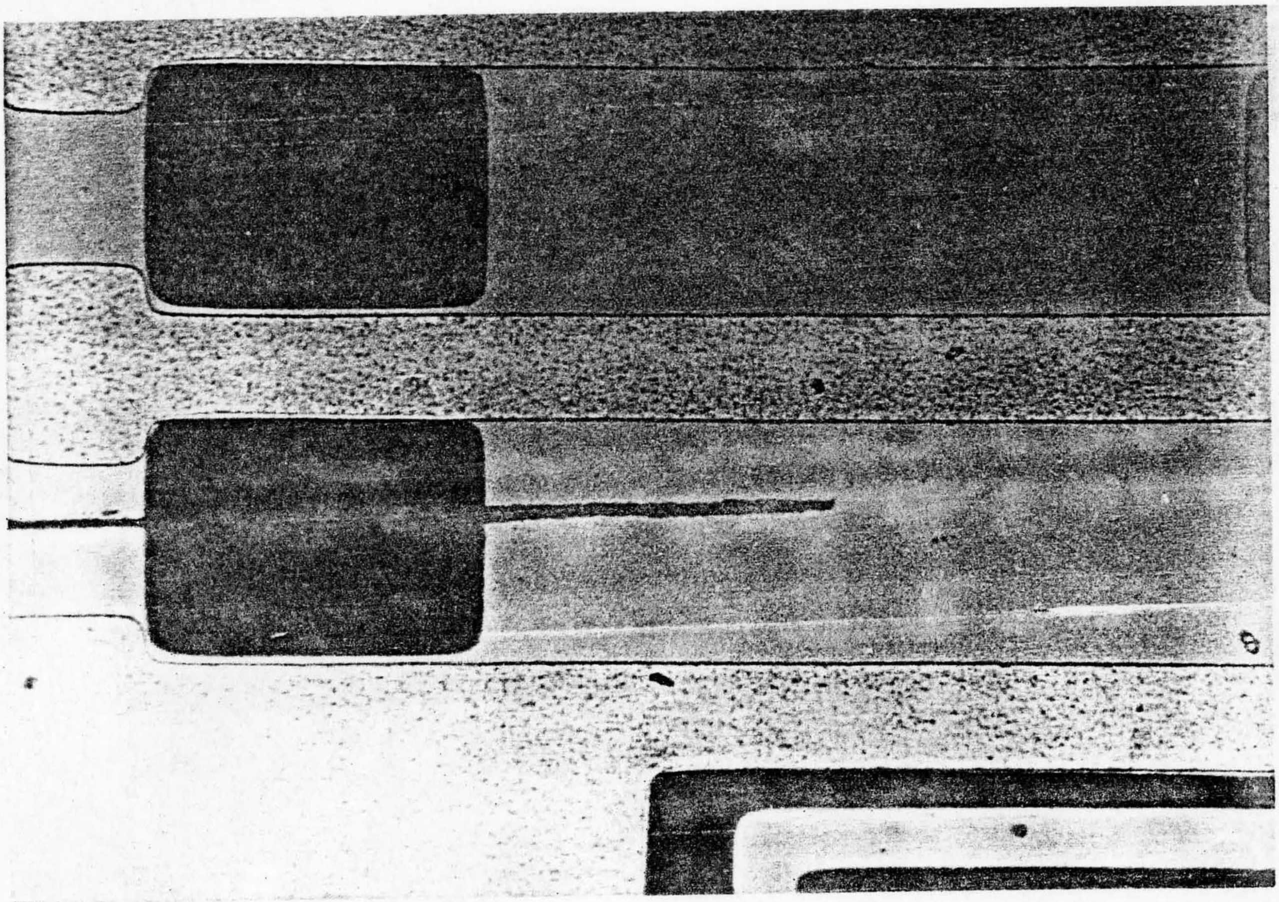

Photograph 2: Identical to photograph 1 except that the .01% spread trim loop has been cut only about 1/3 of the way through. The resistance change is 2 ohms. Magnification is 25X.

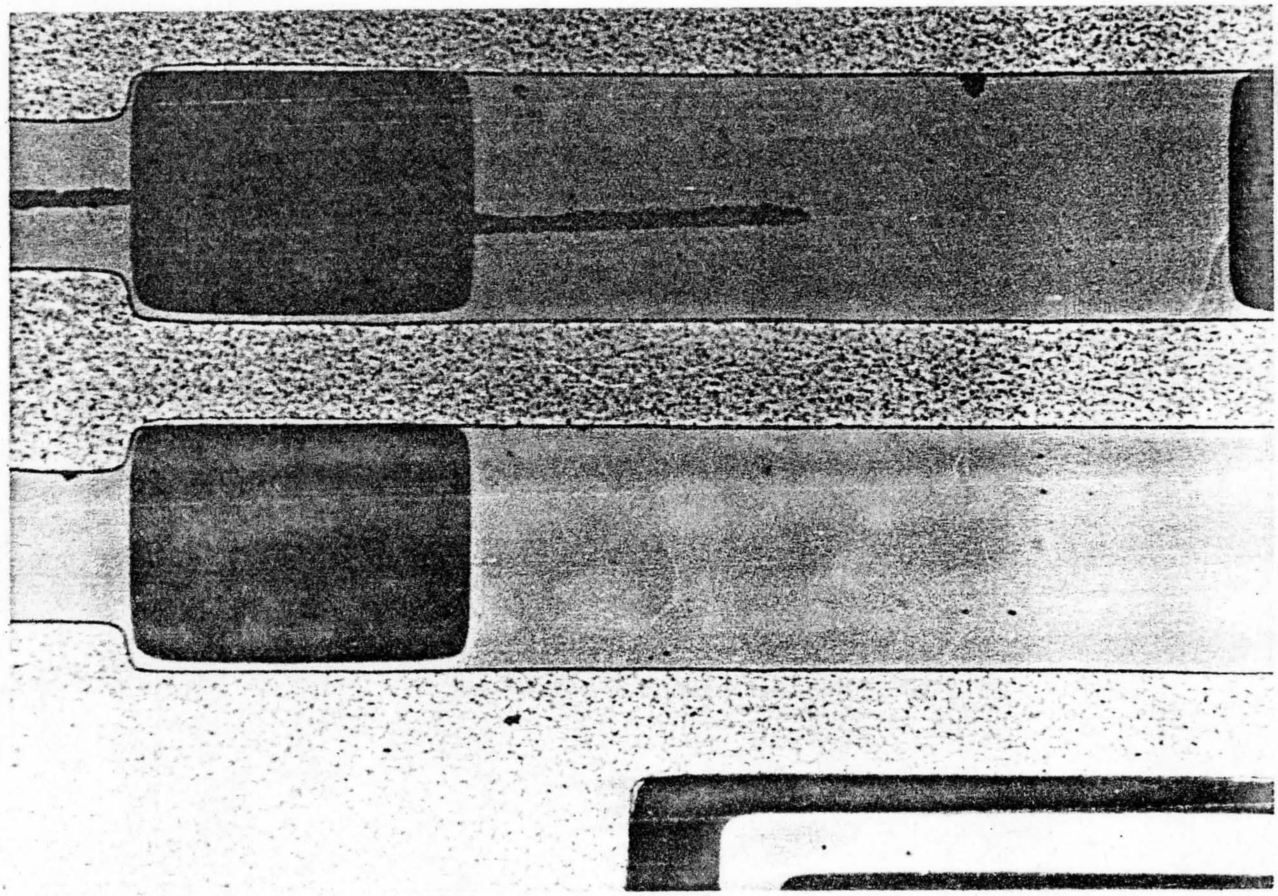

Photograph 3: Identical to photograph 1 except that the .02% spread trim loop has been arc trimmed about 1/2 of the way through. The resistance increase is 25 ohms. Magnification is 25X.

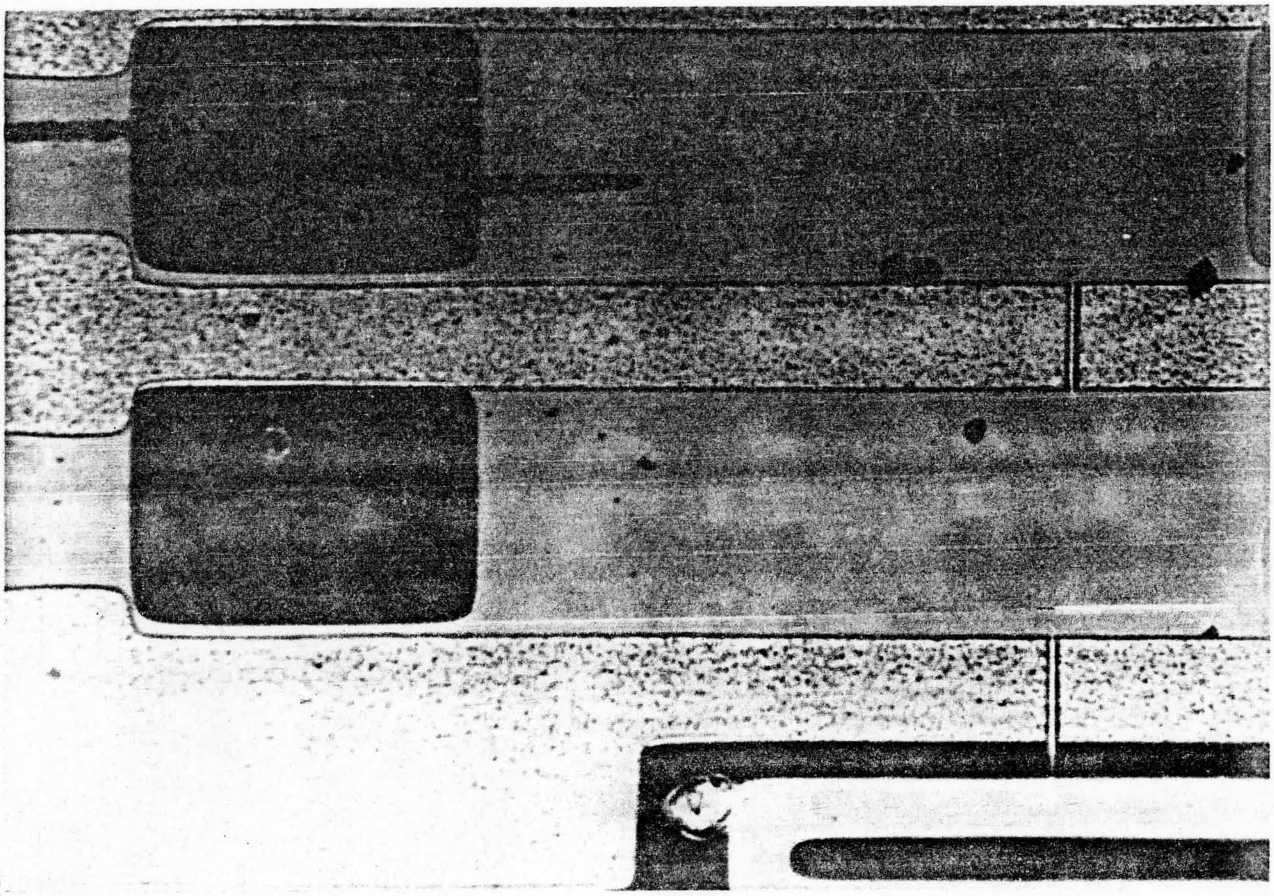

Photograph 4: Identical to photograph 1 except that the .02% spread trim loop has been arc trimmed about 1/4 of the way through. The resistance increase is 5 ohms. Magnification is 25X.

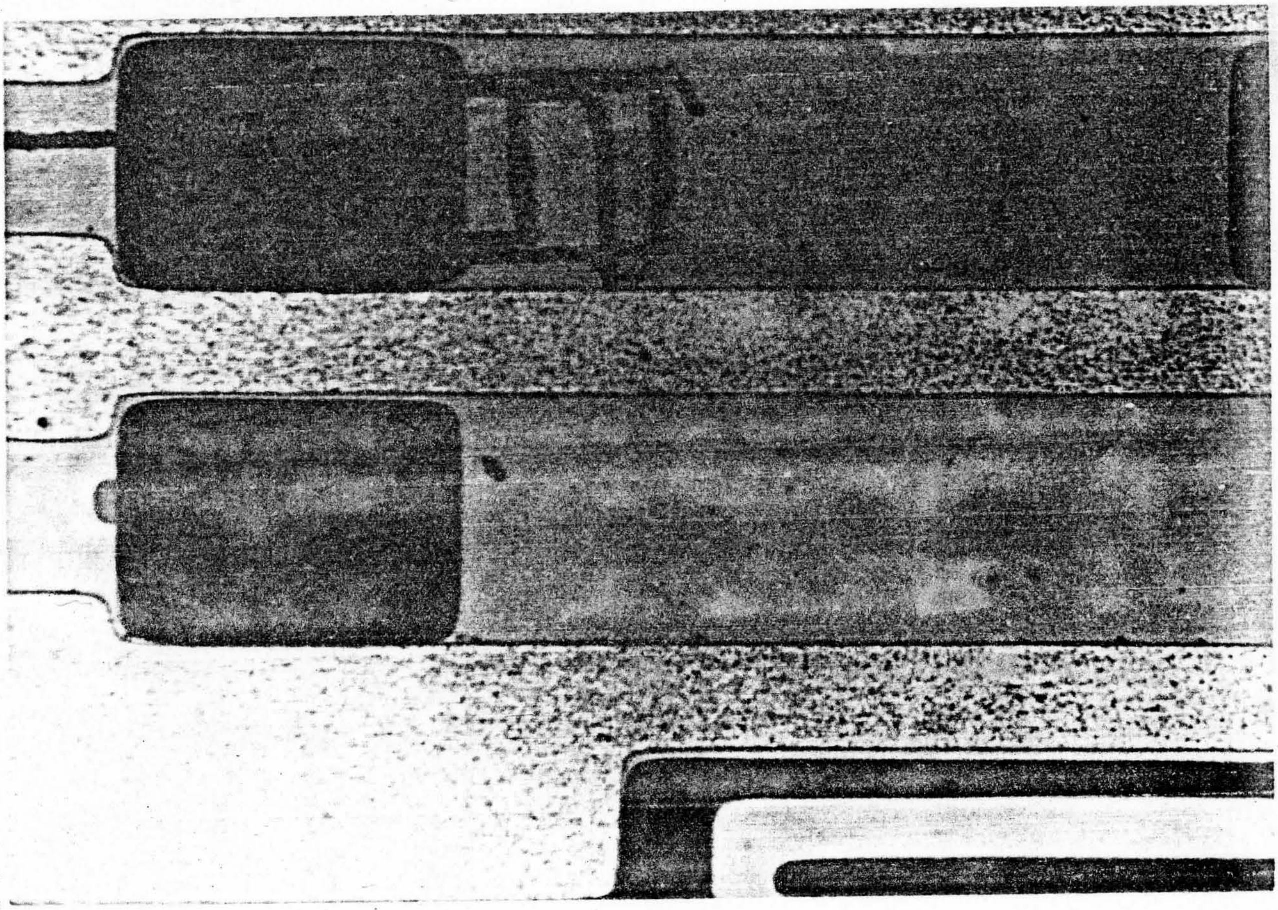

Photograph 5: Identical to photograph 1 except that three rectangular cuts have been made into the .02% spread trim loop. From left to right the cuts decreased resistance 1Ω, increased resistance 4Ω and increased resistance 5Ω respectively. Magnification is 25X.

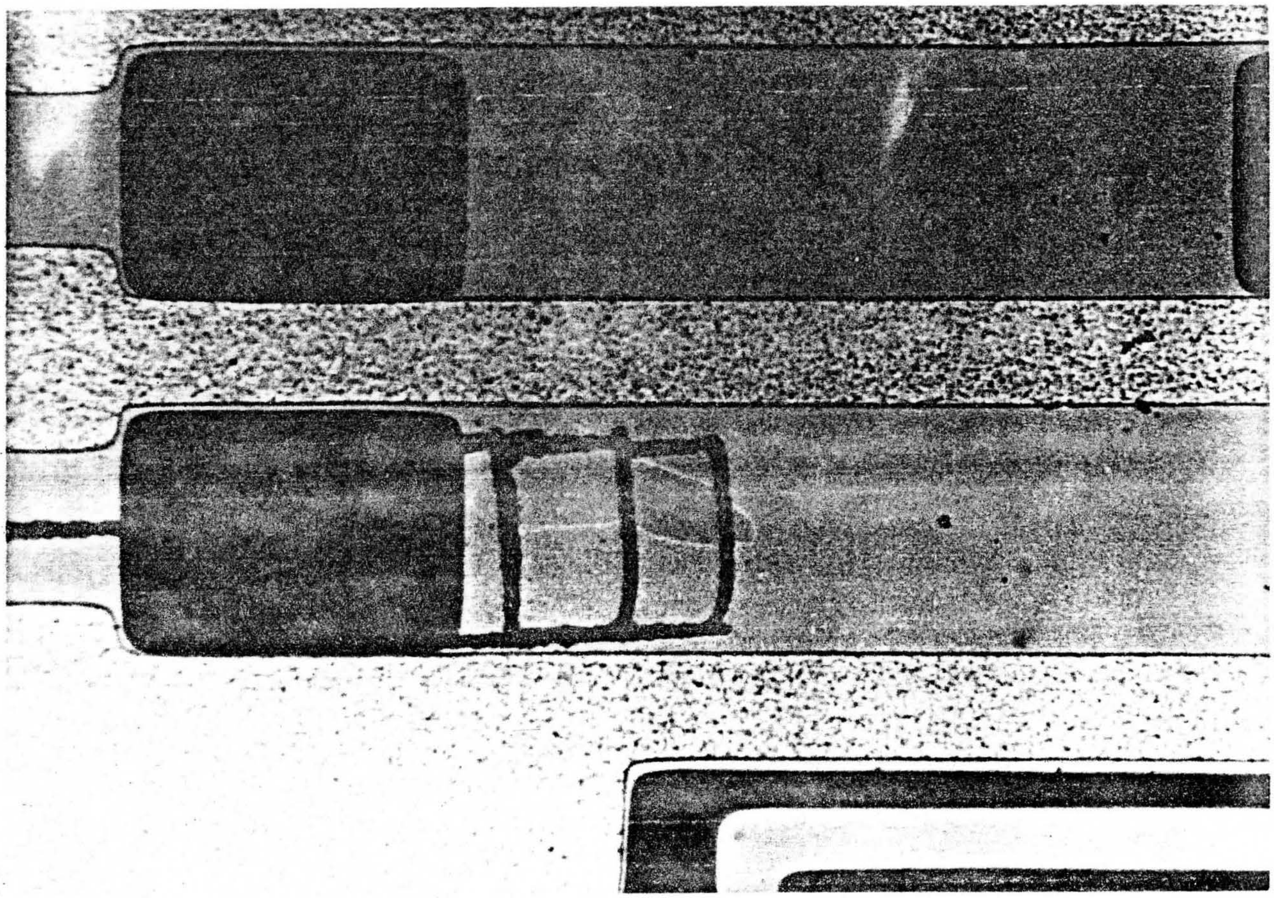

Photograph 6: Identical to photograph 1 except that three rectangular cuts have been made into the .01% spread trim loop. From left to right the cuts decreased the resistance 4Ω, increased resistance 3Ω and increased the resistance 2Ω respectively. Magnification is 25X.

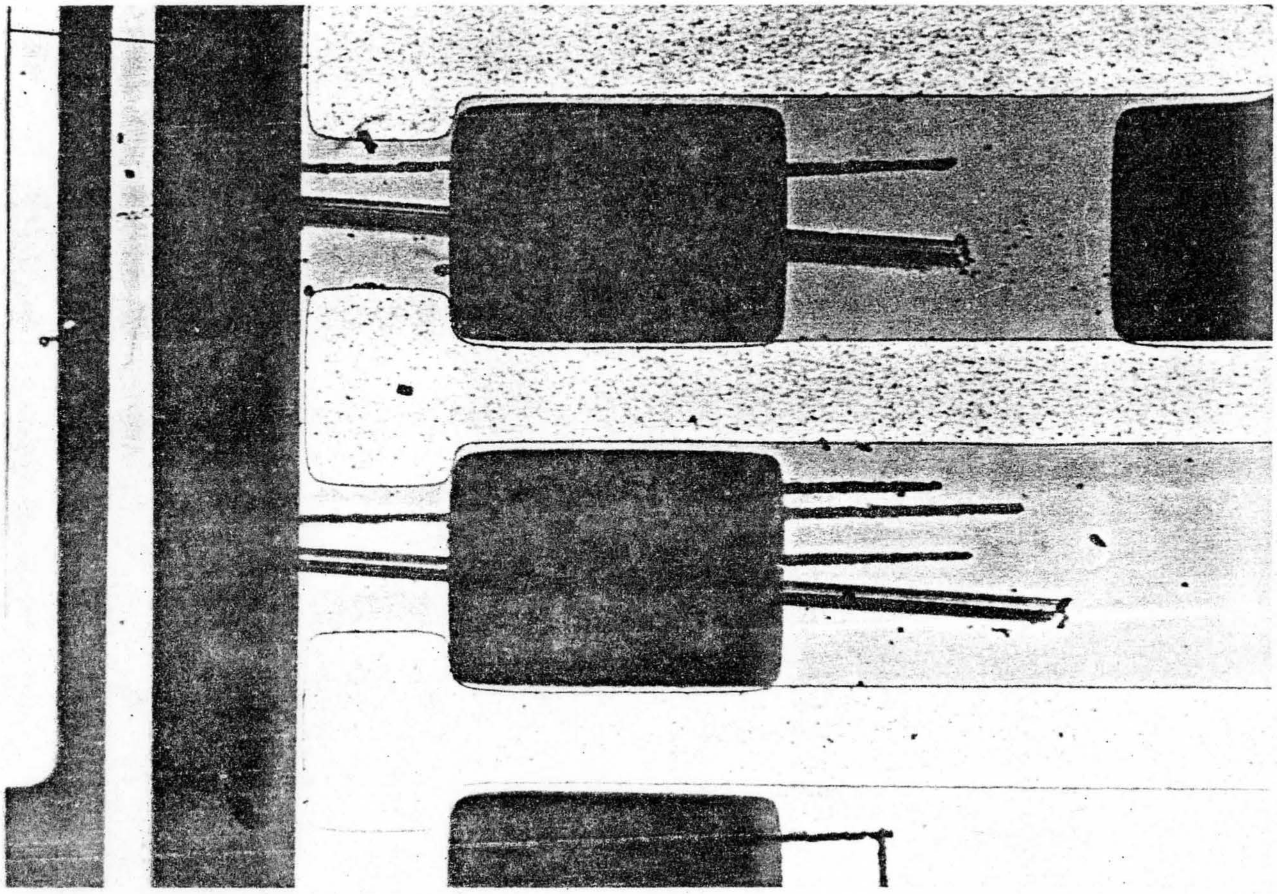

Photograph 7: Comparison of Mechanical and Arc-trim Cuts. The wide cut is due to a diamond stylus while the finer cuts are due to arc-trim. The dark region is substrate. Note the damage on the substrate due to the mechanical cut and lack of it from the arc-trim. Magnification is 25X. The circuit is a GH1039 and the photograph is of the spread trim loop section.

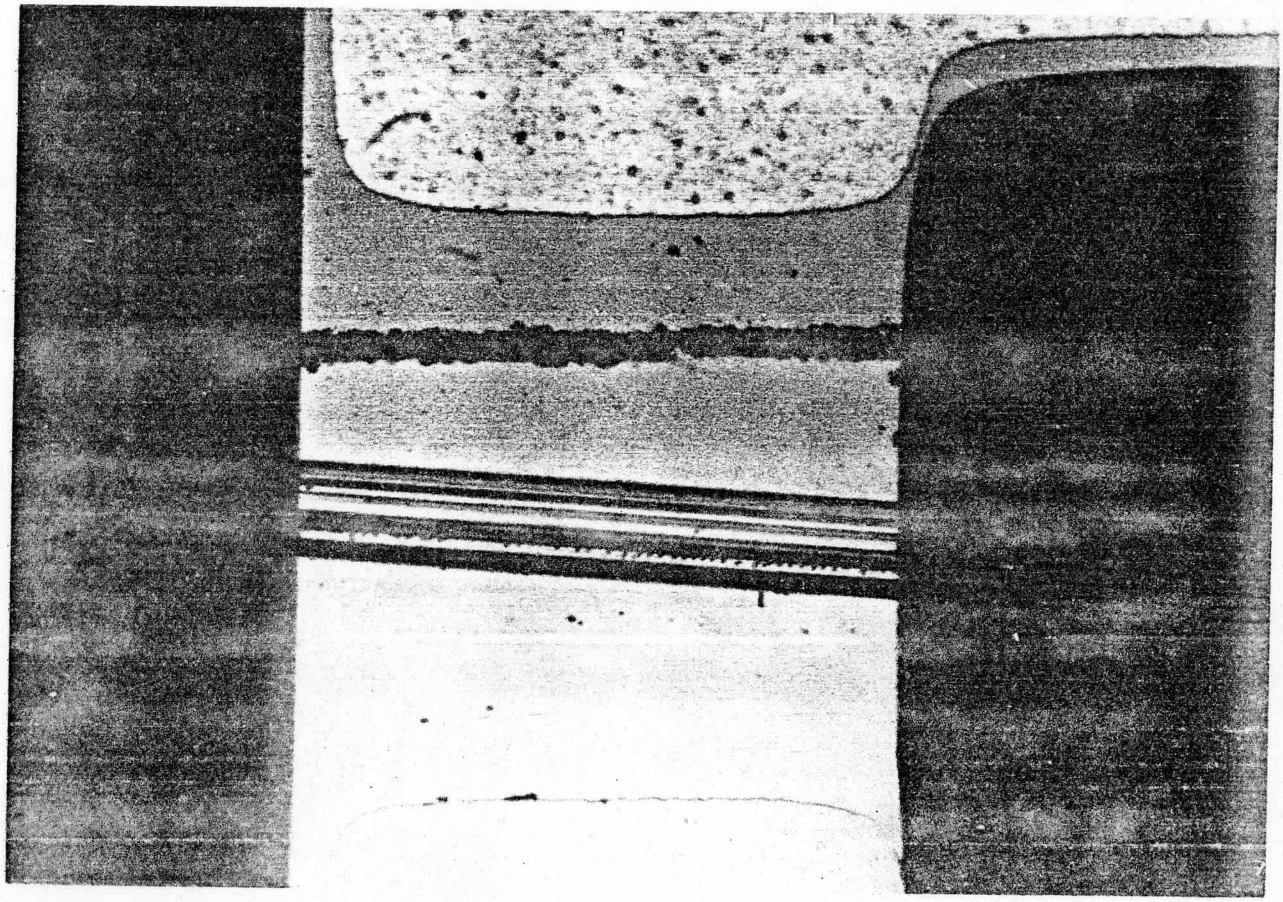

Photograph 8: Comparison of Mechanical and Arc-Trim Cuts. A section of photograph 7 magnified 100X, showing in more detail the cut through a shorting resistor of a spread trim loop on the GH1039.

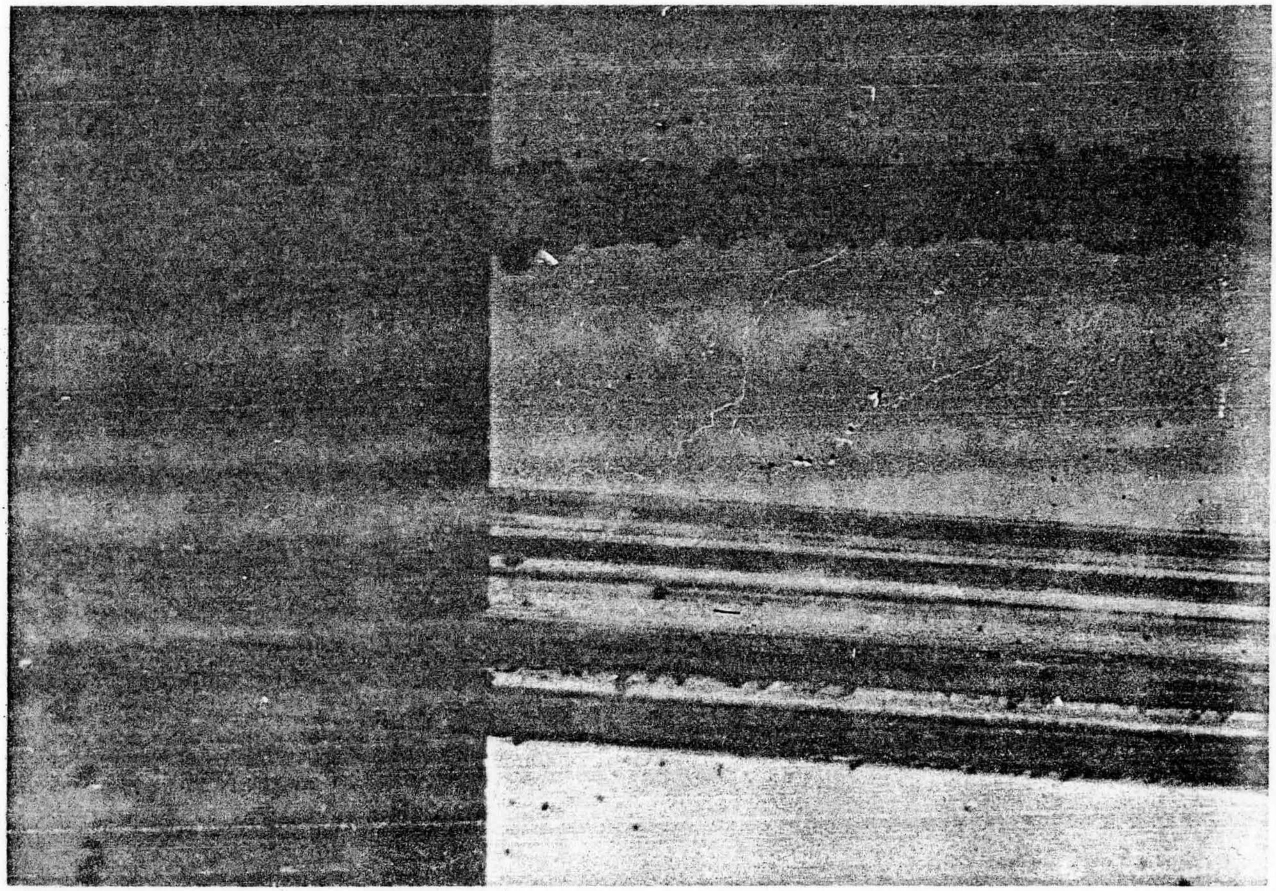

Photograph 9: Comparison of Mechanical and Arc-Trim Cuts. Same section as in photograph 8 magnified 250X.

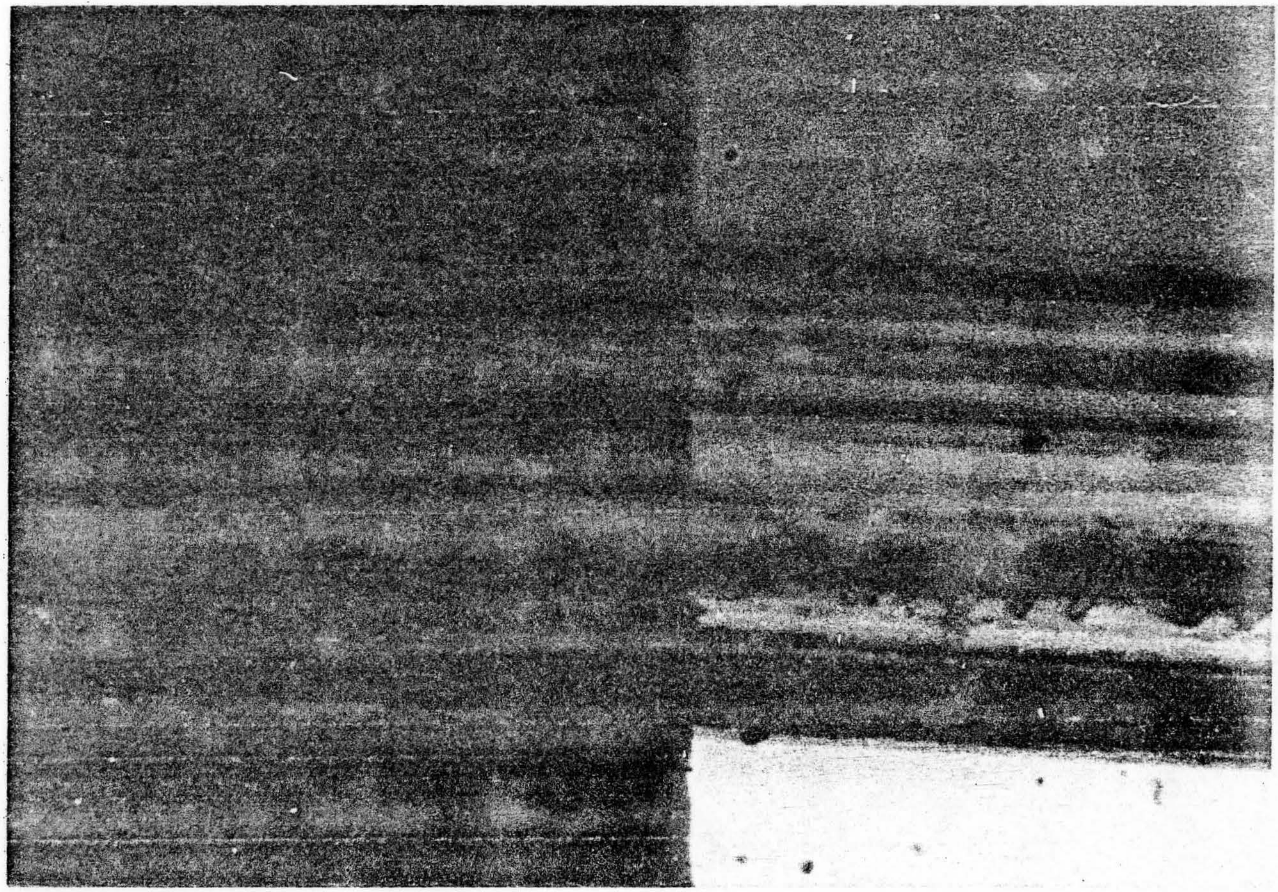

Photograph 10: Photograph of the mechanical diamond stylus cut in photograph 9 magnified 500X.

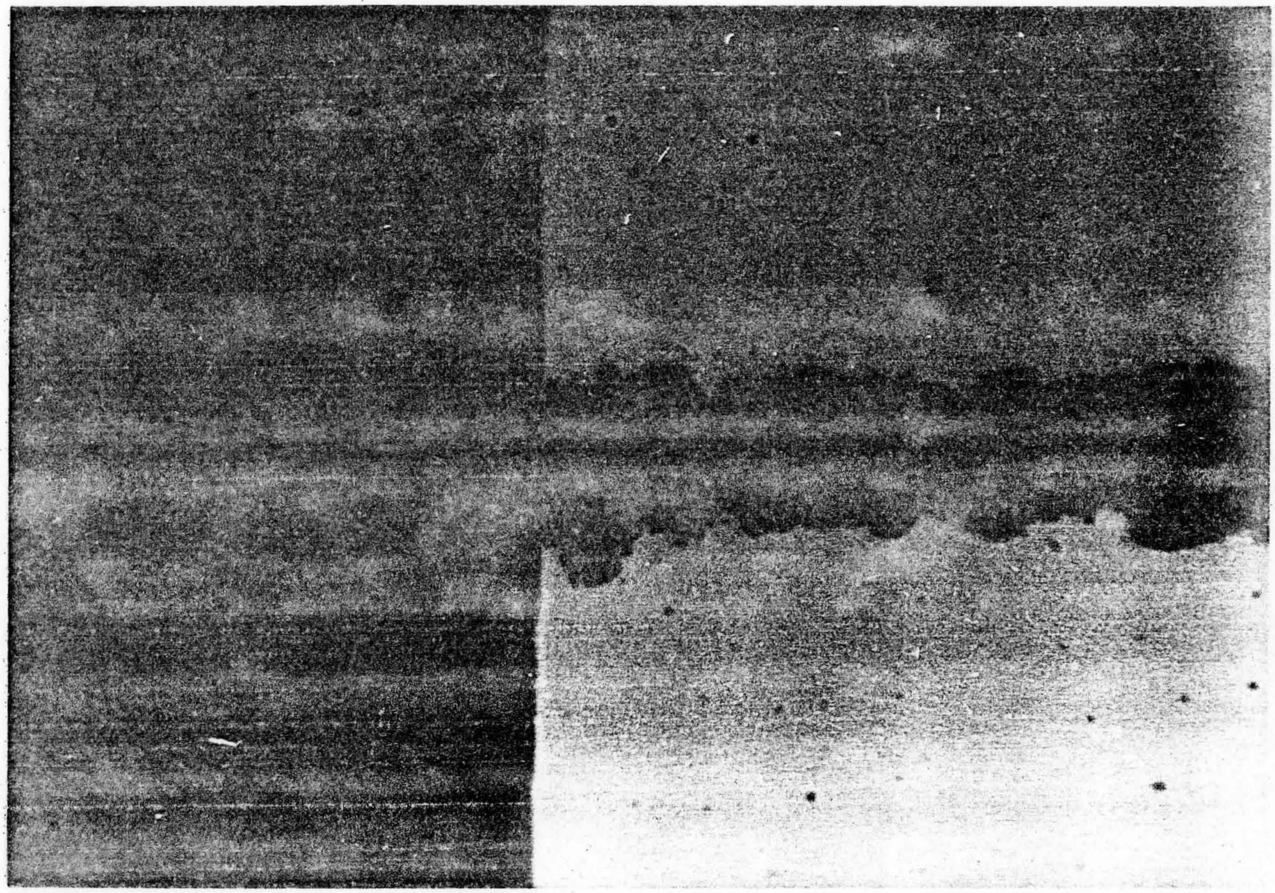

Photograph 11: Photograph of the arc-trim cut in photograph 9 magnified 500X.

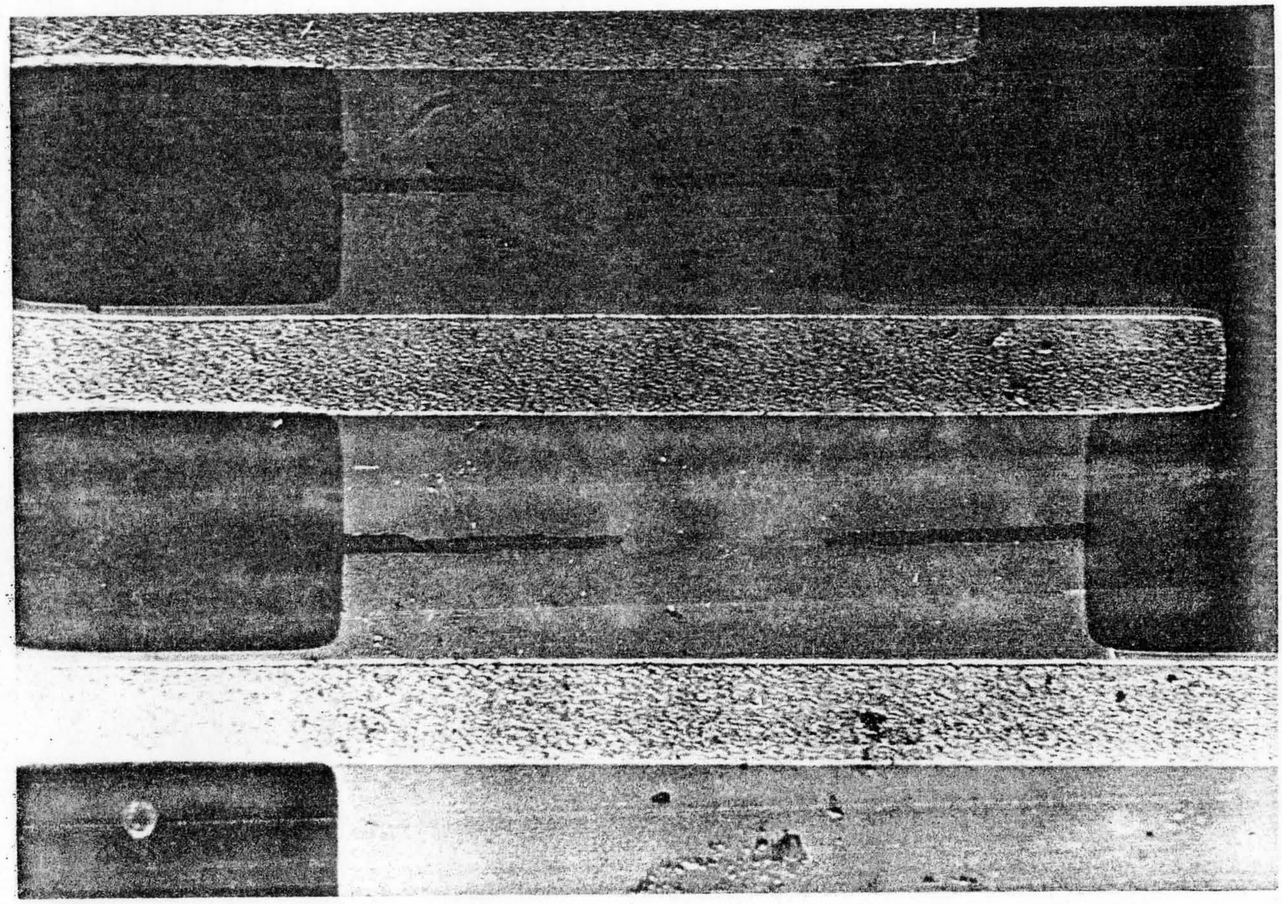

Photograph 12: Tests to determine the effect of tungsten stylus pressure on the nichrome resistor material. The photograph is of the GH1039 spread trim loops at 25X magnification. The stylus is moved left to right and the missing section of the cut in middle is due to the voltage being removed from the stylus. Very little or no stylus disturbance of the nichrome is observed.

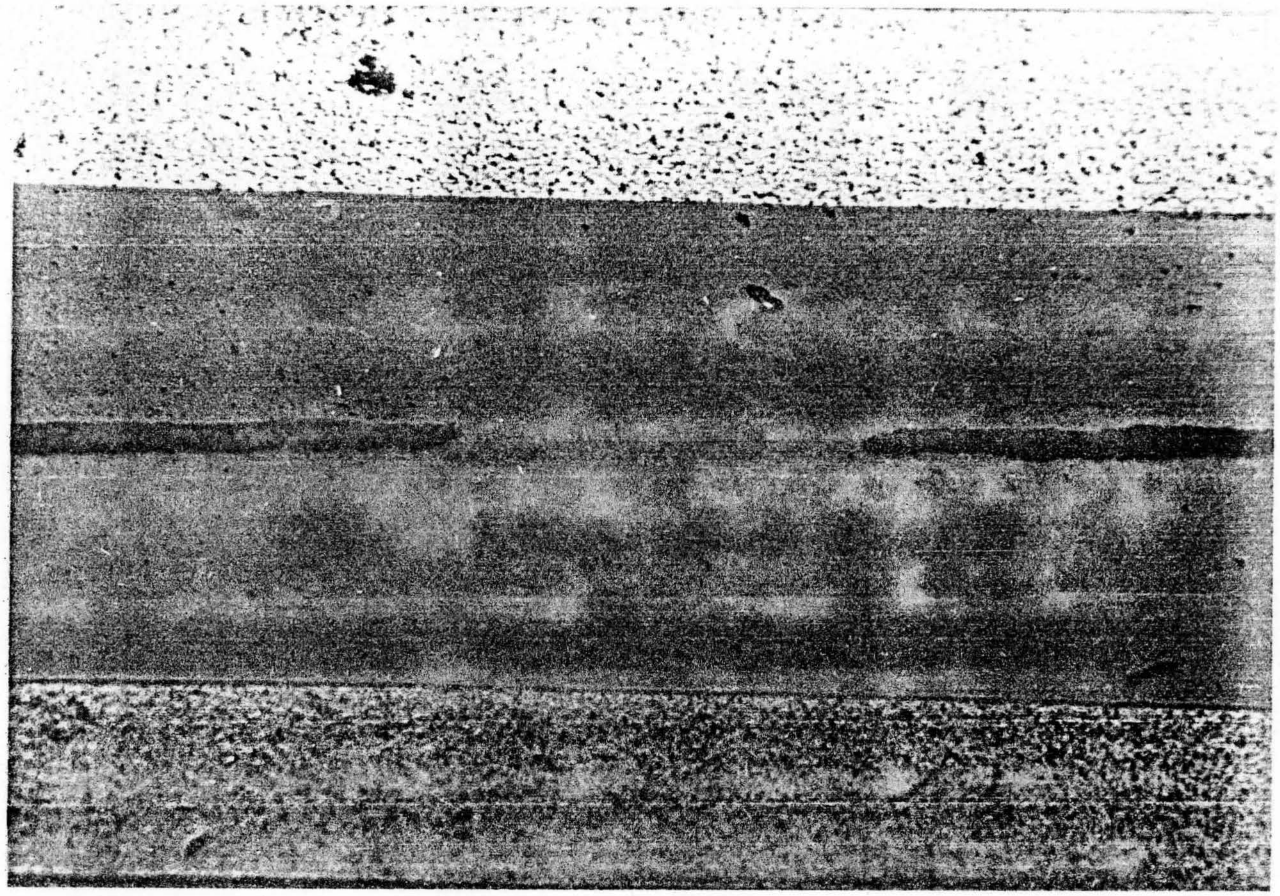

Photograph 13: Lower spread trim loop of photograph 10 magnified 50X. Some light resistor damage is noted.

Photograph 14: Upper spread trim loop of photograph 10 magnified 50X.

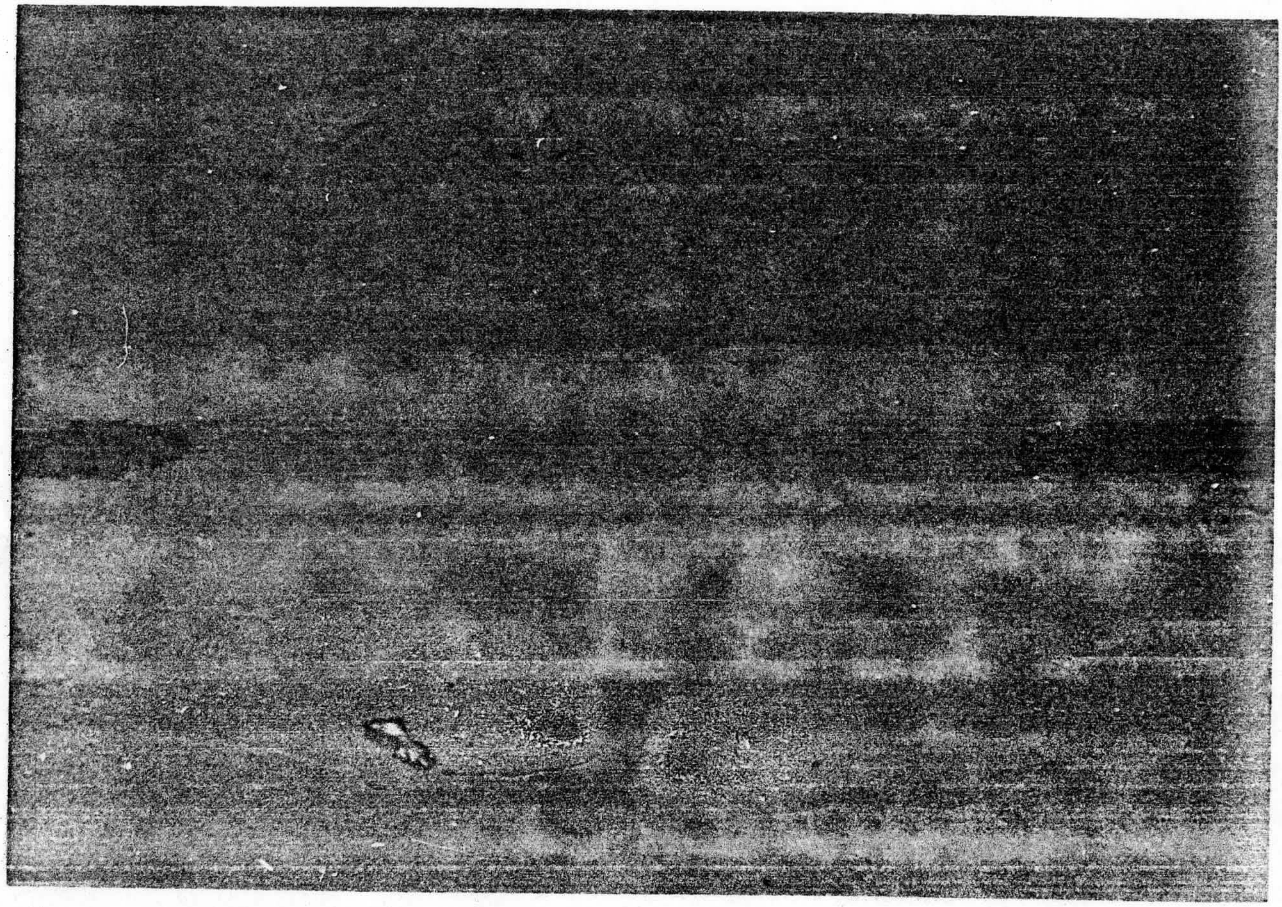

Photograph 15: Lower spread trim loop of photograph 10 magnified 100X.

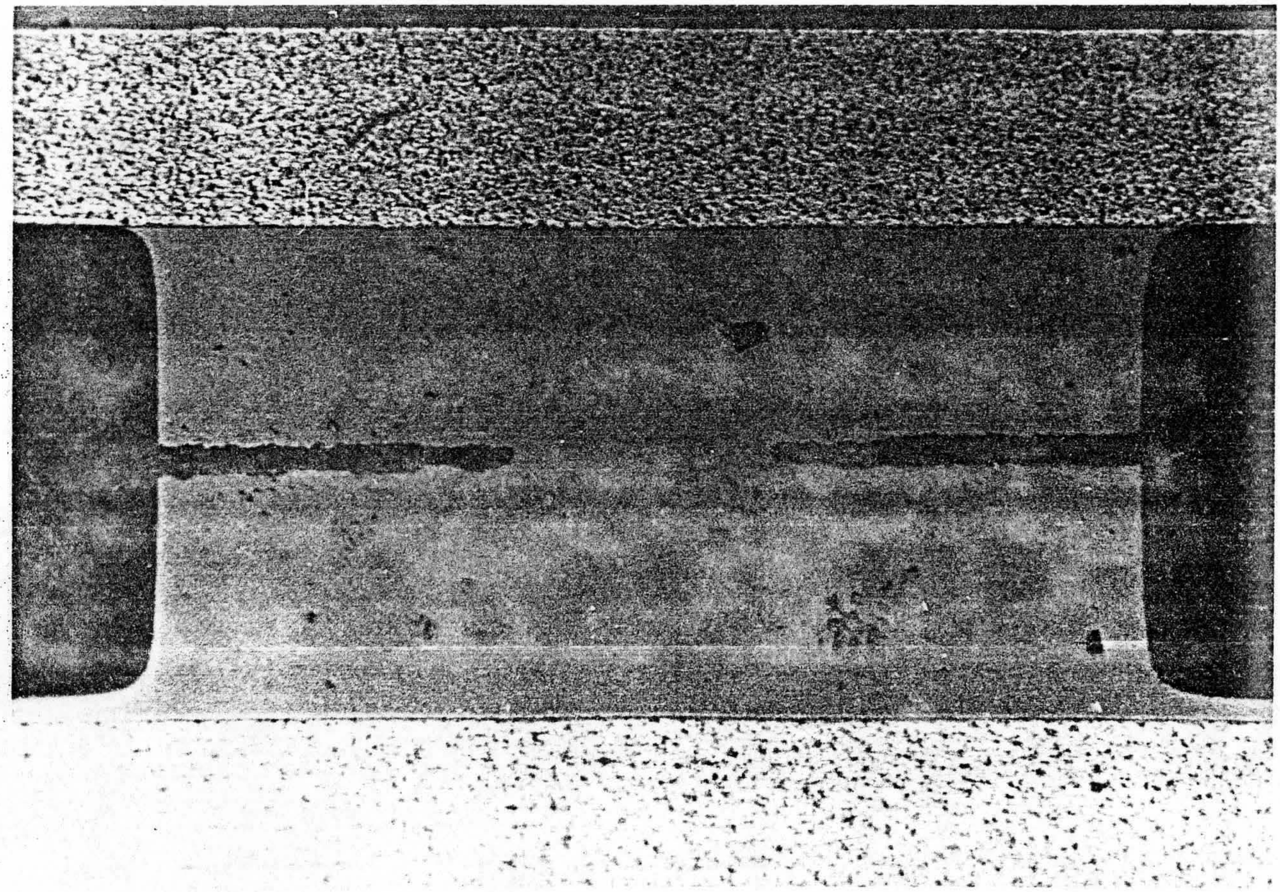

Photograph 16: Upper spread trim loop of photograph 10 magnified 100X.

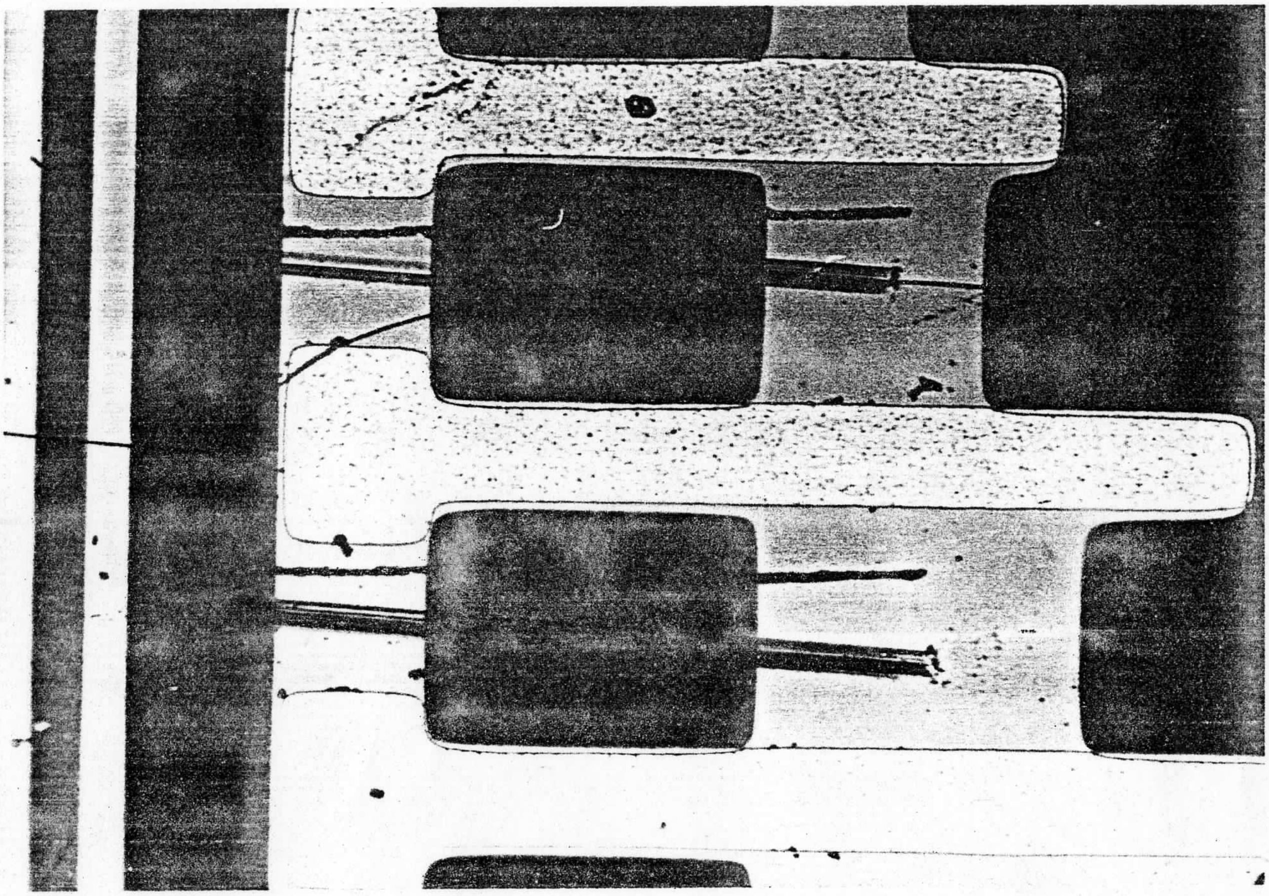

Photograph 17: Photograph of a substrate crack which has propagated through a mechanical cut region scribed with a diamond stylus. This indicates that a mechanical cut causes an undesirable stressing of the substrate.

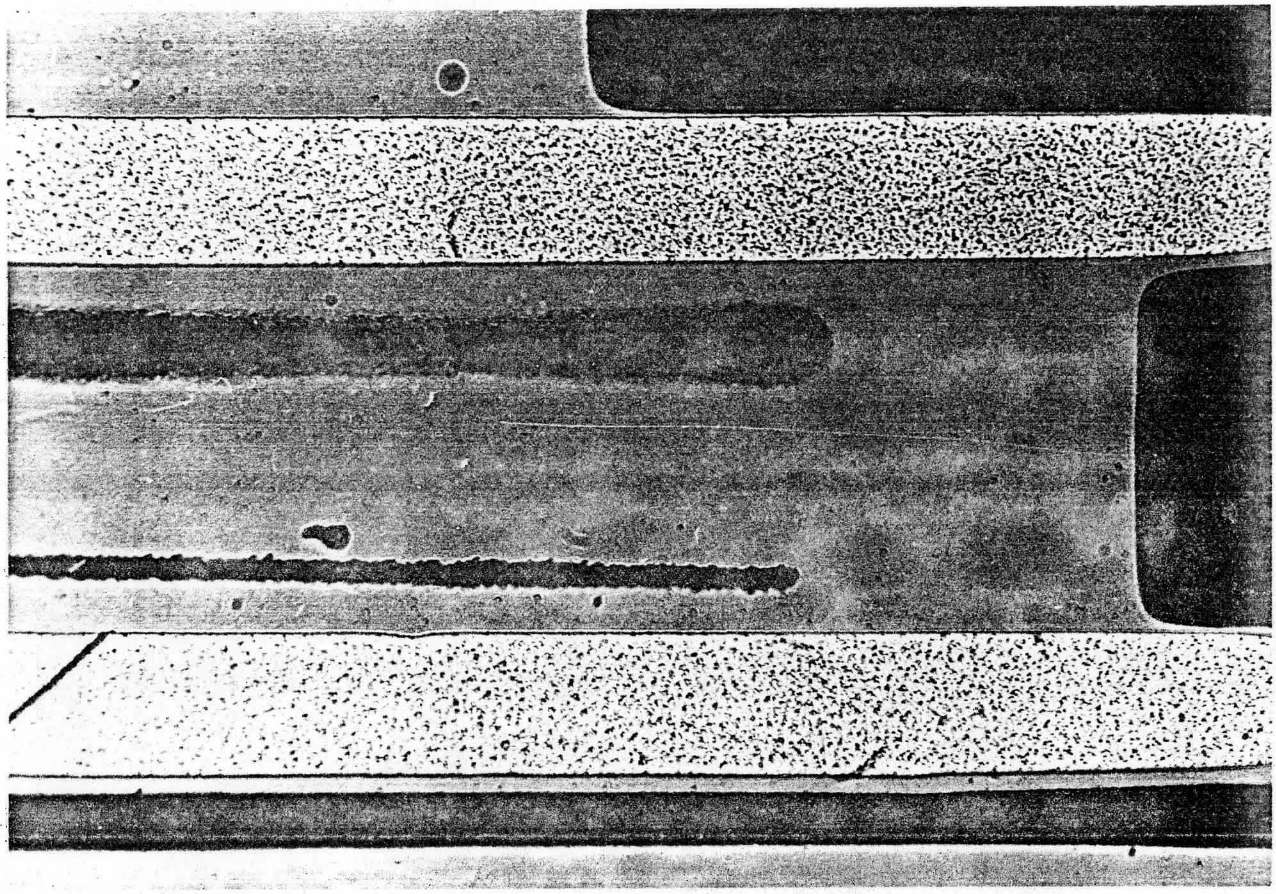

Photograph 18: Comparison of a laser cut and an arc cut made on one of the spread trim loops of the GH1039. Magnification is 50X. The upper trim is the laser cut and the lower, the arc cut. The width of the arc cut is approximately .0002 inches.

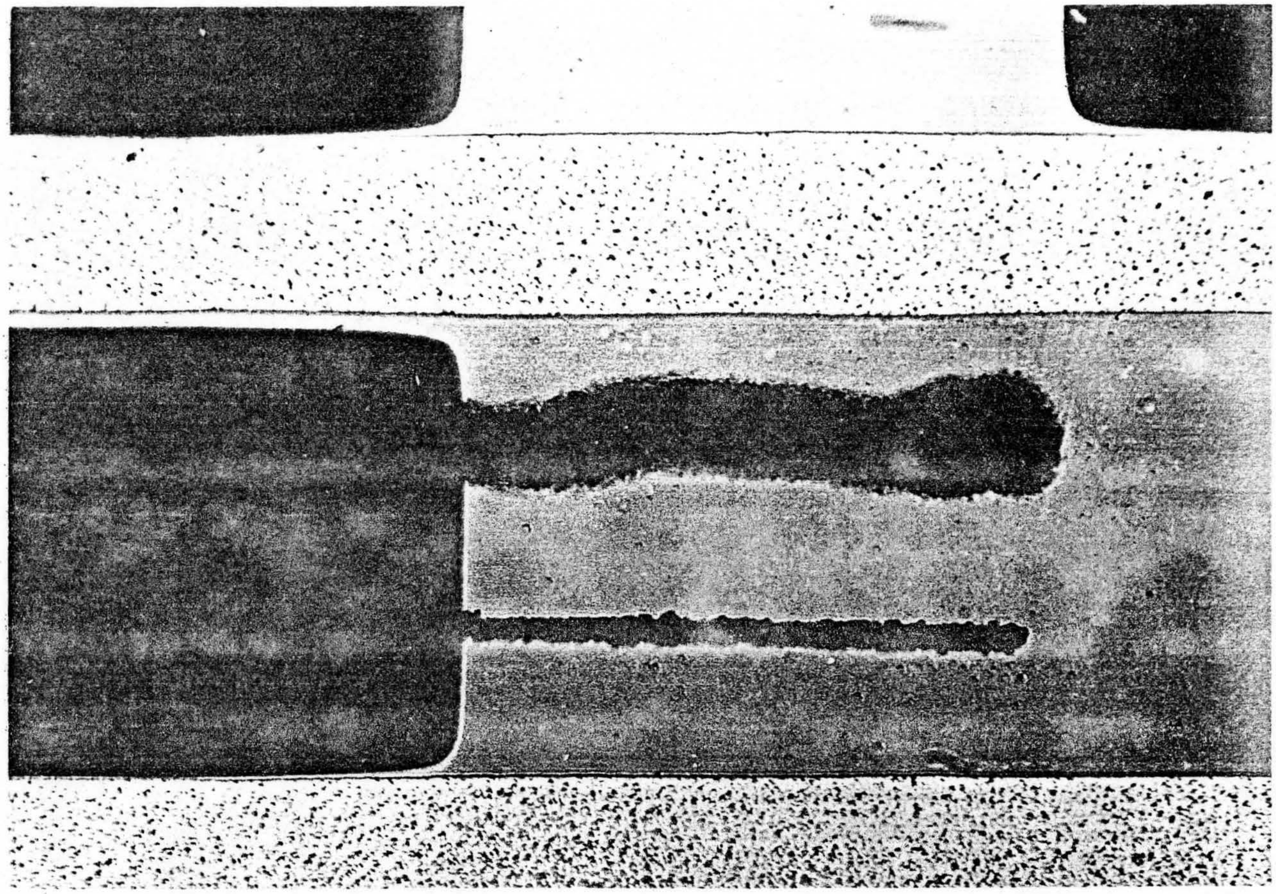

Photograph 19: Comparison of a laser cut and an arc cut made on one of the spread trim loops of the GH1039. Magnification is 50X. The upper trim is the laser cut and the lower, the arc cut. The width of the arc cut is approximately .0002 inches. Note the substrate damage due to the laser cut in the black rectangular substrate region.

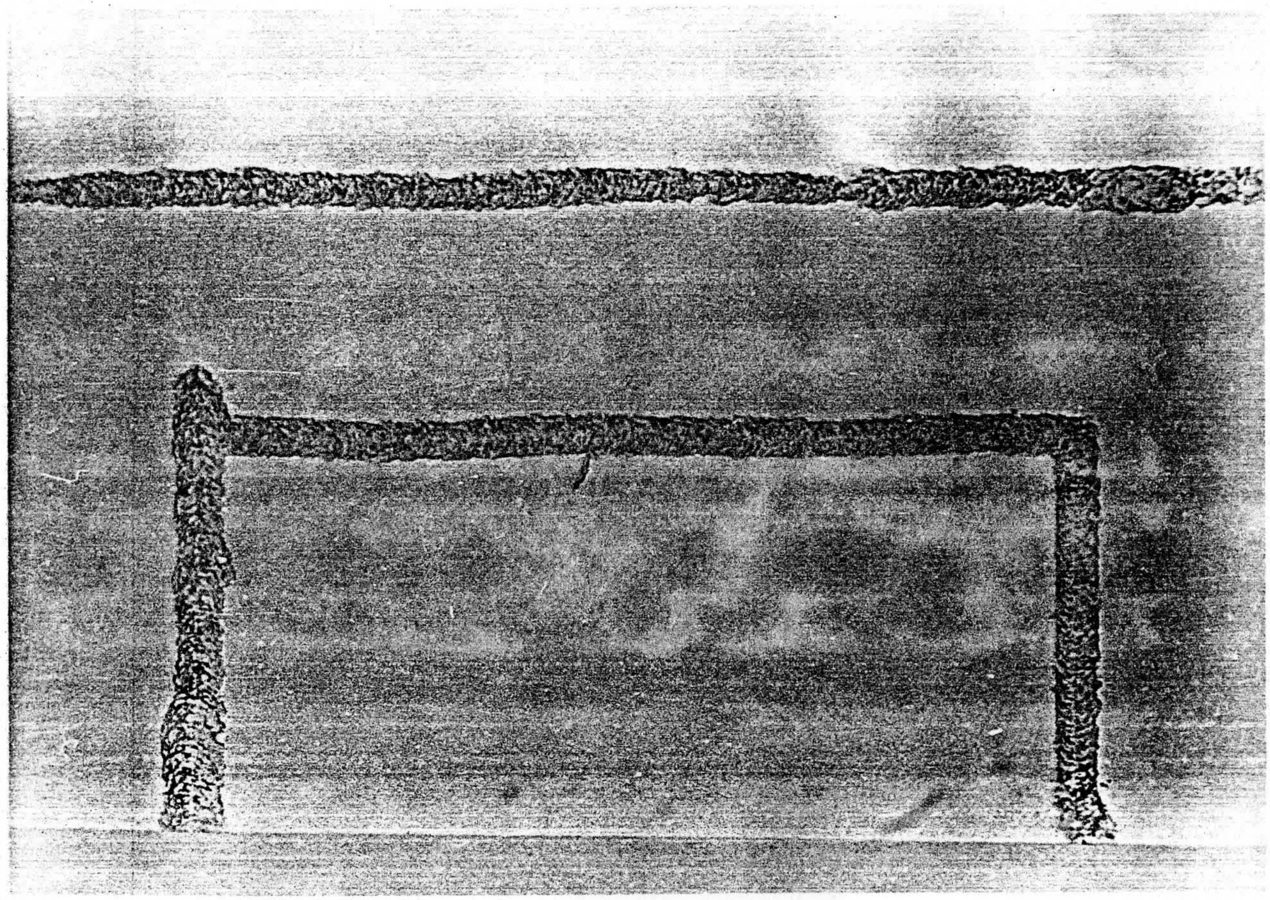

Photograph 20: Typical results of an arc trim on a substrate containing tantalum.